PLANETESIMAL AND PROTOPLANET DYNAMICS IN A TURBULENT PROTOPLANETARY DISK

BY

CHAO-CHIN YANG

DISSERTATION

Submitted in partial fulfillment of the requirements
for the degree of Doctor of Philosophy in Astronomy
in the Graduate College of the
University of Illinois at Urbana-Champaign, 2010

Urbana, Illinois

Doctoral Committee:

Professor Charles F. Gammie, Chair
Professor Mordecai-Mark Mac Low, Director of Research,
American Museum of Natural History
Associate Professor Paul M. Ricker
Associate Professor Leslie W. Looney

Abstract

In a young protoplanetary disk, planetary objects undergo orbital migration due to the gravitational torques exerted by their surrounding gas. It has been an outstanding issue that an earth-sized planet embedded in a gas-rich environment may rapidly migrate into its host star. In this dissertation, I study some of the processes that affect the orbital migration of planetary objects and their roles on planet formation scenarios.

Sharp density features in protoplanetary disks, for instance at the edge of a magnetically dead zone, have recently been proposed as effective barriers to slow down or even stop the problematically fast migration of planetary cores into their central star. Density features on a radial scale approaching the disk vertical scale height might not exist, however, since they could be Rayleigh (or more generally Solberg-Høiland) unstable. Stability must be checked explicitly in one-dimensional viscous accretion disk models because these instabilities are artificially eliminated in the process of reducing the full set of axisymmetric equations. The disk thermodynamics, via the entropy stratification, and its vertical structure also influence stability when sharp density features are present. We propose the concept of Rayleigh adjustment for viscous disk models: any density feature that violates Rayleigh stability (or its generalization) should be diffused radially by hydrodynamical turbulence on a dynamical time-scale, approaching marginal stability in a quasi-continuous manner.

Due to the gravitational influence of density fluctuations in the gas disk subject to magneto-rotational instability, planetesimals and protoplanets undergo diffusive radial migration as well as changes of other orbital properties. The magnitude of the effect on particle orbits has important consequences for planet formation scenarios. To accurately measure the gravitational influence of turbulent density fluctuations on particle orbits, numerical simulations capturing both large-scale and small-scale coherent structures are required. Using local shearing boxes with various resolutions up to 64 points per disk scale height and horizontal sizes up to 16 scale heights, we systematically study the corresponding density structure and particle orbit evolution. We consider ideal magnetized disks with isothermal equation of state, and compare disks with and without vertical stratification. We find that although the results converge with resolution for fixed box dimensions, the response of the particles

to the gravity of the turbulent gas strongly depends on the horizontal box dimension. Our results indicate the dominance of large-scale density structures, which are closely related to recently discussed zonal flow models of protoplanetary disks.

Based on heuristic arguments, some implications may be drawn from the measurements of our local models. The radial diffusive migration of protoplanets induced by magneto-rotational turbulence may be unimportant compared to secular migration. Kilometer-sized planetesimals moving in magneto-rotational turbulence may not suffer from mutual collisional destruction, except for those in the inner region of a young protoplanetary disk. Before these results can be considered valid, though, it will be necessary to elucidate the discrepancies that have appeared between global and local models.

To my parents and my wife

Acknowledgement

This dissertation would not have come to fruition without the assistance of many people. I would like first to thank my advisor, Prof. Mordecai-Mark Mac Low of American Museum of Natural History, who took on such an onerous responsibility and supported my research as well as life in New York. I am very grateful that he allowed me almost complete freedom to explore the world of astrophysics and develop my own thread of research, while offering me help in time whenever I needed it and no matter how urgent it was.

I am indebted to Prof. You-Hua Chu for her enthusiastic support throughout my graduate study. She was always making sure that I was taken good care of, not only in my professional development but also in my daily life. I owe much to Prof. Kristen Menou of Columbia University for he contributed to many of the works reported in this dissertation. I am thankful that Prof. Charles Gammie served willingly as the chair of my dissertation committee and engaged me in many constructive discussions of my research. Many thanks to Prof. Paul Ricker, who also advised my research for more than two years and is very patient working with students. I thank Prof. Leslie Looney and Prof. Ronald Webbink for their service in my committee.

I was fortunate to be working with Dr. Robert Gruendl for one year, from whom I learned many observational techniques. I also benefited from many conversations with Dr. Anders Johansen of Lund University, Sweden.

Studying in a foreign country would have been much more difficult if there had been no encouragement and help from friends and fellows. I am especially appreciative of and enjoyed the good company of many Taiwanese friends and fellow graduate students, who made my life much easier.

I am pleased to express my gratitude to the support staff in the Department, Jeri Cochran, Dr. Bryan Dunne, Mary Margaret O'Connor, Sandra Osterbur, and Kevin Pointer, and Gwendolyn King in the Department of Astrophysics at the American Museum of Natural History for their excellent administrative and support services.

Special thanks are due to my parents and my extended family. They always understand and absolutely support the career path I am pursuing, no matter how difficult it may be.

Finally, this dissertation is dedicated to my lovely wife, Chih-Ting Hsieh. She made uncountable sacrifices and endured many of my tedious and endless working cycles. Without her complete understanding and hearty encouragement, I would not reach this stage in my pursuit of an academic career.

Table of Contents

Chapter 1

Introduction

1.1 Extrasolar Planets

The year 1995 is often marked as the first discovery of a planet around a solar-type star. Reported by Mayor & Queloz (1995) and immediately confirmed by Marcy & Butler (1995), it is a Jupiter-mass object orbiting the star 51 Pegasi with a period of about four days. The same object was in fact detected earlier by Latham et al. (1989), but the data was not definitive enough to rule out the possibility of it as a brown dwarf. Since then, more and more planet-like objects outside our solar system have been discovered. The observations of nearby stars have been improved so significantly that the detection of these extrasolar planets has become routine.

As of this writing, about 463 extrasolar planets in 395 planetary systems are reported. Currently, the lightest object has a mass of $\sim 2 M_{\oplus}$ which is located in the GJ 581 planetary system (Mayor et al., 2009), indicating that the detection of rocky planets like our own begins to become possible. Quite a number of massive planets, so-called "hot Jupiters", orbit their host stars with a very short period, and there exists a pile-up of this kind of objects at a distance of about 0.03 AU.

Interestingly, the range of eccentricity covers from zero to almost up to unity. The highest eccentricity that has been observed is that of the object HD 20782 b, which has an eccentricity of $\sim$0.97 and orbits at a distance of $\sim$1.4 AU (O'Toole et al., 2009). There exists a clear trend of decreasing range of eccentricity with decreasing orbital distance, i.e., the shorter the orbital period, the more circularized the orbit is. This trend can be understood by

tidal circularization, while it is not clear how so many extrasolar planets possess such high eccentricities.

The wealth of data from these observed planetary systems make a statistical study of these objects more and more approachable. The number of systems has reached the point that the distributions of the extrasolar planets against their observed properties become statistically meaningful and can be employed to constrain theoretical models for planetary systems. By computationally simulating the formation and migration of numerous planetary systems and their natal protoplanetary disks, a mock distribution of planets with determined properties can be generated and compared with that of the observed systems. This kind of approach, the population synthesis of extrasolar planets, has been advanced by several authors in recent years (Ida & Lin, 2004a,b, 2005, 2008a,b; Kornet & Wolf, 2006; Robinson et al., 2006; Thommes et al., 2008; Mordasini et al., 2009a,b) and proves to be useful in identifying problematic ingredients in theoretical models.

1.2 Protoplanetary Disks

To understand the formation and evolution of extrasolar planetary systems, the natal protoplanetary disks play a key role. The disk not only serves as a nursery to form new planets, but also interacts with existing planets so that a stable orbital configuration may not achieved. Until the dispersal of the disk, it represents a very dynamical environment, which is actively investigated by many researchers. Here we only consider the early stage of the protoplanetary disk when significant gas is still present.

1.2.1 Physical Properties

The *Hubble Space Telescope* has revealed numerous protoplanetary disks around young stellar objects (e.g., Burrows et al., 1996; McCaughrean & O'dell, 1996; Padgett et al., 1999). These disks can also be directly imaged by ground-based observations like millimeter wave interferometry (e.g., Dutrey et al., 2007; Watson et al., 2007). The advance of high-resolution, multi-band observations has allowed detailed studies of their structures. However, the determination of the physical properties of these disks remains a major challenge.

One of the most important properties that affect the evolution and dynamics of these

disks is their mass. To estimate the mass, two approaches are often used. The first technique is to measure the dust emission and convert it to the gas mass, and the second is to measure the CO emission and convert it to the molecular hydrogen mass. However, major unknowns exist in both methods. The first method involves the dust opacity, which may be considerably different from that in the interstellar medium, and the assumption of the gas-to-dust ratio of about 100. The second method, on the other hand, requires not yet available the understanding of the chemical evolution in such dense environments. In spite of these difficulties, the mass of a typical protoplanetary disk is estimated to be on the order of $\sim 10^{-2}$ $M_{\odot}$ (e.g., Andrews & Williams, 2005). Hartmann (2008) argued, however, that this might be an underestimate.

Another important property is the disk lifetime, which seriously constrains the timescale for planet formation. One technique to estimate this is to observe the dust continuum emission in stellar clusters, and determine the disk frequency of each cluster. By comparing the disk frequency and cluster age, the disk lifetime can be evaluated. Current estimates point to a disk lifetime of $\lesssim$10 Myr (e.g., Hartmann et al., 1998; Haisch et al., 2001; Sicilia-Aguilar et al., 2006; Henning, 2008). Furthermore, this property may also depend on the stellar mass (Carpenter et al., 2006) and the spectral type (Lada et al., 2006).

1.2.2 Turbulent Accretion

Through its own magnetosphere, a young stellar object may still be in the process of accreting materials from the surrounding gas disk (see, e.g., Camenzind, 1990). This mechanism may account for the ultraviolet, optical, and infrared excesses as well as emission lines observed on the photospheres of T Tauri stars, and a mass accretion rate of the order 10^{-9}–10^{-7} $M_{\odot}$ yr^{-1} is often required in this late phase of star formation (e.g., Bertout et al., 1988; Königl, 1991; Valenti et al., 1993; Calvet & Gullbring, 1998).

A young protoplanetary disk is often considered as an accretion disk that is powered by viscous shear stress, with which angular momentum is transported radially outward while materials drift inwards. One important parameter to quantify the kinematic viscosity ν within the gas disk is the α parameter (Shakura & Sunyaev, 1973). It is a dimensionless parameter to normalize ν by the local speed of sound c_s and the vertical disk scale height

H, i.e., $\nu \equiv \alpha c_s H$. By constructing a viscously evolutionary model to match the correlation between stellar age and mass accretion rate from observations, Hartmann et al. (1998) suggested α could be on the order of 10^{-2}, which is often employed as the fiducial value of the parameter in protoplanetary disks.

Despite a lack of direct observational evidence, it is generally believed that turbulence should exist in protoplanetary disks. Turbulent motions in a differentially rotating disk in effect transport angular momentum over various scales, and this process may be modeled as a kind of shear viscosity. This turbulent viscosity has been shown to provide much more shear stress than the molecular viscosity intrinsic to the gas.

One of the most promising mechanisms to drive turbulence is the magneto-rotational instability (MRI; see the review by Balbus & Hawley, 1998, and references therein). This mechanism acts because a weakly magnetized disk is unstable to linear axisymmetric perturbations. The disk quickly saturates into a statistically-steady turbulent state after a few orbital periods (e.g., Brandenburg et al., 1995; Hawley et al., 1995). The magnetic stress in this saturated state provides a significant amount of shear stress.

Although the MRI may be effective in driving turbulence in protoplanetary disks, concern about the convergence of numerical simulations with increasing resolution was raised recently. It was shown that the strength of the saturated magneto-rotational turbulence in ideal, unstratified disks without mean magnetic flux decreases with increasing resolution and might be negligible when resolution is high and numerical dissipation is small (Fromang & Papaloizou, 2007; Pessah et al., 2007). It has been argued, however, that *only* if there is (1) no vertical stratification (Shi et al., 2009; Davis et al., 2010) and (2) no explicit dissipation, or the Prandtl number is small (e.g., Fromang et al., 2007; Lesur & Longaretti, 2007) and (3) exactly zero net magnetic flux (e.g., Guan et al., 2009; Simon et al., 2009) is convergence a problem.

Yet another concern is that the MRI requires sufficient conductivity and thus ionization in the gas to operate, but this requirement may not be fulfilled in some regions of a typical protoplanetary disk. The disk temperature is so low that collisional ionization is not effective. Other sources of ionization may include the cosmic rays and the ultraviolet radiation from the host stars, but the column density in a gas disk may be so high that ionizing radiation from

these sources may not penetrate, leaving the mid-plane poorly ionized. This led Gammie (1996) to suggest that a typical T Tauri disk should be in a state of layered accretion, where the mid-plane is magnetically inactive down to a certain radius and sandwiched by upper and lower active surface layers. This quiescent region is known as the dead zone.

The dynamics of layered accretion continues to be an active research topic. In addition to the cosmic rays and the ultraviolet radiation, the degree of ionization depends on x rays from the star (Glassgold et al., 1997; Igea & Glassgold, 1999), dust grains and chemical network (Sano et al., 2000; Semenov et al., 2004; Ilgner & Nelson, 2006; Bai & Goodman, 2009), metal abundance (Fromang et al., 2002), and mixing (Turner et al., 2007). Interestingly, even though the dead zone is magnetically inactive, significant hydrodynamic motions inside can be generated by turbulent surface layers, and thus provide some source of shear stress (Fleming & Stone, 2003; Oishi & Mac Low, 2009).

1.3 Planet Migration

When the protoplanetary gas disk is present, it interacts gravitationally with embedded planetary objects such that the objects undergo orbital migration throughout the disk lifetime. The direction and the rate of the migration directly depends on the structure of the disk.[1] Orbital migration is an important aspect in the population synthesis of extrasolar planets (Section 1.1), and it inevitably constrains the formation scenarios of the planets.

Several migration mechanisms exist. The first is the so-called type I migration, which operates most efficiently on protoplanets of earth-like mass. In this case, a protoplanet is not massive enough to open a gap in the gas disk and is thus embedded within the gas. It excites density waves through Lindblad resonances and thus exerts torque on the disk. Angular momentum is transferred through the torque and orbital migration of the object occurs. The torque exerted on the protoplanet can be calculated analytically by linear analysis (e.g., Goldreich & Tremaine, 1980; Ward, 1997; Tanaka et al., 2002; Menou & Goodman, 2004). For a laminar, isothermal gas disk with smooth structures, the torque exerted on the protoplanet is in general negative and thus the protoplanet migrates inwards,

[1]The orbital migration of a planetary object may also be affected by surrounding solid objects as well as other planets, which is not considered in this dissertation.

which was confirmed by numerical simulations (e.g., D'Angelo et al., 2003; Bate et al., 2003).

For the simple disk model mentioned above, the timescale for the inward type I migration is short compared to the typical disk lifetime of $\lesssim$10 Myr (Section 1.2.1). For example, for a 5 $M_\oplus$ object embedded in the minimum mass solar nebula (Hayashi, 1981), the infall timescale is only about 2×10^5 yr (e.g., Papaloizou & Larwood, 2000). Furthermore, the timescale is inversely proportional to the mass of the protoplanet; it is even shorter for more massive objects. These considerations pose serious problems on the survivability of protoplanets under type I migration.

Once a protoplanet grows into Jupiter-mass range, it is massive enough to open a gap in its vicinity. In this regime, called type II migration, the protoplanet co-evolves with the protoplanetary disk and migrates inward with the viscous timescale of the disk, as long as the mass of the object is relatively small compared to the disk mass (Lin & Papaloizou, 1986). This timescale is significantly longer than that of type I migration, and thus type II migration does not likewise pose serious threats to Jupiter-like protoplanets.

The problematic rapid inward type I migration has been one of the major issues in the theories of planet formation. Given such a short timescale, no planets should exist, which obviously contradicts with findings of numerous extrasolar planets. To be able to gain some success in comparison with observed planetary systems, most of the population synthesis models mentioned in Section 1.1 need to artificially reduce the type I migration by a significant factor or even completely ignore it. Several mechanisms have been proposed to alleviate this issue, and we discuss some of them in greater detail in Chapter 2.

All of the above discussion considers only a laminar disk. As mentioned in Section 1.2.2, a protoplanetary disk could be viscously evolving due to turbulence, which in turn could be driven by the MRI. The turbulence causes density enhancements significant enough to exert gravitational torques that turn the orbital motion of low-mass objects into a random walk (Laughlin et al. 2004, hereafter LSA04; Nelson & Papaloizou 2004). It has been shown that radial excursions and eccentricities of planetesimals or protoplanets could be excited through such a process (Nelson 2005, hereafter N05; Ogihara et al. 2007, hereafter OIM07). Since some protoplanets could diffuse their way radially outward in the process, type I migration might be effectively delayed and some objects might more easily survive past the

gas disk depletion (Johnson et al. 2006, hereafter JGM06; Adams & Bloch 2009). Even if the disk contains a dead zone, Oishi et al. (2007, hereafter OMM07) have shown that low-mass objects within the dead zone still experience some of the turbulent torques generated by the active layers. Quantifying the gravitational effects of magneto-rotational turbulence on planetesimals and protoplanets is the main focus of Chapters 3 and 4.

Finally, we note a possible generalization to type I migration that has recently become promising to eliminate the rapid inward migration rate. In previous analyses of type I migration, the protoplanetary disk was usually assumed to be isothermal, which may not be applicable in the optically thick region deep inside the disk mid-plane. By relieving this assumption and considering adiabatic or radiative regime, studies find that orbital migration rate in the disk may be reduced or even reversed (Paardekooper & Mellema, 2006; Kley & Crida, 2008; Paardekooper & Papaloizou, 2009; Paardekooper et al., 2010). Further confirmation and development of this new mechanism seems warranted.

1.4 Planet Formation Scenarios

Currently, two opposing scenarios for planet formation are under active research and development. One is the so-called 'core accretion model', and the other is through gravitational instability and fragmentation of the gas disk. We briefly review these two scenarios.

1.4.1 Core Accretion

In the core accretion model, terrestrial planets and planetary cores are built through accretion of solid materials. When a protoplanetary disk first forms out of its natal cloud, it contains μm-sized dust grains coming directly from the interstellar medium. Due to drag force exerted by the gas, these grains settle into the disk mid-plane and co-move with the disk gas. Through mutual collisions, dust grains coagulate and grow in size. The effectiveness of this process depends on the sticking properties of the grains, which can be studied in laboratories (see, e.g., the review by Blum & Wurm, 2008). In less than 10^4 yr, centimeter- to meter-sized particles can be grown through this process.

With the increase in size, however, these particles gradually decouple from the gas while still acted on by the aerodynamic drag. Due to radial pressure support in a protoplanetary

gas disk, the gas rotates somewhat slower than Keplerian frequency, while the solid particles follow Keplerian rotation. This difference in velocity makes the particles experience constant "head wind", lose their angular momentum, and radially drift towards the host star. The timescale of this infall process reaches its minimum at a size of $\sim$1 m, being less than 100 yr at 1 AU (Weidenschilling, 1977). With such a short timescale, no further growth could occur and a protoplanetary disk should clear out meter-sized bodies quickly, posing a serious obstacle in the core accretion scenario.

A fast process for meter-sized bodies to grow into kilometer-sized planetesimals is required to overcome this meter barrier. It has been proposed that this rapid growth could be achieved by the streaming instability (Youdin & Goodman, 2005). This instability works with the back reaction from the solid particles to the gas and exponentially enhances local clumping of the particles. Typically, the growth rate of this instability increases with background solid-to-gas ratio. Since local pressure maxima intermittently occurring in turbulence can serve as a temporary trap of solid particles to increase this ratio, turbulence and streaming instability may cooperate to boost the density of particle clumps to the point that gravitational collapse sets in to form bound objects. This mechanism was demonstrated by numerical simulations, and planetesimals as large as $\sim$1000 km could be formed (Johansen et al., 2007, 2009; Bai & Stone, 2010a,b), which was supported by population synthesis models constrained by the size distribution of the Asteroid belt (Morbidelli et al., 2009).

Once kilometer-sized planetesimals are formed, the growth process continues by mutual collisional accretion. Ida et al. (2008, hereafter IGM08) suggested that the velocity dispersion of planetesimals excited by magneto-rotational turbulence might be so large that kilometer-sized objects suffer from collisional destruction instead of accreting. We also discuss this issue in Chapters 3 and 4.

Later in the process, a population of well separated planetary cores are formed, reaching an oligarchic growth phase. These cores keep accreting small bodies in their immediate vicinities, a process that is also aided by gravitational focusing. This process continues till a core reaches a critical mass of $\sim$5–15 $M_\oplus$ when runaway gas accretion occurs to form a giant planet (e.g. Pollack et al., 1996; Alibert et al., 2005; Rafikov, 2006). As noted in Section 1.3, rapid inward type I migration works against this process and remains to be resolved.

1.4.2 Gravitational Instability

In contrast to the core accretion model, it was suggested that giant planets could be directly formed by gravitational instability and fragmentation of the gas disk (e.g., Kuiper, 1949; Cameron, 1962). The advantage of this scenario is that it operates on a very short timescale, avoiding some long processes involved in the core accretion model.

For young massive protoplanetary disks, the condition for gravitational instability to occur is probably easy to meet. However, sufficient cooling is required for subsequent fragmentation to occur to form bound objects. Using a two-dimensional local shearing sheet, Gammie (2001) showed that the condition $\Omega\tau_c \lesssim 1$ is required for gas fragmentation to occur after gravitational instability sets in, where τ_c is the cooling timescale and Ω is the angular velocity of the disk gas. If the cooling timescale is greater than the orbital timescale, the disk does not fragment and a marginally unstable, turbulent state is sustained. This condition was further confirmed by numerical simulations of global disks (Rice et al., 2003). This restriction inhibits the formation of giant planets via gravitational instability within at least a few tens of AU in a typical protoplanetary disk (Rafikov, 2007, 2009).

1.5 Computations

Given the complexity of many astrophysical systems we are interested in studying, we often seek approximate solutions to these systems via numerical methods. It is no exception that the research reported in this dissertation also heavily relied on successful usage of many computational techniques. In this section, we highlight several aspects of computing implementation relevant to our work.

1.5.1 The Pencil Code

We chose the Pencil Code[2] as our main tool to study particles moving simultaneously within magneto-rotational turbulence.

The principle concept behind this code is to spatially discretize any system of partial differential equations by sixth-order finite differences. All the derivatives are evaluated along

[2]The Pencil Code is publicly available at `http://code.google.com/p/pencil-code/`.

one-dimensional arrays of grid points (called pencils) in one direction at a time, achieving high cache efficiency. Then the system is forwarded in time using third-order Runge-Kutta method.

There exist several advantages with this approach. Calculating finite differences is computationally inexpensive compared with, e.g., spectral methods or Godunov methods. However, it does not sacrifice accuracy. Instead, the higher the order, the better its spectral resolution, approaching that of a spectral method, which has perfect resolving power down to the smallest scale of the grid. Furthermore, the truncation errors of high-order finite differences are also high order, introducing no formal numerical dissipation. Therefore, this code is optimal for simulating weakly compressible turbulent flows, which requires high fidelity at high spectral frequency.

Since this code induces no formal numerical dissipation, an explicit stabilizing scheme is needed. Ideally, this scheme should only dissipate power near the grid scale while preserving the power at any other scale as much as possible. This goal is achieved in the Pencil Code by implementing hyper-dissipation terms. These terms are composed of sixth-order derivatives like $\partial^6/\partial x^6$ explicitly added into each equation of the system. The strength of the dissipation should scale with k^6, where k is the wavenumber of any structure. This high-order dependence makes the dissipation highly nonlinear, being very small for most long-wavelength structures while increasing rapidly at high frequency. By carefully choosing the coefficients of these terms such that the mesh Reynolds number is maintained near unity (see Equation (3.7) of Chapter 3), only power near grid scale is damped while still maintaining the stability of the code.

Inevitably, if the system contains or evolves into shocks or any type of discontinuities, a shock-capturing scheme is still necessary. In the Pencil Code, a von Neumann type of artificial viscosity is implemented. In multi-dimensional case, divergence of the velocity field is used as the kinematic viscosity and therefore converging flows are targeted to be damped (Haugen et al., 2004; Lyra et al., 2008). We further impose a lower cutoff to the magnitude of the divergence such that weakly converging flows are not dissipated in order to preserve most features in the system (see Equation (3.4)).

The code is also capable of simulating particle dynamics, which is solved simultaneously

with the Runge-Kutta steps evolving the fluid. The gravitational potential is calculated with fast Fourier transforms. Particle-gas interactions are computed with the standard particle-mesh method, and momentum conservation for these interactions has been taken into account (Johansen et al., 2007).

A final remark is that the Pencil Code is not formulated to be conservative. Conserved quantities are monitored, instead, to evaluate the quality of the solution. In practice, however, these quantities are well conserved in our simulations.

1.5.2 Local Shearing Box versus Global Disk

In Chapters 3 and 4, we use the local shearing box approximations to simulate a small Cartesian box located near the disk mid-plane and at a large distance from the central star (Goldreich & Lynden-Bell, 1965; Brandenburg et al., 1995; Hawley et al., 1995). The x-axis is always directed radially, the y-axis azimuthal, and the z-axis vertically. The center of the box rotates about the star at local Keplerian angular frequency. Only terms linear in x/R are preserved, and the global differentially-rotating flow becomes local linear shear flow.

One of the advantages of using a local shearing box is its high resolving power. One disk scale height can easily be resolved by one part in 10^2 or higher, and this seems to be enough to capture small-scale coherent structures in magneto-rotational turbulence (Guan et al., 2009). The other advantage of a local shearing box is that the only timescale involved is the local orbital period, so the system can be integrated for long physical time.

In contrast, a global disk model does not have these advantages. Especially, the orbital period often increases outward with radial distance such that physical time is limited by the orbital period at the innermost boundary. To achieve the same resolution and physical time at any regions of interest of a global disk model as a local shearing box, many more grid points and time-steps are inevitably required. Furthermore, calculating gravitational potential in cylindrical or spherical coordinate systems remains computationally expensive, which limits the ability of a global disk to simulate particle-particle or particle-gas interactions in these coordinate systems.

Admittedly, curvature terms are not implemented in a local shearing box, and thus a local box may not correctly describe large-scale structures as a global disk can. This issue

is one of the major topics discussed in Chapter 4.

1.6 Outline

In this dissertation, I focus my attention on some of the processes that affect the migration of planetesimals and protoplanets in a gas-rich environment. In Chapter 2, I investigate the stability of narrow density profiles that have been suggested to be able to withstand rapid inward type I migration, and propose a self-consistent scheme for one-dimensional, viscously evolving disk models that contain such density features. In the following two chapters, I study massless particles moving under the gravitational influence of density fluctuations in magneto-rotational turbulence, and discuss the implications of the results to planet formation scenarios. The distinction between Chapters 3 and 4 is whether or not the vertical component of the gravity of the central star is included in the models. Finally, I make some concluding remarks in Chapter 5.

Chapter 2

Rayleigh Adjustment of Narrow Barriers in Protoplanetary Disks[1]

As mentioned in Sections 1.3 and 1.4.1 of Chapter 1, one of the major difficulties in the core accretion scenario for planet formation is that before a planetary core can grow into a critical mass of $\sim$5–15 $M_\oplus$ for runaway gas accretion to occur, type I migration due to angular momentum exchange with the natal protoplanetary gas disk can drive the core into the host star in a short time-scale compared to a typical disk lifetime of $\lesssim$10 Myr.

A proposed mechanism to withstand rapid inward type I migration is to induce a steep radial density gradient in the gas disk (Matsumura & Pudritz, 2005, 2006; Masset et al., 2006; Matsumura et al., 2007, 2009; Ida & Lin, 2008b). In particular, since the gas inside the orbit of a planetary core exerts a positive torque on the core whereas the gas outside exerts a negative torque, a large negative radial density gradient in the gas can generate a sufficiently positive torque to halt type I migration. Matsumura & Pudritz (2005, 2006) propose that the transition region in a protoplanetary disk between hydromagnetic turbulence and dead zone can locally provide such a density barrier. On the other hand, by including the co-rotation torque exerted by the gas in the vicinity of a protoplanet, Masset et al. (2006) suggest that a positive torque on the protoplanet can be generated by a positive local density gradient. Ida & Lin (2008b) further study the possibility of a local density bump around the ice line to act as a barrier, and Schlaufman et al. (2009) complement this model by generating mock orbital configurations of extrasolar planetary systems.

However, Papaloizou & Lin (1984) have already pointed out that any local variation

[1]The research reported in this chapter was published in Yang & Menou (2010)

occurring on the order of a disk scale height may render the disk Rayleigh unstable. The sharp feature may then be washed out by the resulting hydrodynamical turbulence. Given that a large local density gradient is necessary to impact type I migration, it is thus critical to examine the stability of such a feature.

We examine the Rayleigh stability of local density features in §2.1. In §2.2, we introduce the concept of Rayleigh adjustment as a possible solution to deal with such features in one-dimensional viscous disk models. In §2.3, we discuss the need to generalize these results by accounting for the possibly important role of entropy stratification and the vertical structure. We conclude with some general comments in §2.4.

2.1 Rayleigh Stability

Since magnetically-coupled regions in a protoplanetary disk are unstable to the magneto-rotational instability (Balbus & Hawley, 1998) and unlikely to develop sharp features, our main concern is the hydrodynamical stability of a magnetically dead zone (Gammie, 1996). The Rayleigh stability criterion is a necessary and sufficient condition for the local axisymmetric stability of an inviscid differentially rotating fluid system (Chandrasekhar, 1961). It states that the specific angular momentum must monotonically increase with cylindrical distance R from the central rotation axis in a flow for strict stability:

$$\frac{\partial}{\partial R}(Rv_\phi) > 0, \tag{2.1}$$

where v_ϕ is the azimuthal velocity of the flow. Near the mid-plane of a protoplanetary gas disk, which is supported by the central stellar gravity and the local pressure gradient, force balance in the radial direction requires that

$$v_\phi^2 = v_K^2 + \frac{R}{\rho}\frac{\partial P}{\partial R}, \tag{2.2}$$

where v_K is the Keplerian velocity at R, ρ is the gas density, P is the gas pressure, and any radial infall has been neglected. Substituting equation (2.2) into equation (2.1) gives the stability criterion

$$v_K^2 + \frac{1}{R}\frac{\partial}{\partial R}\left(\frac{R^3}{\rho}\frac{\partial P}{\partial R}\right) > 0, \tag{2.3}$$

where we have used $v_K \propto R^{-1/2}$.

If variations in pressure, i.e. density or temperature for an ideal gas law, occur on a length scale of order R in a disk, the second term in equation (2.3) is of the order c_s^2, where $c_s = \sqrt{\gamma P/\rho}$ is the sound speed and γ is the adiabatic index (typically 7/5 for diatomic H_2 in the protoplanetary context). In a protoplanetary disk, it is usually the case that $v_K \gg c_s$ and thus the disk is Rayleigh stable irrespective of the sign of the variation. However, if any variation occurs on a length scale of order the disk scale height, $H = R(c_s/v_K)$, the same term becomes of the order $(c_s R/H)^2 \sim v_K^2$, assuming vertical hydrostatic balance holds as usual (e.g. Frank et al., 2002). In other words, the second term in equation (2.3) is of the same order as the first term. Therefore, the disk is prone to Rayleigh instability and sensitive to the exact profile of pressure variations.

Without loss of generality (but see §2.3), we adopt an ideal gas law for the equation of state and focus our stability analysis on the disk mid-plane. We also assume for simplicity that the sound speed c_s is slowly-varying with cylindrical distance R, as compared to the density ρ: $|(\partial c_s/\partial R)/(\partial\rho/\partial R)| \ll c_s/\rho$.[2] Then, to leading order, the stability condition (eq. [2.3]) approximately becomes

$$\left(\frac{v_K}{c_s}\right)^2 + \frac{R^2}{\rho}\frac{\partial^2\rho}{\partial R^2} - \frac{R^2}{\rho^2}\left(\frac{\partial\rho}{\partial R}\right)^2 + \frac{3R}{\rho}\frac{\partial\rho}{\partial R} \gtrsim 0. \tag{2.4}$$

For density variations on a length scale $\sim H$, the fourth term in equation (2.4) is of the order $R/H \sim v_K/c_s$ and thus may be neglected. On the other hand, both the second and the third terms are of the order $(R/H)^2 \sim (v_K/c_s)^2$. Therefore, both the steepness and the curvature of the density profile are important to determine the stability of the disk.

Since the third term in equation (2.4) is always negative, both steeply ascending and descending density profiles may make the disk Rayleigh unstable. For example, we consider a two-fold density drop near $R = R_0$ of the form

$$\rho(R) = \rho_0\left[\frac{3}{2} - \frac{1}{2}\tanh\left(\frac{R - R_0}{\epsilon}\right)\right], \tag{2.5}$$

where ρ_0 is the density after the drop while ϵ controls the width of the drop. At $R = R_0$, the first derivative of the density profile reaches maximum while the second derivative vanishes.

[2]Our analysis could be generalized to address a steep radial temperature profile but we note that one would expect such a feature to be reduced by horizontal radiative transport (see also §2.3 for the role of entropy stratification).

Substituting equation (2.5) in the stability condition (2.4) and evaluating it at $R = R_0$ gives $(v_K/c_s)^2 - (R_0/\epsilon)^2/9 \gtrsim 0$, where we have ignored the fourth term in equation (2.4). Since $H/R = c_s/v_K$, it requires that $\epsilon \gtrsim H/3$ and the maximum slope allowed in this case is $|\partial\rho/\partial R| \sim 3\rho_0/2H$. This illustrates how Rayleigh stability sets an upper limit on the steepness of a density profile.

Furthermore, the second term in equation (2.4) indicates that a disk may be Rayleigh unstable where the second derivative of the density profile is negative. In regions where the profile is concave down, the term sets a lower limit to the radius of curvature. In particular, a cusp pointing upward cannot be stable due to an infinite negative second derivative. Smoothness is a necessary condition in these regions. Locations where pressure or density maxima occur in a protoplanetary disk are of particular interest in that solid grains are captured, but Rayleigh instability may also come into question at these locations in a nontrivial manner. To illustrate this point, we consider a density bump with a Gaussian form,

$$\rho(R) = \rho_0 \left\{ 1 + \frac{H}{\epsilon} \exp\left[-\frac{(R - R_0)^2}{\epsilon^2} \right] \right\}. \tag{2.6}$$

Superposed on a disk of uniform mid-plane density ρ_0, the bump encloses a constant mass (on the order of the mass in an annulus of mid-plane density ρ_0 and width H at $R = R_0$) and has a width proportional to ϵ, provided that $\epsilon \ll R_0$. The most negative second derivative occurs at the peak, where the first derivative vanishes. Evaluating the stability condition (2.4) at $R = R_0$ results in $(v_K/c_s)^2 - 2H(R_0/\epsilon)^2/(H + \epsilon) \gtrsim 0$. Since $H/R = c_s/v_K$, the minimum width allowed for stability is $\epsilon \sim H$. Therefore, a local density maximum cannot be Rayleigh stable if the width of the bump is less than about a disk scale height.

2.2 Rayleigh Adjustment

Once a certain region in a protoplanetary disk reaches a state of Rayleigh instability, we conjecture that the ensuing hydrodynamical turbulence will redistribute material in the disk in such a way that any narrow feature will be smoothed and broadened till the disk recovers a state that is (marginally) Rayleigh stable. The time-scale t_R for a disk to recover a Rayleigh-stable state might be close to the dynamical time-scale of the disk, i.e. $t_R \gtrsim \Omega_{\rm K}^{-1}$, where $\Omega_{\rm K}$

is the Keplerian angular velocity, although a slower growth rate may be expected as one approaches marginal stability. By contrast, standard α-model of thin accretion disks has a viscous time-scale $t_\nu \sim R^2/\alpha H c_s$ (e.g. Frank et al., 2002). Given that $\alpha < 1$ and $H \ll R$, $t_\nu > (R/H)^2 t_R \gg t_R$. In other words, any model of viscously-evolving protoplanetary disks should maintain Rayleigh stability quasi-steadily.

If the condition $t_\nu \gg t_R$ holds, it is useful to implement an adjustment scheme to guarantee that a disk model remains Rayleigh quasi-stable at all time. In evolutionary models like those of Matsumura et al. (2007, 2009) or Ida & Lin (2008b), for instance, this kind of adjustment could be applied at any time-step whenever Rayleigh instability is detected, before one proceeds with the migration torque calculation. The purpose of the adjustment is to capture the final state of the adjustment process when the disk just restores its Rayleigh stability and rotational equilibrium (implied by eq. [2.2]), without any detailed knowledge of the Rayleigh hydrodynamical turbulence occurring on small temporal or spatial scales.

In the hydrodynamical context of interest here, Rayleigh adjustment must involve some level of mass and angular momentum redistribution in the disk. To the extent that the disk reaches a new state of rotational equilibrium (described by eq. [2.2]) after Rayleigh adjustment, however, the adjustment itself can be described as a transition from one state of rotational equilibrium to another such state, under the action of mass redistribution. Therefore, this process may be phenomenologically described by the radial mass diffusion equation

$$\frac{\partial \Sigma}{\partial t} = \frac{1}{R}\frac{\partial}{\partial R}\left(RD\frac{\partial \Sigma}{\partial R} \right), \tag{2.7}$$

where Σ is the vertically-integrated column density and D is the mass diffusion coefficient. We use Σ instead of ρ under the hypothesis that the transport is vertically global. Whether or not the disk evolution due to Rayleigh turbulence can be described by fast radial mass diffusion remains to be demonstrated by full hydrodynamical simulations. In this regard, equation (2.7) can only be deemed to be an approximation to the actual adjustment process.

We hereby describe a simple algorithm to implement Rayleigh adjustment, using the diffusion equation (2.7). As a first step, we ignore any spatial variations and assume that D is a constant to focus our discussion on how to include Rayleigh adjustment into viscously-

evolving disk models. The equation can be discretized as

$$\Sigma_j^{n+1} = \Sigma_j^n + \frac{D\Delta t}{\Delta R^2}\left[\left(\Sigma_{j+1}^n - 2\Sigma_j^n + \Sigma_{j-1}^n\right) + \frac{\Delta R}{2R_j}\left(\Sigma_{j+1}^n - \Sigma_{j-1}^n\right)\right], \tag{2.8}$$

where Σ_j^n is the density at $R = R_j$ and step n, Δt is the time increment of the adjustment scheme, and $\Delta R = R_{j+1} - R_j$ is the grid spacing. We have adopted a regular mesh in equation (8) for simplicity. From von Neumann stability analysis, $\Delta t \leq \Delta R^2/2D$. Substituting $\Delta t = \Delta R^2/2D$ in equation (2.8) gives

$$\Sigma_j^{n+1} = \frac{1}{2}\left(\Sigma_{j+1}^n + \Sigma_{j-1}^n\right) + \frac{\Delta R}{4R_j}\left(\Sigma_{j+1}^n - \Sigma_{j-1}^n\right). \tag{2.9}$$

A Rayleigh unstable density profile can then be treated as an initial guess and equation (2.9) can be iterated to the point when the density first becomes everywhere Rayleigh stable, under the constraint that rotational equilibrium is satisfied throughout (eq. [2.2]). This corresponds to the completion of the turbulent redistribution process induced by Rayleigh instability. Note that the magnitude of the diffusion coefficient D plays no role in determining the final state of the Rayleigh adjustment, which can be seen in equation (2.9), since we have chosen the maximum time-step possible to minimize the number of iterations needed to find the adjusted state. We have verified that the final profile does not depend on the time-step, as long as the von Neumann stability condition is satisfied, and that the total mass of the disk is conserved.

We emphasize that since the diffusion time-scale of this process is about L^2/D, where L is the characteristic length scale of the density profile, sharp Rayleigh-unstable density features (with $L \ll R$) will diffuse much more rapidly than any density structure on large scales. Therefore, in first approximation, the global disk structure will remain largely unaffected by this Rayleigh adjustment even for a globally constant D. Note that such a quasi-instantaneous adjustment scheme can only be justified if the process leading to Rayleigh instability (e.g. viscous mass pile-up) operates much more slowly than the adjustment itself.

As a demonstration, we have implemented this adjustment scheme on the two model density profiles, equations (2.5) and (2.6), previously discussed in §2.1. For concreteness, we adopt $R_0 = 1$ and $H = 0.1$. The parameter ϵ is chosen such that the density profile is Rayleigh unstable. The profile is discretized with 1000 grid points in the range $0.5 \leq R \leq 2$

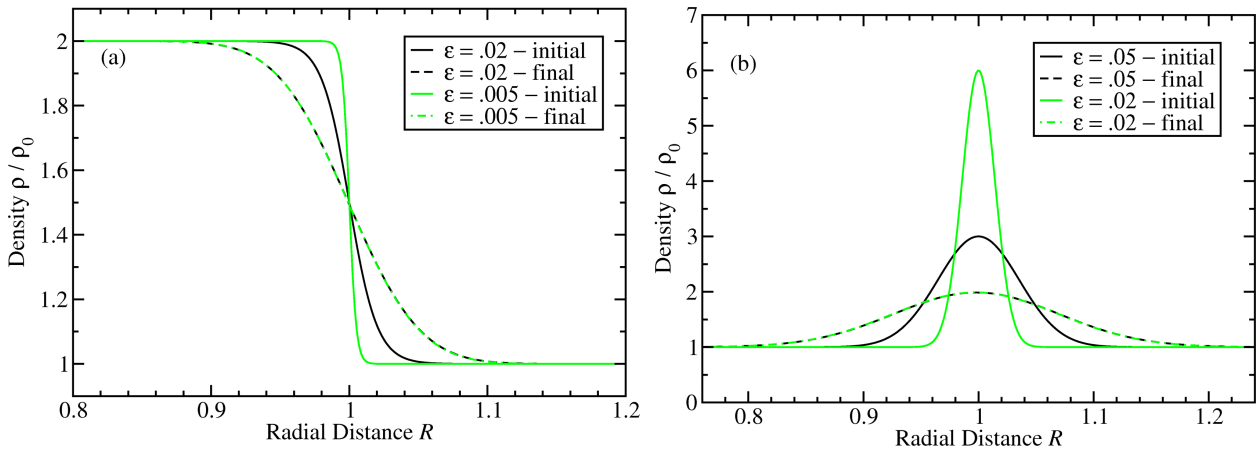

Figure 2.1 Initially Rayleigh unstable (*solid* lines) and final Rayleigh-stable (*dashed* and *dot-dashed* lines) profiles for (a) a density drop (eq. [2.5]) and (b) a density bump (eq. [2.6]) processed through the Rayleigh adjustment scheme discussed in §2.2. With the constant diffusion coefficient adopted in this algorithm, the final relaxed density profiles do not depend on the width of the initially unstable profiles.

and diffused via equation (2.9). As shown in Fig. 2.1, profiles of different initial widths relax to the same enlarged width at marginal Rayleigh stability, which is roughly one disk scale height, H. Even though these results are based on a constant mass diffusion coefficient, they are consistent with the expectation that the width of any density profile is intrinsically limited to $\sim H$ by Rayleigh stability. One expects any variation narrower than $\sim H$ to be smoothed and broadened, although details of this process may depend on the specific Rayleigh adjustment prescription adopted. We note that, in addition to redistributing mass and angular momentum, localized hydrodynamical turbulence in the disk could also directly influence the migration process (e.g. Laughlin et al., 2004; Nelson, 2005; Johnson et al., 2006; Oishi et al., 2007), an effect which is not captured by our adjustment scheme. Potential consequences for the disk thermodynamics have also been ignored.

We note that the mass diffusion equation (2.7) employed here conserves mass in the disk but it does not conserve angular momentum during the adjustment process, under the assumption that rotational equilibrium holds before and after Rayleigh adjustment, as specified by equation (2.2). At first, this would seem to be a serious limitation of the simple mass redistribution scheme proposed here. One may be tempted to improve such a scheme by using instead a more standard viscous equation for mass and angular momentum transport

in a thin disk, of the form

$$\frac{\partial \Sigma}{\partial t} = \frac{3}{R}\frac{\partial}{\partial R}\left[R^{1/2}\frac{\partial}{\partial R}(\nu \Sigma R^{1/2})\right], \tag{2.10}$$

where ν is the effective disk viscosity (e.g. Frank et al., 2002). However, even though this equation does conserve mass and angular momentum in a Keplerian disk, it would be as inadequate as equation (2.7) if used in a Rayleigh adjustment scheme. Indeed, equation (2.10), or its generalizations for non-Keplerian rotation laws, assumes that the disk angular velocity profile is fixed in time. It is precisely the breakdown of this assumption during Rayleigh adjustment, $\partial v_\phi / \partial t \neq 0$, going from one state of rotational equilibrium to another such equilibrium, which prevents this entire class of equations from accurately tracking angular momentum conservation during a Rayleigh adjustment episode. To the extent that one is interested in describing the global evolution of disks in rotational equilibrium with approximate equations such as equation (2.10), one may then choose to consider the small violations in angular momentum conservation occurring during Rayleigh adjustments as an acceptable source of errors, given that it is an unspecified detail at the level of approximation of the viscous theory. This, in our view, motivates the use of the simplest possible mass diffusion scheme, under the constraint of rotational equilibrium, as we have proposed here with equation (2.7).

To summarize, the general outline of a Rayleigh adjustment procedure would be as follows. At each time-step of a one-dimensional evolutionary disk model, evaluate the stability of the disk profile using equation (2.3) or a generalization (see §2.3 below). If the profile is stable, move on to the next time-step of the evolution. Otherwise, use the unstable profile as the initial condition and iterate equation (2.9), or a more sophisticated form of equation (2.7), till the profile has relaxed to marginal stability. Then use the relaxed profile to resume the evolutionary model. Two important assumptions underlying this scheme are (i) that the agent driving the disk viscous evolution acts on a time-scale much longer than the disk dynamical time, (ii) that the relaxed density profile is independent of the pre-adjusted profile, as illustrated in Fig. 2.1 for the simple scheme proposed here.

2.3 Role of Entropy Stratification and Vertical Structure

So far, our discussion has focused exclusively on the Rayleigh stability of a purely radial stratification of angular momentum in the disk mid-plane. More generally, entropy stratification will also be present in the protoplanetary disk and contribute to its axisymmetric stability if sharp density features exist. The full generalization of Rayleigh's stability analysis in the presence of entropy stratification leads to the two necessary and sufficient Solberg–Høiland criteria for axisymmetric stability (e.g. Tassoul, 1978):

$$N_R^2 + N_Z^2 + \frac{1}{R^3}\frac{\partial R^4\Omega^2}{\partial R} > 0, \tag{2.11}$$

$$\left(-\frac{\partial P}{\partial Z}\right)\left(\frac{1}{R^3}\frac{\partial R^4\Omega^2}{\partial R}\frac{\partial \ln P\rho^{-\gamma}}{\partial Z} - \frac{1}{R^3}\frac{\partial R^4\Omega^2}{\partial Z}\frac{\partial \ln P\rho^{-\gamma}}{\partial R}\right) > 0, \tag{2.12}$$

where

$$N_R^2 = -\frac{1}{\gamma\rho}\frac{\partial P}{\partial R}\frac{\partial \ln P\rho^{-\gamma}}{\partial R}, \qquad N_Z^2 = -\frac{1}{\gamma\rho}\frac{\partial P}{\partial Z}\frac{\partial \ln P\rho^{-\gamma}}{\partial Z}, \tag{2.13}$$

$\Omega = v_\phi/R$ is the angular velocity, and Z is the vertical coordinate along the rotation axis. The term $N_R^2 + N_Z^2$ is the sum of the cylindrical radial and vertical components of the squared Brunt–Väisälä frequency.

Equations (2.11)–(2.12) make it clear that the stratifications of entropy and angular momentum both contribute to axisymmetric stability. Since these criteria were derived with respect to any linear axisymmetric perturbation in the (R, Z) plane, they address the cylindrical radial and the vertical components of both stratifications. In the presence of a sharp radial density feature, the radial component of the entropy stratification, which is normally negligible in a disk, can make a significant contribution to local stability. To illustrate this possibility, let us consider a case again where the sound speed c_s is slowly-varying with cylindrical distance R as compared to the density, and let us restrict perturbations to be purely cylindrical radial so that vertical stratification plays no role ($\partial/\partial Z \to 0$ in eqs. [2.11]–[2.13]). In this limit, axisymmetric stability reduces to the much simpler criterion

$$N_R^2 + \frac{1}{R^3}\frac{\partial R^4\Omega^2}{\partial R} > 0, \tag{2.14}$$

which is the equivalent of equation (2.1) with an additional contribution from radial entropy stratification. According to the same scaling analysis as used in §2.1 for equation (2.4), in the

presence of a radial density gradient with length scale H, neglecting any radial temperature gradient on such scales,

$$N_R^2 \simeq \frac{c_s^2}{H^2}\left(1-\frac{1}{\gamma}\right) \simeq \frac{v_K^2}{R^2}\left(1-\frac{1}{\gamma}\right). \tag{2.15}$$

The magnitude of the radial entropy stratification, as measured by N_R^2, could thus be comparable to that of the angular momentum stratification and contribute to the radial stability of the disk configuration.

This suggests that, in the presence of sharp density gradients, it may no longer be possible to ignore the disk thermodynamics for stability considerations. Perhaps even more importantly, equations (2.11)–(2.12) show that the disk radial stability can no longer be studied independently of its vertical structure. In the presence of radial density features with length scale $\sim H$, radial and vertical gradients become comparable in magnitude. The disk stability is then determined by a detailed balance between the radial and vertical stratifications of angular momentum and entropy (eqs. [2.11]–[2.12]). This makes the stability analysis significantly more complicated than considered so far, especially in the case of dead zones with a poorly known vertical structure. It may also imply that a more elaborate treatment than the simple Rayleigh adjustment scheme proposed in §2.2 is required for unstable disks.

2.4 Discussion and Conclusion

The possibility that disks with sharp radial density features may be subject to Rayleigh instability has already been noted by various authors (e.g. Papaloizou & Lin, 1984; Matsumura et al., 2007, 2009). We have reconsidered this issue here and have suggested that stability be checked explicitly in viscous evolutionary disk models which develop such features. In viscous disk models, the full set of axisymmetric equations is reduced to a single radial diffusion equation of the type shown in equation (2.10). Typically, the equation reduction is achieved by imposing a steady angular velocity profile in the disk, $\Omega(R,t) = \Omega(R)$ (often chosen to be Keplerian, like in eq. [2.10]), and by neglecting the radial acceleration term in the radial momentum equation. These are simplifications which contribute to eliminating the class of axisymmetric instabilities discussed here. If sharp density features are to be considered as viable solutions to slow down or even stop protoplanetary migration, with many

important consequences for planet formation scenarios (e.g. Matsumura et al., 2007, 2009; Ida & Lin, 2008b; Schlaufman et al., 2009), a careful examination of stability in viscously evolved models seems warranted.

The various arguments we have put forward are not meant to imply that the sharp density features considered in various works (e.g. Matsumura et al., 2007, 2009; Ida & Lin, 2008b; Schlaufman et al., 2009) are axisymmetrically unstable. However, they suggest that an approximate scaling analysis based on a representative length-scale $\sim H$ may not be sufficiently accurate to evaluate the axisymmetric stability of a disk, which depends on the detailed shape of the density profile. In addition, since both the vertical structure and the entropy stratification of the disk can influence its stability when sharp features are present, a careful treatment of the disk thermodynamics may be required. The extent to which density features can or cannot grow to be as sharp as a disk scale height may significantly affect planetary migration because differential Lindblad torques are also applied over a length-scale $\sim H$ (e.g. Ward, 1997; Matsumura et al., 2007) and co-rotation torques are very sensitive to the local density (Masset et al., 2006) and thermodynamic (Paardekooper & Papaloizou, 2008) conditions. For those disks which develop unstable density profiles as a result of slow viscous evolution, for instance mass pile-up in a magnetically dead zone, we have proposed that Rayleigh adjustment schemes be implemented. Although more detailed work would be needed to incorporate such a scheme within the framework of a viscous disk solver, our goal is to suggest that this type of adjustment schemes can be used to evolve more consistently disks with sharp features on viscous evolutionary time-scales.

Finally, we remark that our discussion has been restricted to the stability of axisymmetric perturbations in protoplanetary disks. It has been suggested that disks with narrow density features are also susceptible to non-axisymmetric instabilities (Li et al., 2000, 2001; Lyra et al., 2009). To the extent that such instabilities lead to mass diffusion on a fast dynamical time-scale, it should be possible to model their effects on disk evolutionary time-scales with an adjustment scheme similar to the one proposed here.

Chapter 3

Planetesimal and Protoplanet Dynamics in a Turbulent Protoplanetary Disk: Ideal Unstratified Disks[1]

As discussed in Chapter 1, the turbulent nature of protoplanetary disks might lead to scenarios for the formation and migration of planetesimals and planetary cores that are rather different from those suggested for the better-studied case of a laminar disk. On one hand, density fluctuations in magneto-rotational turbulence may induce significant radial diffusive migration such that some protoplanets may survive from rapid inward type I migration (JGM06; Adams & Bloch 2009). On the other hand, IGM08 argued that the eccentricities of kilometer-sized planetesimals excited by the turbulence drives significant orbital crossing such that they suffer from collisional destruction.

The survivability of planetesimals or protoplanets under type I migration or collisional destruction sensitively depends on their orbital dynamics in a turbulent gas disk. Previous direct orbital integrations of planetesimals or protoplanets embedded in a turbulent gas disk were conducted in global disk models (LSA04; N05; OIM07; IGM08). In contrast to global disk models, it can be advantageous to employ the local shearing box approximation (e.g., Goldreich & Lynden-Bell, 1965; Hawley et al., 1995; Brandenburg et al., 1995) because of its high resolving power on turbulence structures and the possibility of integrating for long times. Nelson & Papaloizou (2004) and OMM07 first measured the stochastic torques generated by

[1]The research reported in this chapter was published in Yang et al. (2009)

hydromagnetic turbulence at the center of a local shearing box. In this paper, we pursue this topic further by using direct orbital integration of planetesimals moving as massless particles under the gravitational influence of MRI-driven turbulence in a local shearing box. We focus our attention on unstratified disks in the context of ideal magnetohydrodynamics (MHD). To maintain a nonzero, numerically convergent level of stochastic perturbations driven by the MRI, we impose a constant vertical magnetic flux. We describe our numerical models in Section 3.1 and present the simulations in Section 3.2, along with statistical analyses of the disk properties and the planetesimal orbits. In Section 3.3, we use our results to revisit the issue of survivability of planetesimals and planetary cores, before reaching our conclusions in Section 3.4.

3.1 Numerical Modeling

We use the parallelized, cache-efficient, Pencil Code described by Brandenburg & Dobler (2002). It solves the non-ideal MHD Equations by sixth-order finite differences in space and third-order Runge-Kutta steps in time. The induction Equation is solved using the magnetic vector potential $\boldsymbol{A}$ so that zero divergence of magnetic field $\boldsymbol{B}$ is guaranteed at all time. To save memory usage, the Runge-Kutta time integration is performed using the $2N$-method (Williamson, 1980). The scheme is not written in conservative form. Instead, conserved quantities like total mass are monitored to evaluate the quality of the solution. In the following subsections, we describe the Equations assumed in our models as well as the numerical constructs.

3.1.1 Magnetohydrodynamics

We use the local shearing box approximation (e.g., Goldreich & Lynden-Bell, 1965; Brandenburg et al., 1995; Hawley et al., 1995) to simulate a small Cartesian box carved out of a Keplerian disk at a large distance from the host star. The center of the box co-rotates with the disk at Keplerian angular speed Ω_K, the x-axis is directed radially, and the y-axis is directed azimuthally. The vertical component of gravity from the host star is ignored and thus the disk is unstratified. We impose a vertical, external magnetic field $\boldsymbol{B}_{\rm ext} = B_{\rm ext}\hat{\boldsymbol{z}}$ to

maintain a finite magnetic flux. The MHD Equations then become

$$\partial_t \rho - \frac{3}{2}\Omega_K x \partial_y \rho + \nabla \cdot (\rho \boldsymbol{u}) = f_D + \nabla \cdot (\nu_s \nabla \rho), \tag{3.1}$$

$$\partial_t \boldsymbol{u} - \frac{3}{2}\Omega_K x \partial_y \boldsymbol{u} + \boldsymbol{u} \cdot \nabla \boldsymbol{u} = -\frac{1}{\rho}\nabla p + \left(2\Omega_K u_y \hat{\boldsymbol{x}} - \frac{1}{2}\Omega_K u_x \hat{\boldsymbol{y}}\right) + \frac{1}{\rho}\boldsymbol{J} \times (\boldsymbol{B} + \boldsymbol{B}_{\rm ext}) + \boldsymbol{f}_V + \frac{1}{\rho}\nabla (\nu_s \rho \nabla \cdot \boldsymbol{u}), \tag{3.2}$$

$$\partial_t \boldsymbol{A} - \frac{3}{2}\Omega_K x \partial_y \boldsymbol{A} = \frac{3}{2}\Omega_K A_y \hat{\boldsymbol{x}} + \boldsymbol{u} \times (\boldsymbol{B} + \boldsymbol{B}_{\rm ext}) + \boldsymbol{f}_R - \eta_s \boldsymbol{J}, \tag{3.3}$$

in which ρ is gas density, $\boldsymbol{u}$ is gas velocity relative to the background shear flow, p is gas pressure, $\boldsymbol{J} = \nabla \times \boldsymbol{B}/\mu_0$ is the electric current density, $\boldsymbol{B} = \nabla \times \boldsymbol{A}$, and μ_0 is permeability. The terms f_D, $\boldsymbol{f}_V$, and $\boldsymbol{f}_R$, and those containing scalar variables ν_s and η_s are numerical dissipation terms needed to stabilize the scheme, which are described below. They are needed to resolve shocks, and because the difference scheme formally has vanishing dissipation. We assume an isothermal Equation of state, $p = c_s^2 \rho$, where c_s is the isothermal speed of sound.

The mass diffusion term $\nabla \cdot (\nu_s \nabla \rho)$ in the continuity Equation (3.1) and the bulk viscosity term $\nabla (\nu_s \rho \nabla \cdot \boldsymbol{u})/\rho$ in the momentum Equation (3.2) are implemented to broaden shocks. The artificial kinematic viscosity ν_s is of von Neumann type (c.f., Haugen et al., 2004; Lyra et al., 2008):

$$\nu_s = \begin{cases} -h^2 \nabla \cdot \boldsymbol{u}, & \text{if} \quad \nabla \cdot \boldsymbol{u} < -c_s/4h, \\ 0, & \text{otherwise}, \end{cases} \tag{3.4}$$

where h is grid spacing. It is smoothed by taking a maximum over nearest neighbors and then convolved with a Gaussian kernel having a standard deviation of h. Note that the threshold for the velocity divergence is set for eliminating artificial diffusion where hydrodynamic shocks are unlikely to be present.

We also include the Ohmic term $-\eta_s \boldsymbol{J}$ in the induction Equation (3.3) to broaden strong current sheets. The artificial resistivity η_s assumes the same form used by Nitta et al. (2001) but with a lower cutoff:

$$\eta_s = \begin{cases} \mu_0 h v_A, & \text{if} \quad v_A > 8c_s, \\ 0, & \text{otherwise}, \end{cases} \tag{3.5}$$

where $v_A = |\boldsymbol{B} + \boldsymbol{B}_{\rm ext}|/\sqrt{\mu_0 \rho}$ is the Alfvén speed. Although simple, this form may perform better to resolve sharp magnetic structures than a resistivity proportional to the magnitude of current density itself (Fragile et al., 2005). We apply a lower cutoff in Equation (3.5) to only treat regions where fast magnetic reconnection may occur.

In addition to applying artificial diffusions addressing shocks and current sheets, we also implement hyper-diffusion f_D, hyper-viscosity $\boldsymbol{f}_V$, and hyper-resistivity $\boldsymbol{f}_R$ in the respective MHD Equations (3.1)–(3.3) (e.g., Haugen & Brandenburg, 2004; Johansen & Klahr, 2005):

$$f_D = \nu_3 \nabla^6 \rho, \quad \boldsymbol{f}_V = \nu_3 \left(\nabla^6 \boldsymbol{u} + \mathbf{S} \cdot \nabla \ln \rho \right), \quad \text{and} \quad \boldsymbol{f}_R = \nu_3 \nabla^6 \boldsymbol{A}, \tag{3.6}$$

where ν_3 is a constant, the tensor $\mathbf{S}$ is defined by $S_{ij} \equiv \partial_j^5 u_i$, and the sixth-order differential operator $\nabla^6 \equiv \partial_x^6 + \partial_y^6 + \partial_z^6$. These terms are included in order to stabilize the high-order finite-difference scheme implemented by the Pencil Code. The corresponding diffusivity is proportional to k^6, where k is the wavenumber of a signal in the simulation, so features at small scales dissipate at a much higher rate than those at larger scales. Therefore, by adjusting the coefficient ν_3, we can maintain numerical stability by damping oscillations near the grid scale while still preserving much of the inertial range of the modeled turbulence resolved in the simulation. In our models, we choose ν_3 such that the mesh Reynolds number

$$\mathrm{Re}_{\mathrm{mesh}} \equiv \frac{u_{\max}}{\nu_3} \left(\frac{h}{\pi} \right)^5 \lesssim 1, \tag{3.7}$$

where $u_{\max}$ is the absolute maximum of u over the computational domain. This criterion states that dissipation at the Nyquist frequency should be comparable to or stronger than gas advection. Note that since all the adopted hyper-diffusive terms have the same coefficient ν_3, the effective magnetic Prandtl number $\mathrm{Pr}_{M,\mathrm{eff}} \equiv \mu_0 \nu_{\mathrm{eff}} / \eta_{\mathrm{eff}}$ in our simulations should be reasonably close to unity, where ν_{eff} and η_{eff} are the effective viscosity and resistivity in the simulations, respectively.

3.1.2 Particle Dynamics

In this work, we consider particles of zero mass to study the effect of hydromagnetic turbulence on the orbital properties of planetesimals. Although simple, this offers a good approximation for kilometer-sized planetesimals as they are large enough that gaseous drag force can be neglected, but small enough that type I migration does not dominate. For the approximation to be valid, the mass of a particle must lie between roughly 10^{14} g and 10^{26} g, corresponding to a size range of about 0.1–1000 km (OMM07). Furthermore, if the action of hydromagnetic turbulence on the particles is separable from effects due to other interactions, our measurements can be applied to all stages of planet formation.

In our models, therefore, we consider particles moving under only the gravitational influence of the host star and that of the protoplanetary gas disk. We ignore drag forces between the particles and the gas and the gravity of the particles. Because the particles exert no force on the gas or themselves, no migration torques act. Given deterministic Keplerian shear flow and epicycle motions, deviations in particle trajectories due to turbulent fluctuations in the gas can easily be isolated.

Under these assumptions, the Equations of motion for each particle become

$$\frac{\mathrm{d}\boldsymbol{x}_p}{\mathrm{d}t} = \boldsymbol{u}_p - \frac{3}{2}\Omega_K x_p \hat{\boldsymbol{y}}, \tag{3.8}$$

$$\frac{\mathrm{d}\boldsymbol{u}_p}{\mathrm{d}t} = \left(2\Omega_K u_{p,y}\hat{\boldsymbol{x}} - \frac{1}{2}\Omega_K u_{p,x}\hat{\boldsymbol{y}}\right) - \nabla\Phi. \tag{3.9}$$

The vector $\boldsymbol{x}_p$ is the position of the particle in the shearing box, while $\boldsymbol{u}_p$ is the velocity of the particle relative to the background shear flow. The scalar variable Φ is the gravitational potential of the gas, which is the solution of the Poisson Equation (Goldreich & Lynden-Bell, 1965):

$$\left[\left(\partial_x + \frac{3}{2}\Omega_K t\partial_y\right)^2 + \partial_y^2 + \partial_z^2\right]\Phi = 4\pi G\rho, \tag{3.10}$$

where G is the gravitational constant.

Sheared, periodic boundary conditions (Hawley et al., 1995) are adopted for the solution of Equation (3.10). The system is strictly periodic in the y- and z-directions while the x-direction requires special treatment. Since the yz-plane at any given x moves with the Keplerian shear flow, the lower x-boundary plane should be imaged by the upper x-boundary plane shifted by $-3\Omega_K L_x \delta t/2$ in the y-direction, where δt is the time step and L_x is the x-dimension of the computational domain. In mathematical notation, $\rho(x, y, z) = \rho(x + L_x, y - 3\Omega_K L_x \delta t/2, z)$. Rather than interpolating $\rho(x, y, z)$ in real space to obtain sheared periodicity, we use Fourier interpolation when solving Equation (3.10) in Fourier space (see Johansen et al., 2007, Supplementary Information).[2]

The position $\boldsymbol{x}_p$ and velocity $\boldsymbol{u}_p$ of each particle is updated by solving the Equations of motion (3.8) simultaneously with the third-order Runge-Kutta steps for the MHD Equations (3.1)–(3.3). In addition to the Courant conditions set by the MHD Equations, the time

[2]This technique was originally suggested by Colin McNally at `http://imp.mcmaster.ca/ colinm/ism/rotfft.html`.

step is limited by the absolute maximum of Equation (3.8) such that no particles can cross more than half the zone size in one time step. We compute the gradient of the potential $\nabla\Phi$ on the grid after solving Equation (3.10) and then quadratically interpolate it to the position of each particle in the calculation of Equation (3.9).

3.1.3 Code Units and Scaling Relations

We define the length and the time units as the vertical scale height H and the orbital period $P = 2\pi/\Omega_K$, respectively, at the center of our local shearing box located at an arbitrary distance to the host star R. Since vertical hydrostatic equilibrium of isothermal gas requires that $H = \sqrt{2}c_s/\Omega_K$, the speed of sound is fixed at $c_s = \pi\sqrt{2}$. Note that this choice makes the system invariant with temperature.

We adopt two different mass units such that $\rho_0 = (4\pi GP^2)^{-1}$ and $\rho_0 = (GP^2)^{-1}$ for a low-mass and a high-mass disk, respectively, where ρ_0 is the uniform initial gas density. For these two disk models, the Toomre Q parameter for the gas is $Q_g = c_s\Omega_K/\pi G\Sigma = 63$ and 5.0, respectively, where $\Sigma = \sqrt{\pi}\rho_0 H$ is the column density.[3] The gas disks in our models are gravitationally stable and thus we ignore gas self-gravity. For convenience, we define a dimensionless parameter

$$\xi \equiv 4\pi G\rho_0 P^2 = 4(2\pi)^{3/2}/Q_g \tag{3.11}$$

as a measure of the strength of disk gravity. For our low-mass and high-mass disks, $\xi = 1$ and 4π, respectively.

In physical units, ρ_0 is given by the following scaling relation:

$$\rho_0 = \left(1.2 \times 10^{-9}\ \mathrm{g\ cm^{-3}}\right)\xi\left(\frac{P}{\mathrm{yr}}\right)^{-2} = \left(1.2 \times 10^{-9}\ \mathrm{g\ cm^{-3}}\right)\xi\left(\frac{M_\star}{M_\odot}\right)\left(\frac{R}{\mathrm{AU}}\right)^{-3},$$

where $M_\star$ is the mass of the host star. The corresponding column density is

$$\Sigma = \left(1.5 \times 10^{3}\ \mathrm{g\ cm^{-2}}\right)\xi\left(\frac{c_s}{10^5\ \mathrm{cm\ s^{-1}}}\right)\left(\frac{P}{\mathrm{yr}}\right)^{-1}. \tag{3.12}$$

These scaling relations describe families of disk models to which our results apply. In particular, at 1 AU around a solar-type star, the column density of our low-mass disk is roughly consistent with that of the classical minimum mass solar nebula (MMSN; Hayashi, 1981).

[3]Strictly speaking, this relation only holds for stratified disks. Comparison between stratified and unstratified disk models will be made in a subsequent study.

Finally, the derived units of magnetic field and vector potential are $\mu_0^{1/2}\rho_0^{1/2}HP^{-1}$ and $\mu_0^{1/2}\rho_0^{1/2}H^2P^{-1}$, respectively. We arbitrarily set the permeability $\mu_0 = 1$. The magnetic energy density associated with $B = 1$ is then $1/(4\pi^2)$ of the initial pressure $p_0 = c_s^2\rho_0$.

3.1.4 Initial and Boundary Conditions

The initial conditions for our models are the following. The gas density is uniform ($\rho = \rho_0$) while the magnetic vector potential is set to zero ($\boldsymbol{A} = 0$). An external vertical magnetic field is imposed, ranging from $B_{\rm ext} = 0.01$ to 0.64. The corresponding plasma $\beta \equiv 2\mu_0\rho c_s^2/B^2$ ranges from 3.9×10^5 to 96. Gaussian noise in gas velocity of amplitude 10^{-3} is imposed to seed the MRI.

As noted in Section 3.1.2, the boundary conditions for all dynamical variables are sheared periodic and we find values for the ghost zones using Fourier interpolation. Our fiducial model has a computational domain of $2 \times 2 \times 2H$, but we also study domains with sizes up to $8 \times 8 \times 2H$. The highest resolution we use is 64 grid points per disk scale height H.

The coefficient ν_3 of the hyper-diffusive terms discussed in Section 3.1.1 needs to be fine-tuned such that the mesh Reynolds number $\mathrm{Re}_{\rm mesh}$ is as close to unity as possible during the course of the simulation (Equation (3.7)). We adopt an iterative approach to determine the optimal value of ν_3, using $\mathrm{Re}_{\rm mesh} \sim 1$. For the case of $B_{\rm ext} = 0.08$ ($\beta_{\rm ext} = 6.2 \times 10^3$) with a $2 \times 2 \times 2H$ box at a resolution of 64 points per scale height, we choose $\nu_3 = 2.9 \times 10^{-11}$ for which $u_{\rm max} \simeq 6.0 \pm 2.7$ at saturation level, where the deviation of $u_{\rm max}$ is given by 3σ in its time variation.

We uniformly distribute 32^3 particles in the entire computational domain. We do not allow them to move until time $t = t_0$ after which the hydromagnetic turbulence has saturated and approached a statistically steady state. For the case of $B_{\rm ext} = 0.08$ ($\beta_{\rm ext} = 6.2 \times 10^3$), we choose $t_0 = 20P$ (see Section 3.2.1). Then the particles are set to initially move relative to the background shear flow such that they have an initial eccentricity of e_0 and start at the apogee of their orbits, i.e.,

$$\boldsymbol{u}_{p,0} = -\frac{1}{2}H\Omega_K\left(\frac{e_0}{H/R}\right)\hat{\boldsymbol{y}} \tag{3.13}$$

(see Appendix A). We wrap a particle around when it moves beyond any of the six boundary

planes.

We remark that each model presented in the following section is just one realization of the stochastic nature of the turbulence, corresponding to one set of initial velocity perturbations of the gas. The similarity in particle orbital evolutions found across several models are due to closeness of the random number sequences used to generate the velocity perturbations and thus similar initial conditions for the gas.

3.2 Simulation Results

3.2.1 Convergence of Turbulence Properties

Grid Resolution

We first present a study of the convergence with increasing numerical resolution of the properties of the turbulence important to our work. We work on a $2 \times 2 \times 2H$ grid for this study to reach maximum resolution. Figure 3.1 plots density perturbation $\Delta\rho/\rho_0$, inverse plasma β, and the Shakura & Sunyaev (1973) α-parameter as a function of time t for disks with an external magnetic field of $B_{\rm ext} = 0.08$ ($\beta_{\rm ext} = 6.2 \times 10^3$) at resolutions up to 64 grid points per disk scale height H, where $\Delta\rho \equiv \rho - \rho_0$. The density perturbation $\Delta\rho/\rho_0$ shown is the rms value over the computational domain while the inverse plasma β shown is the volume-averaged value. The α-parameter is calculated from the combined effects due to the Reynolds and Maxwell shear stresses (e.g., Brandenburg, 1998):

$$\alpha = \frac{\sqrt{2}}{3} \frac{\langle \rho u_x u_y - B_x B_y/\mu_0 \rangle}{\rho_0 c_s^2}, \tag{3.14}$$

where the bracket $\langle\rangle$ denotes the volume average over the entire computational domain. As shown in Figure 3.1, the MRI saturates and remains roughly steady after about $t = 20P$. After saturation, all three properties exhibit only small changes with increasing resolution, aside from a slight trend of increasing α. The properties of the saturated turbulence appear to converge to a nonzero level, as opposed to disks without net magnetic flux (e.g., Fromang & Papaloizou, 2007).

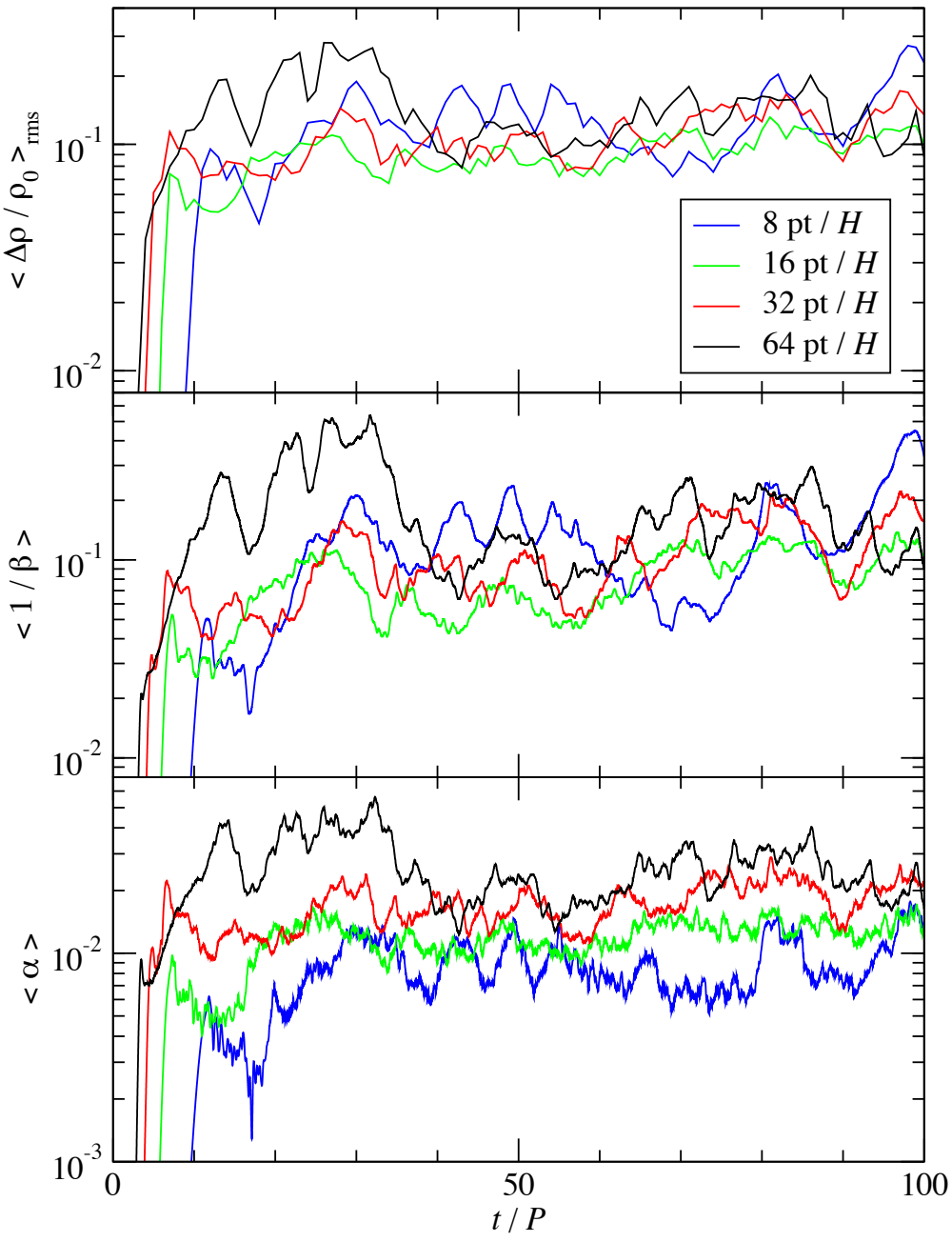

Figure 3.1 Density perturbation $\Delta\rho/\rho_0$, inverse plasma β, and α-parameter as a function of time t (in units of orbital period P) for a $2 \times 2 \times 2H$ local shearing box under an external vertical magnetic field of $B_{\rm ext} = 0.08$ ($\beta_{\rm ext} = 6.2 \times 10^3$). All properties are volume averaged over the whole computational domain with the rms value of $\Delta\rho/\rho_0$ being given. Results are shown for resolutions up to 64 points per scale height H.

Box Size

We also examine how the same averaged quantities depend on the size of our local shearing box by studying three runs done with increasing horizontal size, up to $8 \times 8 \times 2H$, at our medium resolution of 32 points per scale height. Johansen et al. (2009) ran high-resolution (with ∼137 points per scale height), unstratified models without mean field and found roughly linear growth in the effective viscosity α with box size. In Figure 3.2, we show that the plasma β and the effective α-parameter appear almost independent of box size in our models, aside from a trend toward reduced temporal fluctuations when averaged over larger boxes. The rms density perturbation $\Delta\rho/\rho_0$ shows a weak trend towards increasing at larger box size, though, with the average over the time period $20 < t/P < 120$ increasing by 26% from the smallest to the largest box, a scale change of a factor of four. This probably occurs because of the inclusion of larger-scale instability modes in the larger boxes; it is not a particularly dramatic effect, though, because the smallest box size that we study already captures the fastest growing modes. Nevertheless, this small effect seems to strongly affect particle orbital properties, as we will discuss below.

3.2.2 Vertical Net Flux Dependence

We next turn to the effect of varying external vertical magnetic field. Figure 3.3 plots the same properties of the saturated turbulence as a function of the external vertical magnetic field, represented by the inverse plasma β, for our smallest box. They are volume averaged as described above, and then time averaged over a period of at least $20P$ after saturation. Also included in the figure are the time variation of these properties, as indicated by the error bars. We confirm the general trend of increasing turbulence activity with increasing uniform vertical field (e.g., Hawley et al., 1995; Sano et al., 2004; Johansen et al., 2006). Numerical convergence can be seen over the range of the field strengths we have explored. In addition to the turbulent transport often discussed in the literature, we also report the dependence between density perturbation and external field in Figure 3.3, which may be more relevant to the orbital dynamics of particles moving in these disks. We emphasize that by varying the net vertical magnetic flux through a disk, a wide range of turbulent viscosity values can be obtained, as suggested by numerous previous works as well as Figure 3.3.

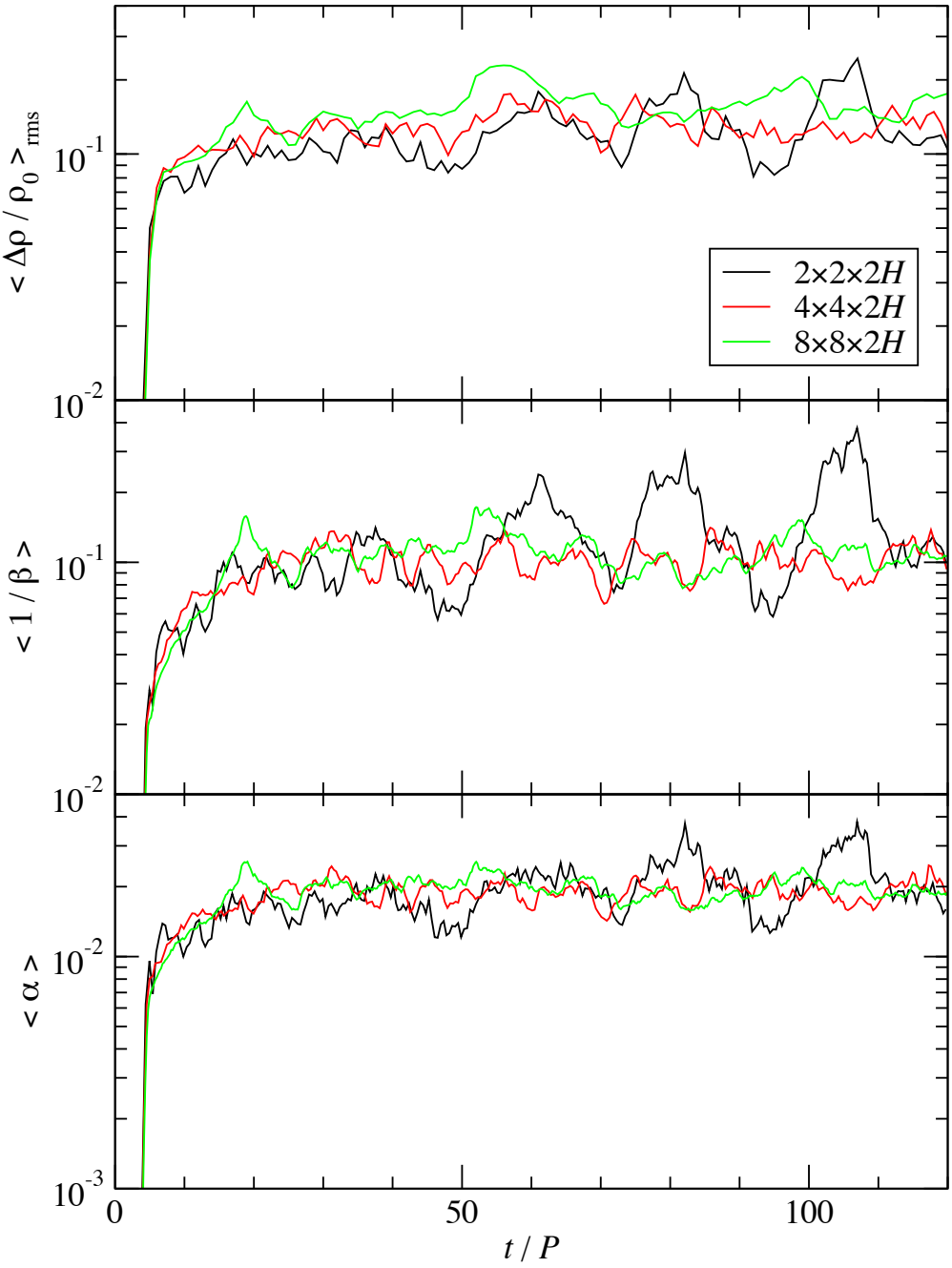

Figure 3.2 Density perturbation $\Delta\rho/\rho_0$, inverse plasma β, and α-parameter as a function of time t for three different box sizes at a resolution of 32 points per scale height H. An external vertical magnetic field of $B_{\rm ext} = 0.08$ ($\beta_{\rm ext} = 6.2 \times 10^3$) is imposed. Properties are volume averaged over the whole computational domain and the rms value for $\Delta\rho/\rho_0$ is shown.

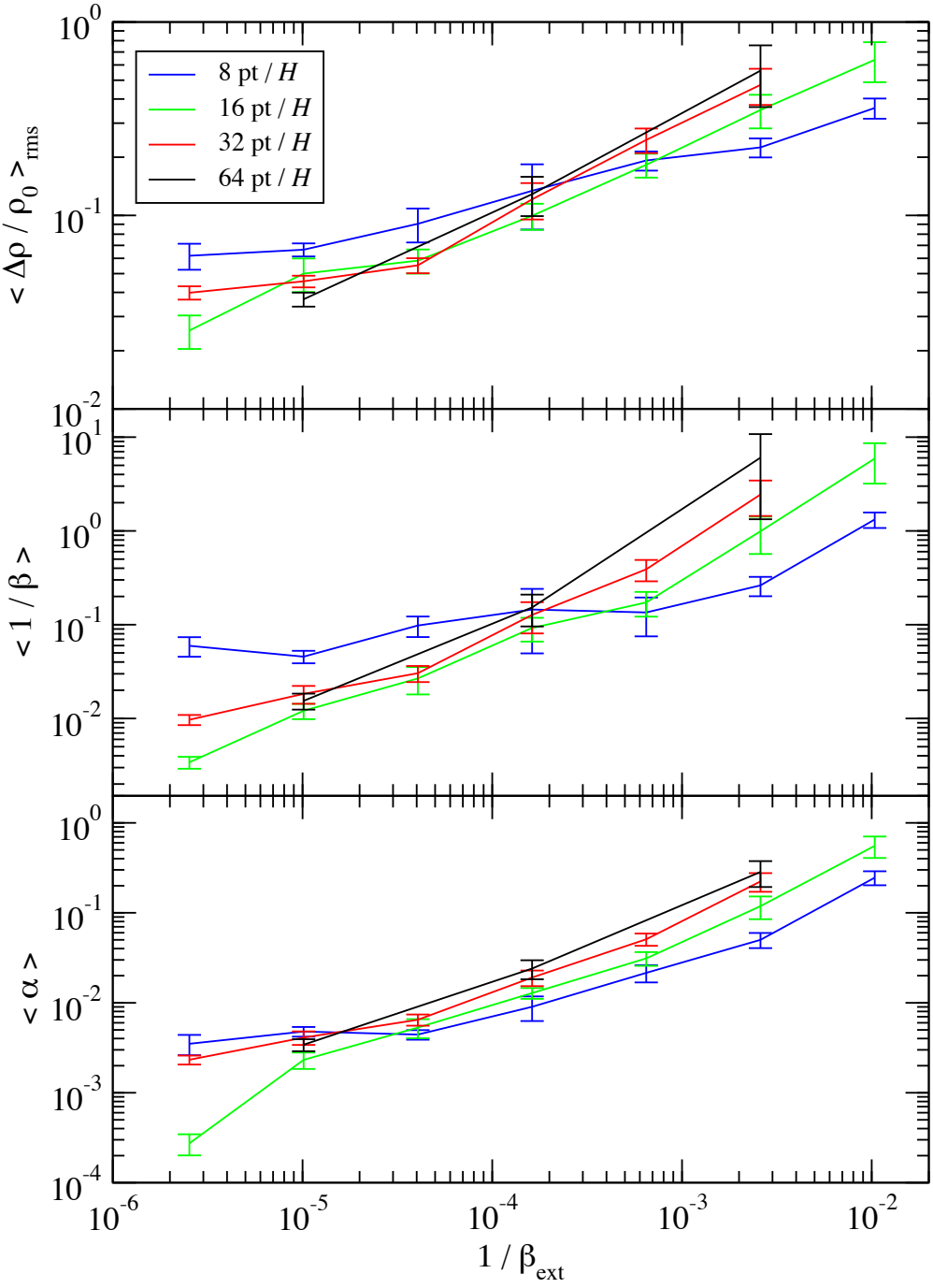

Figure 3.3 Density perturbation $\Delta\rho/\rho_0$, inverse plasma β, and α-parameter as a function of external magnetic field in terms of inverse plasma β for a $2 \times 2 \times 2H$ box. All properties are volume averaged over the whole computational domain as well as time-averaged over an interval of at least 20 orbital periods after saturation of the MRI. Results are shown for resolutions up to 64 points per scale height H. The error bars denote 1σ in time variation around the volume-averaged properties.

To best represent typical protoplanetary accretion disks, we adopt a fiducial disk model with $B_{\rm ext} = 0.08$ ($\beta_{\rm ext} = 6.2 \times 10^3$), which we run at a resolution of 64 points per scale height on a $2 \times 2 \times 2H$ grid. As shown in Figures 3.1 and 3.3, this model gives a turbulent accretion of $\alpha \sim 10^{-2}$, which is consistent with current estimates for disks around typical T Tauri stars (e.g., Hartmann et al., 1998, 2006). Note that in our fiducial model, the rms density perturbation of the gas is on the order of $\sim$10%.

3.2.3 Motion of a Single Particle

Using our fiducial model in the context of a protoplanetary disk, we now study the orbital dynamics of zero-mass particles moving in this turbulent environment. As demonstrated in Figure 3.4, a particle moving under gravity of the turbulent gas undergoes epicycle motion horizontally as well as continuous change in its mean radius. We define the radial drift of each particle as $\Delta x \equiv \bar{x} - x_0$, where $\bar{x}$ is the mean radial position over one orbital period (as exemplified by the red line in Figure 3.4) and x_0 is the initial radial position. Given that $x \ll R$, the eccentricity of each particle can be approximated by $e \approx (x_{\rm max} - x_{\rm min})/2R$, where $x_{\rm max}$ and $x_{\rm min}$ are the maximum and the minimum radial positions in one epicycle, respectively. With these two quantities, we can measure the orbital migration and eccentricity change of planetesimals induced by hydromagnetic turbulence.

Figure 3.5 shows the change of radial drift and eccentricity with time for four randomly selected particles. It is evidently a stochastic process and the final outcome can be quite different with slightly different initial conditions. Nevertheless, statistical methods can be employed to quantify the process. We discuss the statistical evolution of these orbital properties in the following subsections.

3.2.4 Radial Drift

Histograms of the distribution of radial drifts at three different times in the low-mass disk version of our fiducial model are plotted in Figure 3.6. The distribution of particles in radial drift resembles a normal distribution with its center located at approximately zero. This is not surprising since there is no preferred direction locally for the turbulence to generate a net torque. More interestingly, the width of the distribution increases with time. Although the

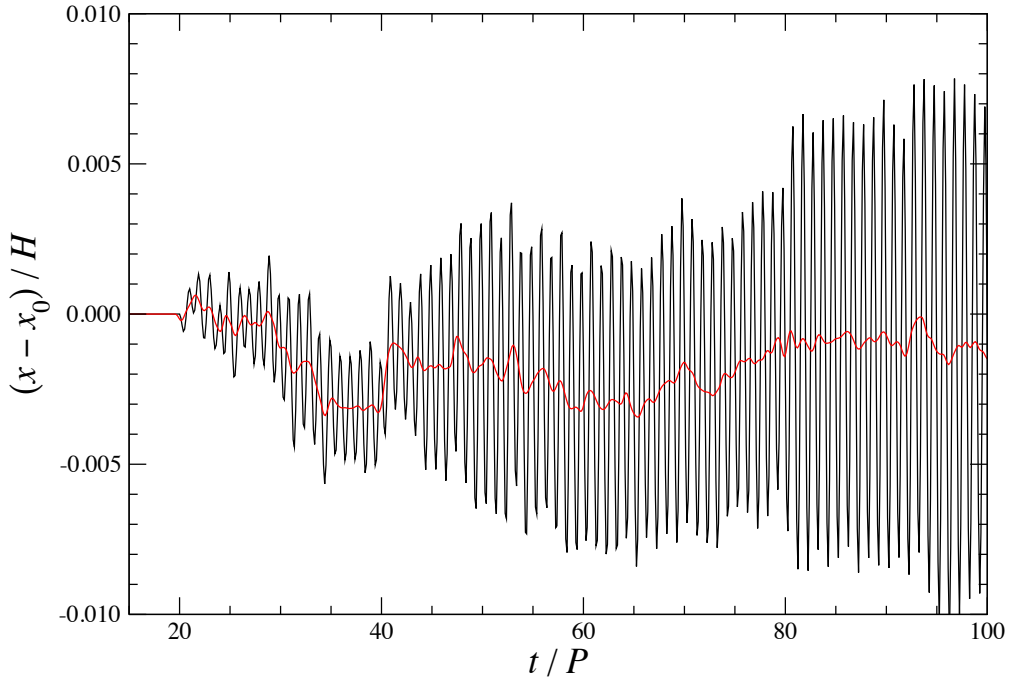

Figure 3.4 Radial motion of one representative particle with initial eccentricity $e_0 = 0$ moving in the low-mass disk version of our fiducial model. The *black* line shows its radial displacement $x - x_0$ from initial position x_0 as a function of time t. The *red* line shows the corresponding radial drift, defined as the running average over one epicycle, i.e., one orbital period P.

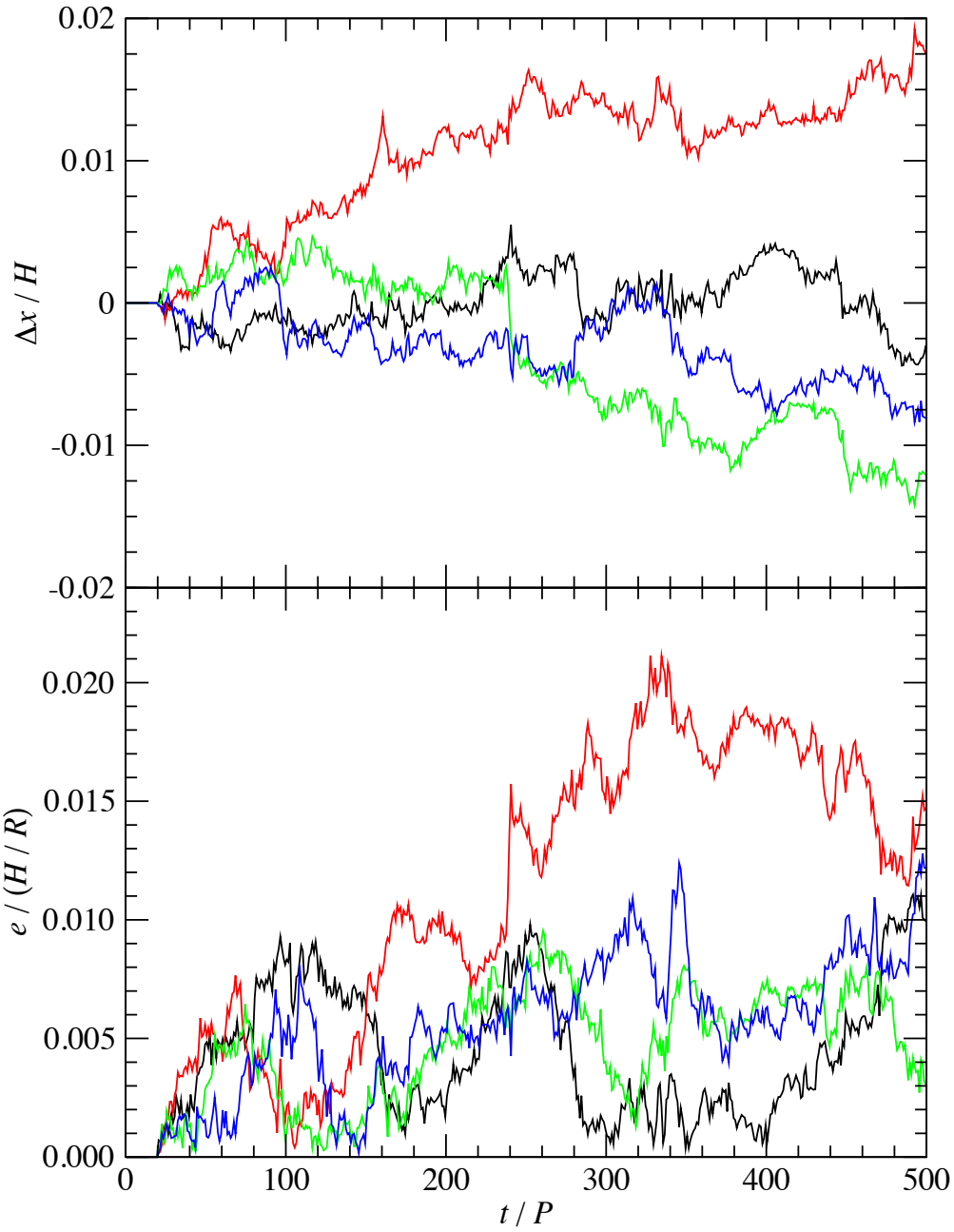

Figure 3.5 Time evolution of radial drift Δx (*top* panel) and eccentricity e (*bottom* panel) for four randomly selected particles with initial eccentricity $e_0 = 0$ moving in the low-mass disk version of our fiducial model. The eccentricity is in terms of H/R, the ratio of one disk scale height to the distance of the shearing box to the host star.

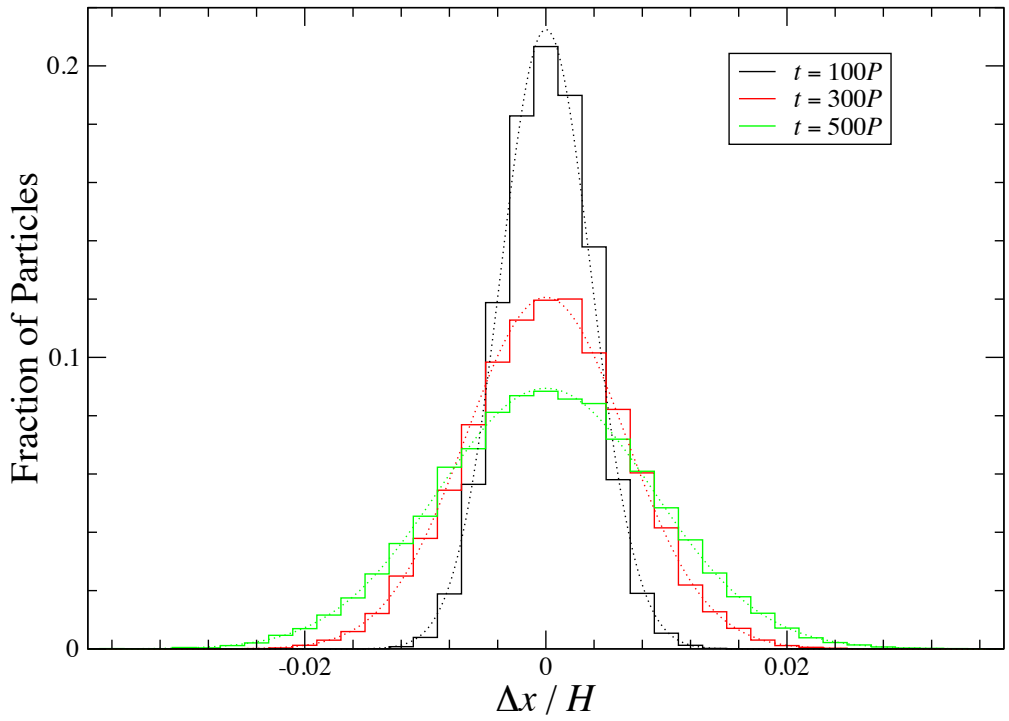

Figure 3.6 Distribution of particle radial drifts Δx at three different times in our fiducial model. These particles have initial eccentricity $e_0 = 0$ and evolve in a low-mass disk. The dotted lines are best fits in the form of normal distributions.

hydromagnetic turbulence has no net effect on the orbital radius of the particles, it becomes more and more likely for any single particle to drift away from its original orbit as time increases. This could help a subset of particles to survive type I migration, as suggested by JGM06 and Adams & Bloch (2009).

Figure 3.7 shows the standard deviation of radial drift $\sigma(\Delta x)$ as a function of elapsed time $\Delta t \equiv t - t_0$ for particles with different initial eccentricity e_0 moving in different strengths of disk gravity ξ in our fiducial model. The standard deviation steadily increases with time, with little difference between particles of different initial eccentricities. Power-law fitting results in time indices of about 0.52–0.58, just slightly larger than 1/2. This confirms the proposition that gravitational influence of the hydromagnetic turbulence makes particles undergo random walks (LSA04; Nelson & Papaloizou 2004; N05) and the resulting orbital evolution can be described as a diffusion process (JGM06; OIM07; Adams & Bloch, 2009; Rein & Papaloizou, 2009).

We measure the dependence of radial drift on disk gravity, as quantified by the dimen-

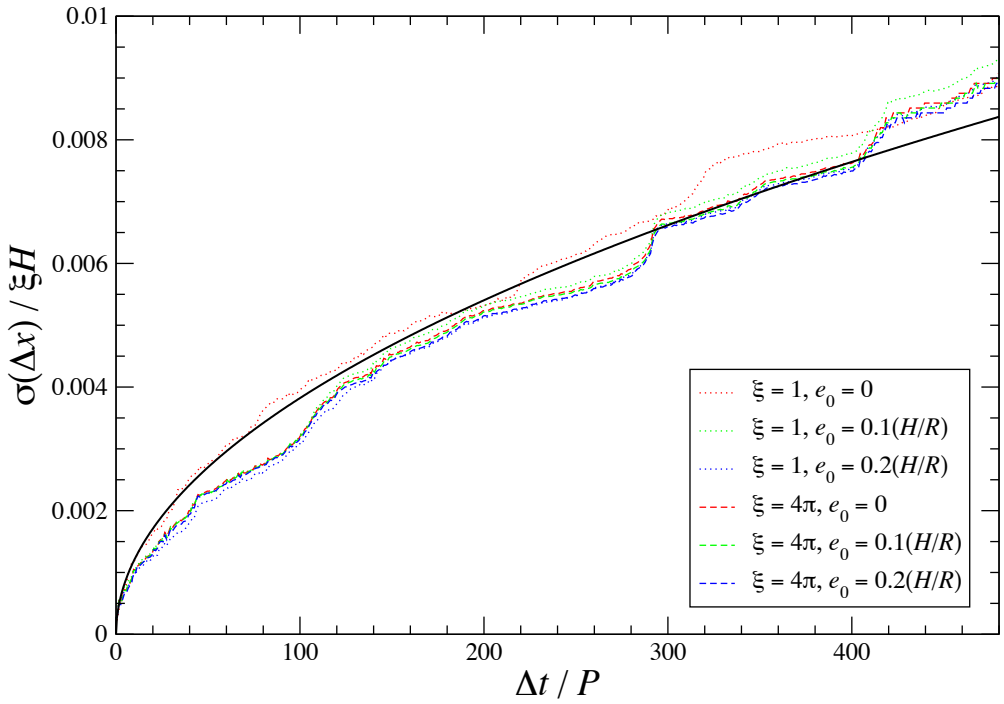

Figure 3.7 Standard deviation of radial drift $\sigma(\Delta x)$ as a function of elapsed time Δt in our fiducial model. The *dotted* lines are obtained from low-mass disks ($\xi = 1$) while the *dashed* lines are from high-mass disks ($\xi = 4\pi$). Particles with initial eccentricities $e_0 = 0$, $0.1(H/R)$, and $0.2(H/R)$ are denoted by *red*, *green*, and *blue* lines, respectively. The *black solid* line is the best fit to all six curves.

sionless parameter ξ, by comparing the results from our low-mass and high-mass disk models (see Section 3.1.3). As demonstrated in Figure 3.7, radial drifts in these models roughly coincide after being scaled with ξ, indicating a dependence close to linear. By assuming that $\sigma(\Delta x)$ scales with $\xi \Delta t^{1/2}$, our best fit to the results shown in Figure 3.7 is

$$\sigma(\Delta x) = (3.8 \pm 0.4) \times 10^{-4}\, \xi H \left(\frac{\Delta t}{P}\right)^{1/2} . \tag{3.15}$$

The size of the computational domain of a local shearing box does have a rather substantial effect on the magnitude of the random walk, and thus the diffusion derived from this model, as shown in Figure 3.8. Increasing the horizontal size of the box by a factor of four results in almost an order of magnitude increase in the standard deviation of the radial drift at each time. In contrast to gas properties discussed in Section 3.2.1, we have not seen convergence of the magnitude of the orbital random walk with box size in our study.

Our largest box shows an amplitude of the random walk roughly a factor of three smaller

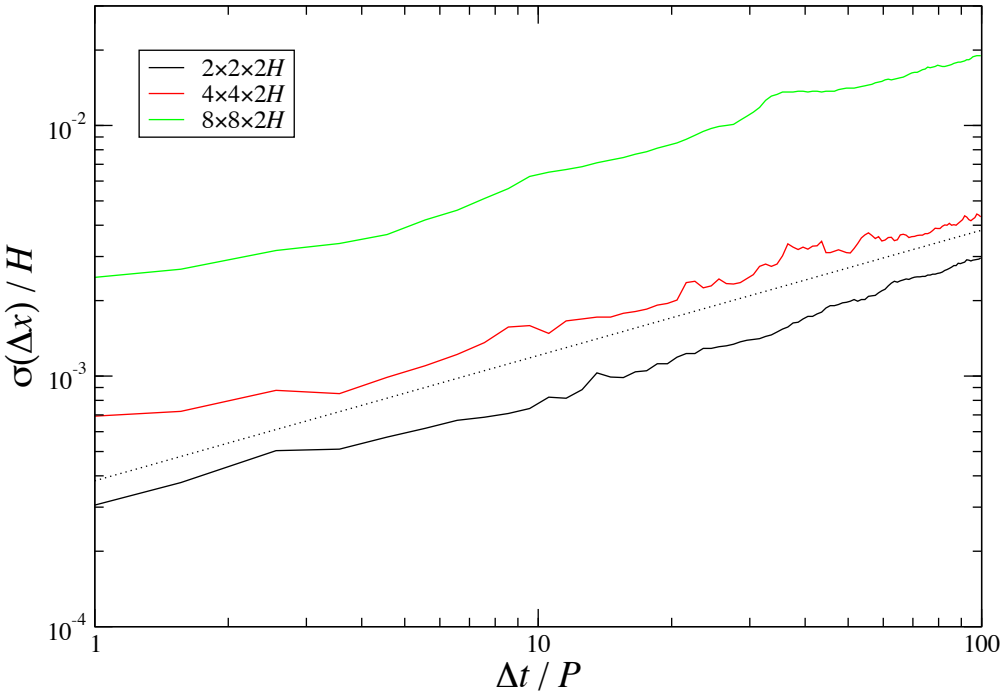

Figure 3.8 Standard deviation of radial drift $\sigma(\Delta x)$ as a function of elapsed time Δt for three different box sizes at a resolution of 32 points per scale height H (*solid* lines), where only the low-mass disk model ($\xi = 1$) and particles with zero initial eccentricity are considered. For comparison, the straight *dotted* line gives the best fit to the high-resolution model shown in Figure 3.7 (Equation (3.15)).

than seen in the global model described by N05. We make this estimate by examining his Figure 4. This shows the semi-major axis for six zero-mass particles at different radii R over a period of time of roughly 100 orbits in the relevant region of 2–3 times the inner edge of his grid, at $R = R_1$, in a disk with $H \simeq 0.1R$. The standard deviation of $\Delta x/\xi H$ of the particles at $\Delta t \simeq 90P$ is roughly 0.06, where P is the orbital period at the respective initial radii of the particles and the relevant disk-gravity parameter $\xi \simeq 0.9\,(R/R_1)^2$ (R. P. Nelson 2009, private communication). By comparison, the result for our $8 \times 8 \times 2H$ box shown in Figure 3.8 gives $\sigma(\Delta x)/H \simeq 0.02$ at $\Delta t \simeq 90P$.

On the other hand, OIM07 found results roughly consistent with our fiducial disk model. These authors used orbital integrations of particles influenced by torques given by a heuristic, stochastic formula for hydromagnetic turbulence, and the formula was suggested by LSA04 based on zero net flux, global disk, MHD simulations. The disk models OIM07 studied were about 10–100 times less massive than the MMSN, but they reported their scaling with varying disk mass. By extrapolating their results to values appropriate for our low-mass disk model with $\xi = 1$, and considering their fiducial magnitudes for the stochastic torques, we find that our measured spread of radial drift (Equation (3.15)) is roughly consistent with theirs at 1 AU. As discussed by these authors, large uncertainty in their results might be involved, mostly due to the uncertainty in the magnitude of the stochastic torques and their neglecting the power given by LSA04 in the $m = 1$ mode (where the integer m represents the Fourier decomposition of density structure in azimuthal angle rather than the spiral mode used in density wave theories).

3.2.5 Eccentricity

Figure 3.9(a) shows the histograms of eccentricity at three different times for particles with initial eccentricity $e_0 = 0$ moving in the low-mass version of our fiducial disk model.[4] The distributions appear close to a Rayleigh distribution:

$$f(e) = \left(\frac{e}{\sigma^2}\right) \exp\left(-\frac{e^2}{2\sigma^2}\right), \tag{3.16}$$

[4]We remark that the mean eccentricity of particles with initial eccentricity $e_0 = 0$ is about $0.012(H/R)$ and $0.16(H/R)$ at $t = 500P$ for the low-mass and the high-mass disk models, respectively. These eccentricities correspond to epicycle motions covering about 1.5 and 20 grid zones in the radial direction, enough to resolve the gravitational forces experienced by the particles.

where σ is a constant proportional to both the peak and the width of the distribution. The standard deviation of this distribution is given by $\sqrt{(4-\pi)/2}\,\sigma$. As shown in Figure 3.9(a), both the eccentricity at the peak value and the width of the distribution increase with time, so it at first appears that eccentricity is excited by hydromagnetic turbulence. Such eccentricity growth was also reported by N05 and OIM07.

However, we find a different distribution for particles with nonzero initial eccentricity in the same model. Figure 3.9(b) shows the histograms of eccentricity deviation $\Delta e \equiv e - e_0$ at three different times for particles with initial eccentricity $e_0 = 0.1(H/R)$. They are similar to a normal distribution with a constant mean, implying that the average eccentricity of these particles remains constant at the initial eccentricity (see also OIM07). The width of the distribution does increase with time. Therefore, hydromagnetic turbulence does not just excite the eccentricity of particles; it can also act to damp the existing eccentricity of some particles. The distribution found for particles with $e_0 = 0$ is just a special case of this general behavior: since eccentricity is a positive definite quantity and the initial eccentricity is zero, it is no surprise that a normal distribution for the eccentricity deviation, $f(\Delta e) = \exp\left(-\Delta e^2/2\sigma^2\right)/\sqrt{2\pi}\sigma$, manifests as a Rayleigh distribution for the eccentricity itself (Equation (3.16)).

Figure 3.10 shows the standard deviation of eccentricity deviation $\sigma(\Delta e)$ as a function of elapsed time Δt measured for our fiducial model. Note that to be consistent with a normal distribution as discussed above, we have multiplied the standard deviation measured for particles with $e_0 = 0$ by a factor of $\sqrt{2/(4-\pi)}$. As in the case of radial drift discussed in Section 3.2.4, little difference exists between particles with different initial eccentricities and the results scale linearly with the dimensionless parameter ξ, which measures the strength of the disk gravity. Chi-square fitting with a $\xi \Delta t^{1/2}$ dependence to the growth in eccentricity deviation in all six models leads to (Figure 3.10)

$$\sigma(\Delta e) = (4.1 \pm 0.6) \times 10^{-4}\, \xi \left(\frac{H}{R}\right) \left(\frac{\Delta t}{P}\right)^{1/2}. \tag{3.17}$$

Note that at 1 AU in an MMSN disk, $\xi \simeq 1$, $H/R \simeq 0.1$, and $P = 1$ yr, and thus the increase in eccentricity deviation due to hydromagnetic turbulence only amounts to about 0.04 in 1 Myr.

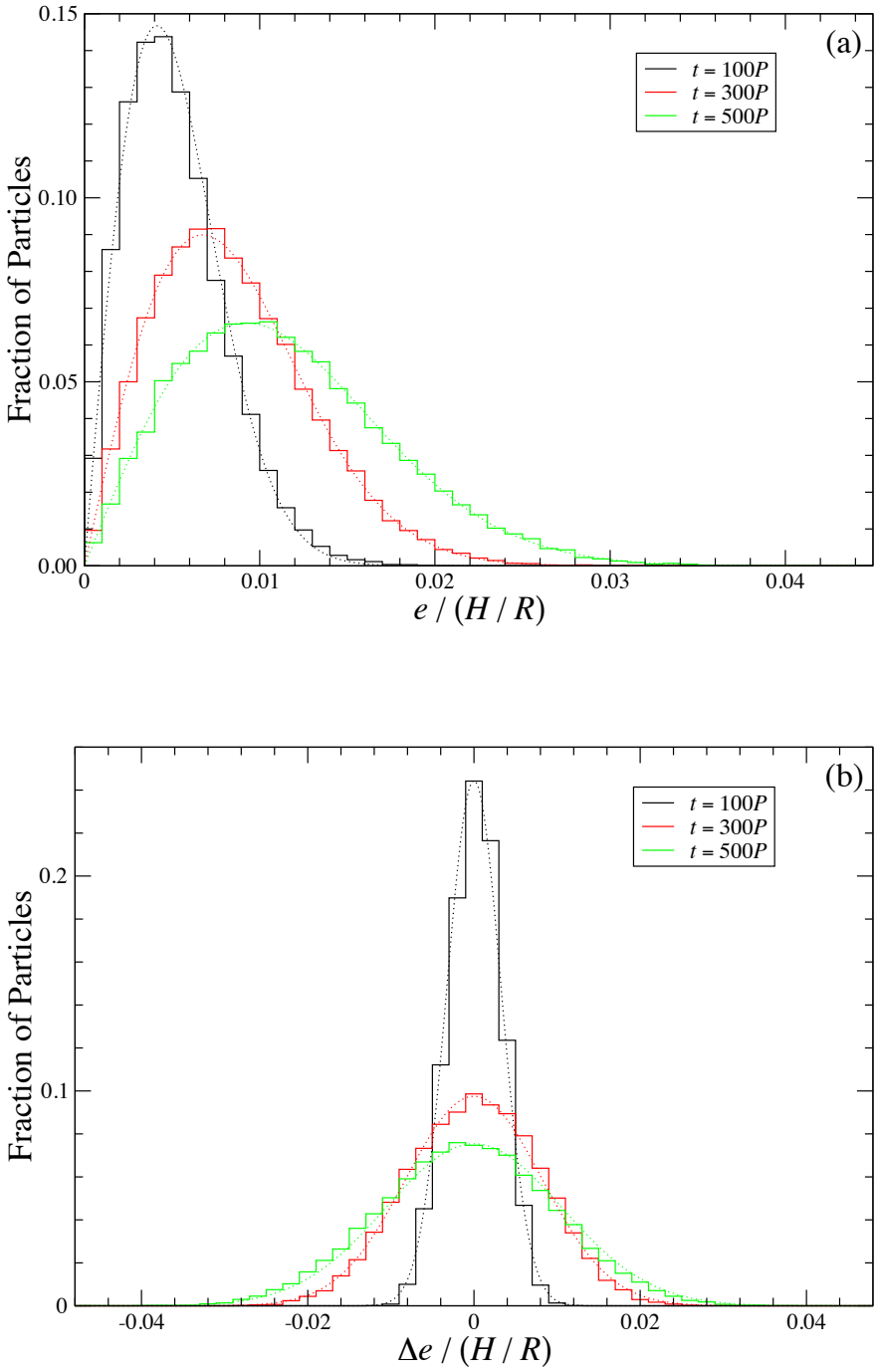

Figure 3.9 Distribution of particles in (a) eccentricity e for particles with initial eccentricity $e_0 = 0$ and (b) eccentricity deviation $\Delta e = e - e_0$ for particles with $e_0 = 0.1(H/R)$ at three different times in our fiducial model. These particles move in a low-mass disk. The dotted lines are best fits in the form of (a) Rayleigh and (b) normal distributions.

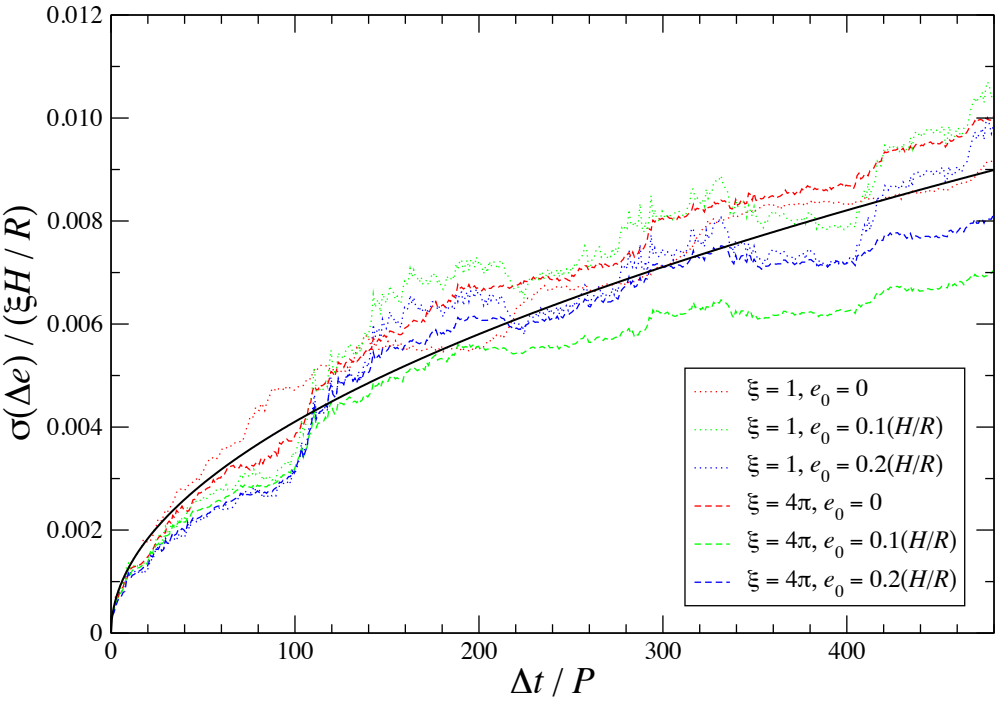

Figure 3.10 Standard deviation of eccentricity deviation $\sigma(\Delta e)$ as a function of elapsed time Δt in our fiducial model. The line styles and colors are the same as in Figure 3.7. The standard deviation measured for particles with initial eccentricity $e_0 = 0$ has been multiplied by a factor of $\sqrt{2/(4-\pi)}$ to be consistent with a normal distribution (see Section 3.2.5).

As with the case of radial drift discussed in Section 3.2.4, our measured spread of eccentricity in our fiducial model is in approximate agreement with OIM07. On the other hand, N05 reported a typical eccentricity growth of $e \simeq 0.03$ for $\Delta t \sim 100P$. With $\xi \simeq 6.6$ at radius $R = 2.7R_1$ in the model studied by N05 (R. P. Nelson 2009, private communication) and $H/R \simeq 0.1$, the eccentricity deviation given by Equation (3.17) is about one order of magnitude less than what was reported by N05.

One possible explanation for this inconsistency could be the presence of large-scale structures, particularly $m = 1$ modes, in global, but not in local models. OIM07 reported that the inclusion of an $m = 1$ mode in their torque formula induces a ten times greater impact of hydromagnetic turbulence on particle orbits, using the calibration with global MHD simulations provided by LSA04. Inspection of LSA04, as well as N05, shows that the density structures in their global models often extend more than $\pi/2$ in azimuthal angle, leading to the $m = 1$ mode having the largest amplitude. Such large-scale modes indeed can be excited in self-gravitating disks, and they could also be excited by local turbulence. This idea is offered some support by the modest growth in density perturbations in larger boxes that we find (Figure 3.2), and the growth in α reported in larger boxes by Johansen et al. (2009).

In Figure 3.11, we examine the growth in eccentricity deviation as a function of box size in our local models. Increasing the horizontal box size by a factor of four indeed increases the eccentricity deviation by a factor of four, though this still does not account for the order of magnitude higher value found by N05 in his global model. If $m = 1$ modes indeed can be similarly excited by well resolved turbulence, though, this could offer an explanation for the discrepancy.

However, using local models with mean azimuthal fields, Guan et al. (2009) reported that the coherent structures induced by the MRI are localized, with correlation lengths of about $0.05H$, $0.32H$, and $0.05H$ in radial, azimuthal, and vertical directions, respectively. Therefore, it is possible that current global models might not have enough resolution to model such fine structures, which were then spuriously connected into extended structures resembling $m = 1$ modes. To determine the physical reality of large-scale structure in turbulent disks, global models capable of resolving localized structures will be needed.

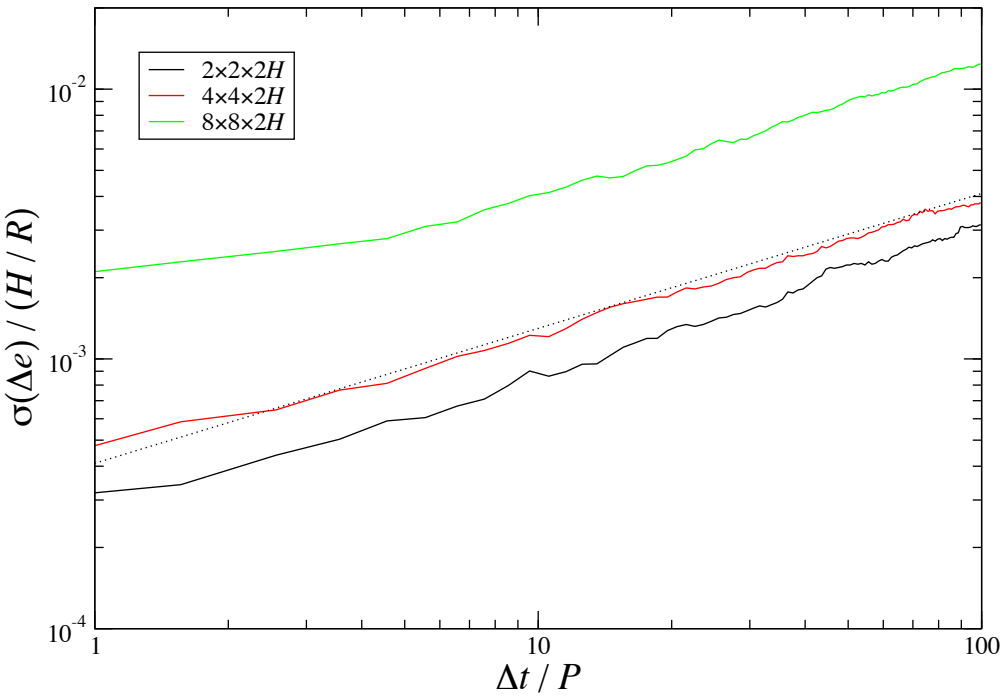

Figure 3.11 Standard deviation of eccentricity deviation $\sigma(\Delta e)$ as a function of elapsed time Δt for three different box sizes at a resolution of 32 points per scale height H (*solid* lines), where only the low-mass disk model ($\xi = 1$) and particles with zero initial eccentricity are considered. For comparison, the straight *dotted* line gives the best fit to the high-resolution model shown in Figure 3.10 (Equation (3.17)).

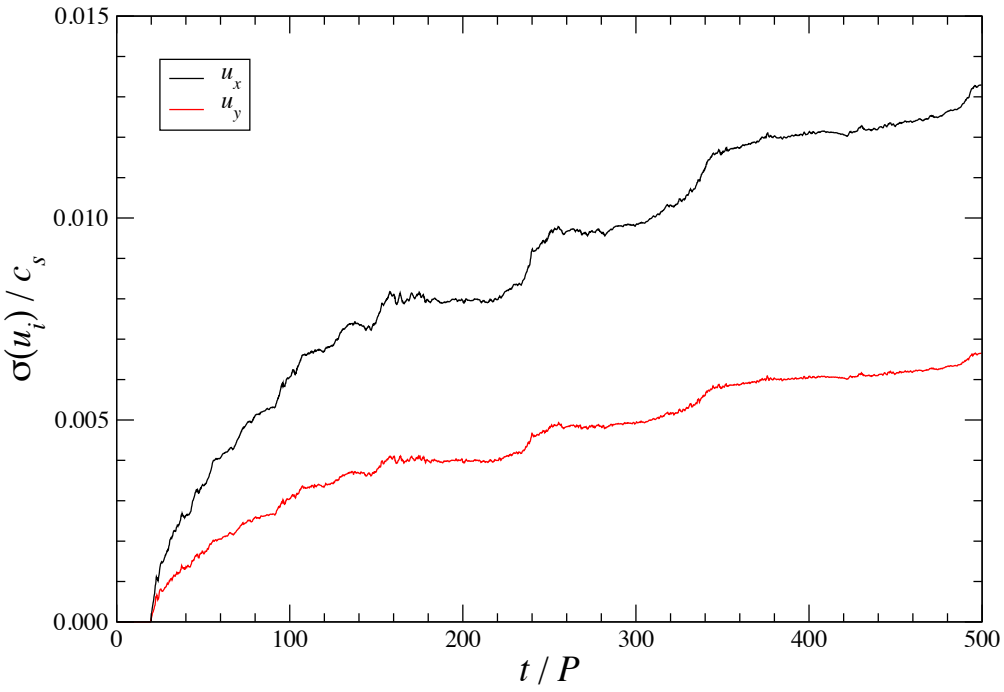

Figure 3.12 Radial and azimuthal components of velocity dispersion $\sigma(u_x)$ and $\sigma(u_y)$ as a function of time t for particles with initial eccentricity $e_0 = 0$ moving in the low-mass disk version of our fiducial model. They are presented as running averages over one orbital period P.

3.2.6 Horizontal Velocity Dispersion

Another important quantity in the study of planetesimal dynamics is the velocity dispersion of the particles. We calculate the radial and the azimuthal components of velocity dispersion by taking the standard deviations of radial and azimuthal velocities for all particles, i.e., $\sigma(u_x)$ and $\sigma(u_y)$, respectively. Since all the dynamical Equations are linearized in terms of x/R in the local shearing box approximation, the background shear flow is uniform irrespective of position, so the velocity dispersion for all particles in the computational domain is a well-defined local quantity. Figure 3.12 plots $\sigma(u_x)$ and $\sigma(u_y)$ measured for particles with zero initial eccentricity in the low-mass disk version of our fiducial model as a function of time t. The velocity dispersion monotonically increases with time, and thus hydromagnetic turbulence tends to steadily heat up a planetesimal disk. Note that $\sigma(u_y) \sim \sigma(u_x)/2$, a sanity check that our results are consistent with a swarm of non-interacting particles moving epicyclically in a Keplerian disk.

Figure 3.13 compiles the radial velocity dispersions $\sigma(u_x)$ as a function of elapsed time Δt measured in our fiducial model for particles with different initial eccentricity e_0 moving in disks of different disk gravities. As is the case with the radial drift and eccentricity deviation discussed in Section 3.2.4 and Section 3.2.5, the results depend linearly on ξ, the strength of disk gravity, though there seems to be a slightly enhanced effect for particles with $e_0 > 0$. Given the uncertainty involved in the numerical simulations, we assume it is a secondary effect as a first approximation. The best fit to all six models is then given by

$$\sigma(u_x) = (7.6 \pm 1.6) \times 10^{-4}\, \xi c_s \left(\frac{\Delta t}{P}\right)^{1/2}. \tag{3.18}$$

The corresponding timescale τ_T for turbulent excitation of velocity dispersion can be estimated by $\tau \equiv \sigma/(\mathrm{d}\sigma/\mathrm{d}\Delta t)$, and we find from Equation (3.18)

$$\tau_T = \left(3.4 \times 10^6\, P\right) \xi^{-2} \left[\frac{\sigma(u_x)}{c_s}\right]^2. \tag{3.19}$$

Increasing the box size increases the magnitude of this effect, as shown in Figure 3.14, possibly even non-linearly.

As noted in Section 3.2.5, hydromagnetic turbulence can act either to excite the eccentricities of planetesimals or to circularize their eccentric orbits. However, a perfectly cold disk of planetesimals with nonzero initial eccentricity but vanishing velocity dispersion will be monotonically heated by the turbulence, as shown above. The velocity dispersion increases with time while the mean eccentricity may remain unchanged unless a significant fraction of particles are circularized. Therefore, the eccentricity may not necessarily be proportional to the velocity dispersion for a swarm of planetesimals moving through hydromagnetic turbulence.

The velocity dispersion of a planetesimal disk also grows with time due to mutual gravitational scattering. The corresponding timescale for a swarm of identical particles of mass m_p can be estimated by (e.g., Papaloizou & Terquem, 2006)

$$\tau_{GS} = \frac{\sigma^3(u_x)}{8\sqrt{\pi} G^2 m_p^2 n_p \ln \Lambda_p} \left[\frac{\sqrt{3}}{4} \ln\left(\frac{2+\sqrt{3}}{2-\sqrt{3}}\right) - 1\right]^{-1}, \tag{3.20}$$

where n_p is the number density of planetesimals and $\Lambda_p = 3\sigma^2(u_x) H_p / 4 G m_p$, in which $H_p \sim \sqrt{2}\sigma(u_z)/\Omega_K$ is the scale height of the planetesimal disk determined by the vertical

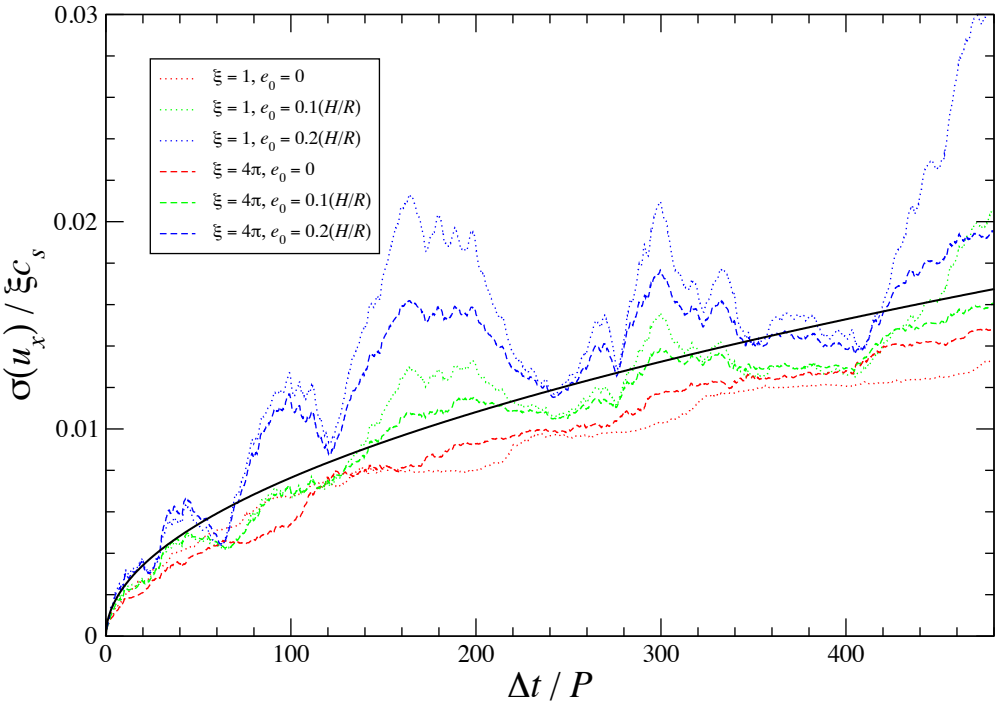

Figure 3.13 Radial component of velocity dispersion $\sigma(u_x)$ as a function of elapsed time Δt in our fiducial model, computed as running averages over one orbital period P. The *dotted* lines are obtained from low-mass disks ($\xi = 1$) while the *dashed* lines are from high-mass disks ($\xi = 4\pi$). Particles with initial eccentricities $e_0 = 0$, $0.1(H/R)$, and $0.2(H/R)$ are denoted by *red*, *green*, and *blue* lines, respectively. The *solid black* line is the best fit to all six curves, assuming no explicit dependence on e_0.

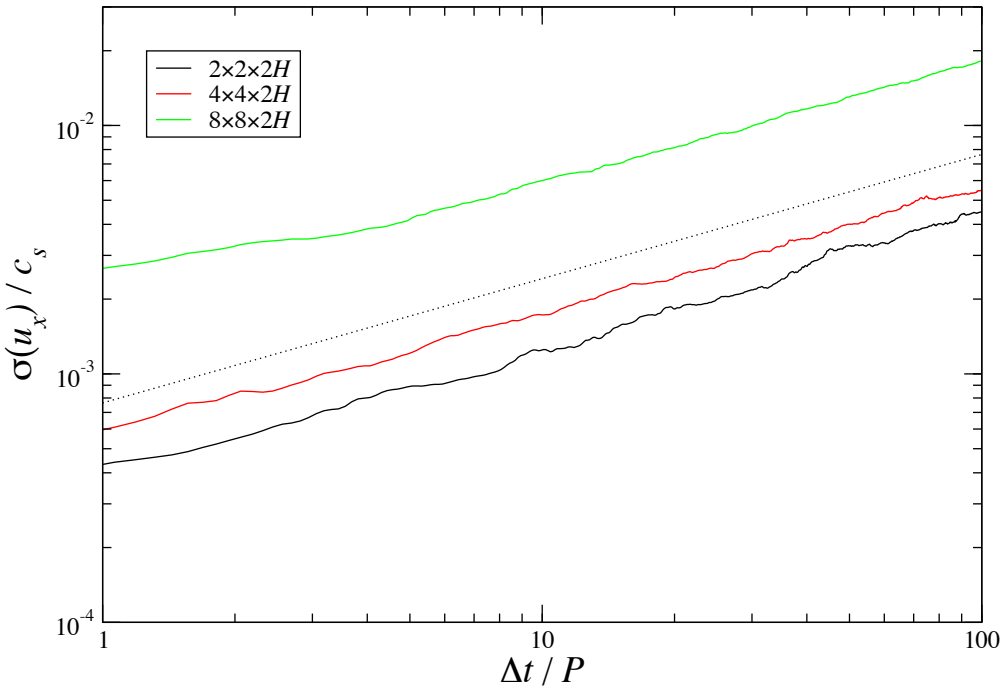

Figure 3.14 Radial component of velocity dispersion $\sigma(u_x)$ as a function of elapsed time Δt for three different box sizes at a resolution of 32 points per scale height H (*solid* lines), where only the low-mass disk model ($\xi = 1$) and particles with zero initial eccentricity are considered. For comparison, the straight *dotted* line gives the best fit to the high-resolution model shown in Figure 3.13 (Equation (3.18)).

velocity dispersion $\sigma(u_z)$. To find τ_{GS} in physical units, we assume for simplicity that most of the solid material in a protoplanetary disk is concentrated in planetesimals, and thus $n_p m_p \sim \varepsilon \rho_0 c_s / \sigma(u_z)$ where ε is the solid-to-gas ratio. We also assume $\sigma(u_z) \sim \sigma(u_x)/2$, so that Equation (3.20) becomes

$$\tau_{GS} \simeq \frac{\sqrt{\pi} P^2 \sigma^4(u_x)}{4\varepsilon\xi c_s G m_p \ln \Lambda_p} \left[\frac{\sqrt{3}}{4} \ln\left(\frac{2+\sqrt{3}}{2-\sqrt{3}} \right) - 1 \right]^{-1} \tag{3.21}$$

with

$$\Lambda_p \simeq \frac{3\sqrt{2} P \sigma^3(u_x)}{16\pi G m_p}. \tag{3.22}$$

We further focus our discussion on a velocity scale of order $v_{\rm esc}$, the escape velocity at the surface of a planetesimal:

$$v_{\rm esc} = \left(\frac{32\pi}{3} G^3 m_p^2 \rho_p \right)^{1/6}, \tag{3.23}$$

where ρ_p is the material density of the planetesimal. This scale is of critical interest for planetary cores to accrete solid material; particles with relative velocities of order $v_{\rm esc}$ are more likely to coalesce into larger bodies than to be eroded into smaller pieces. By assuming $\sigma(u_x) \sim v_{\rm esc}$, the timescales for heating a planetesimal disk by hydromagnetic turbulence and gravitational scattering become

$$\tau_T = \left(1.1 \times 10^2 \text{ yr}\right) \xi^{-2} \left(\frac{\rho_p}{3 \text{ g cm}^{-3}} \right)^{1/3} \left(\frac{m_p}{10^{18} \text{ g}} \right)^{2/3} \left(\frac{c_s}{10^5 \text{ cm s}^{-1}} \right)^{-2} \left(\frac{P}{\text{yr}} \right) \tag{3.24}$$

and

$$\tau_{GS} \simeq \left(\frac{1.4 \times 10^5}{\ln \Lambda_p} \text{ yr} \right) \xi^{-1} \left(\frac{\varepsilon}{0.01} \right)^{-1} \left(\frac{\rho_p}{3 \text{ g cm}^{-3}} \right)^{2/3} \left(\frac{m_p}{10^{18} \text{ g}} \right)^{1/3} \left(\frac{c_s}{10^5 \text{ cm s}^{-1}} \right)^{-1} \left(\frac{P}{\text{yr}} \right)^2 \tag{3.25}$$

with

$$\Lambda_p \simeq 6.9 \times 10^3 \left(\frac{\rho_p}{3 \text{ g cm}^{-3}} \right)^{1/2} \left(\frac{P}{\text{yr}} \right), \tag{3.26}$$

respectively.

With the scales assumed above and at 1 AU in an MMSN disk, $\tau_{GS} \sim 2 \times 10^4$ yr while measurement from our high-resolution fiducial model described by Equation (3.19) gives $\tau_T \sim 100$ yr. For larger objects approaching the planetary mass regime, with $m_p = 0.001 M_\oplus$, $\tau_{GS} \sim \tau_T \sim 3 \times 10^6$ yr. Therefore, hydromagnetic turbulence probably dominates the

heating of a disk of kilometer-sized planetesimals, while gravitational scattering may be more important for objects approaching the Earth size. Models with larger boxes yield smaller values of τ_T, strengthening this conclusion. Note that τ_{GS} increases more steeply with $\sigma(u_x)$ and P but decreases less rapidly with ξ than τ_T (Equations (3.19) and 3.21), and thus hydromagnetic turbulence gains dominance over gravitational scattering for larger velocity dispersion, larger distance to the host star, and more massive gas disks than assumed here.

3.3 Implications For Planet Formation

In this section, we apply our results on the orbital evolution of zero-mass particles to two specific problems in planet formation. First, we estimate the strength of diffusive migration of protoplanets due to hydromagnetic turbulence and discuss their survivability under type I migration following the analytical framework established by JGM06. Secondly, we revisit the proposition of IGM08 that planetesimals may suffer from collisional destruction as a result of hydromagnetic turbulence excitation of velocity dispersion among them.

3.3.1 Diffusive Migration of Protoplanets

Using a Fokker-Planck formalism, JGM06 derived an advection-diffusion Equation to describe the evolution of the distribution of protoplanets under the influence of both type I migration and hydromagnetic turbulence. Adams & Bloch (2009) further consolidated the analysis by studying more realistic disk density structure with both spatial and time dependence. These authors found that turbulence tends to reduce the lifetimes of most protoplanets while allowing some of them to linger long enough to survive rapid inward type I migration. The likelihood of producing a planetary system with a specific configuration sensitively depends on the strength of the diffusive migration induced by the turbulence, however. JGM06 and Adams & Bloch (2009) calibrated the turbulence strength with the global disk models computed by LSA04, Nelson & Papaloizou (2004), and N05. In contrast, using a local disk model, OMM07 found that the strength might be several orders of magnitude less than what was estimated by JGM06. In this section, we provide a new assessment based on the disk models studied in this work.

As shown in Section 3.2.4, an initial delta function in the distribution of mean orbital radii of zero-mass particles is spread with time into a normal distribution of constant mean. A $t^{1/2}$ time dependence for the standard deviation of the distribution suggests that this process can be described by a diffusion Equation of the form

$$\frac{\partial f}{\partial t} = \frac{\partial}{\partial x}\left(\mathcal{D}\frac{\partial f}{\partial x}\right), \tag{3.27}$$

where $\mathcal{D}$ is the diffusion coefficient and $f = f(t, x)$ is the distribution function: $f(t, x)\mathrm{d}x$ is the probability of finding a particle with a radial displacement in $(x, x + \mathrm{d}x)$ at time t. Let us write,

$$f(x, t) = \frac{1}{\sigma(t)\sqrt{2\pi}} \exp\left[-\frac{x^2}{\sigma^2(t)}\right], \tag{3.28}$$

$$\sigma(t) = \sigma_1 \left(\frac{t}{P}\right)^{1/2} \qquad (t > 0), \tag{3.29}$$

where σ_1 is a proportionality constant. Substituting Equation (3.28) into Equation (3.27), we find that $\mathrm{d}\sigma/\mathrm{d}t = 2\mathcal{D}/\sigma$ and thus with $\sigma(t \to 0^+) = 0$,

$$\sigma(t) = 2\mathcal{D}^{1/2} t^{1/2}. \tag{3.30}$$

By comparing Equations (3.29) and (3.30), the diffusion coefficient $\mathcal{D}$ is related to σ_1 and P by

$$\mathcal{D} = \frac{\sigma_1^2}{4P}. \tag{3.31}$$

The best fit to our fiducial high-resolution, small box model, given by Equation (3.15), can be substituted here to find

$$\mathcal{D}(R) = 3.6 \times 10^{-8}\, \xi^2 \left(\frac{H^2}{P}\right) \tag{3.32}$$

by identifying t with Δt. In this derivation, we have assumed that the stochastic torque exerted by hydromagnetic turbulence is a local process such that the diffusion coefficient $\mathcal{D}$ is sufficiently constant near $x = 0$.

We are now in a position to estimate the diffusion coefficient $D(J)$ of JGM06 in comparison to $\mathcal{D}(R)$, where $J = m_p\,(GM_\star R)^{1/2}$ is the orbital angular momentum of a protoplanet of mass m_p orbiting a star of mass $M_\star$ on a quasi-circular orbit at a radial distance R. Since $D(J)$ and $\mathcal{D}(R)$ have dimensions of $[J^2/t]$ and $[R^2/t]$, respectively, they may be related by

$D(J) \sim \mathcal{D}(R)(\partial J/\partial R)^2 = (J/2R)^2\mathcal{D}(R)$. Using dimensional arguments, JGM06 defined a dimensionless parameter ϵ to describe the uncertainties associated with hydromagnetic turbulence:

$$D(J) = (2.1 \times 10^{-3})\epsilon(2\pi)^3 \frac{\Sigma^2 J^7}{G^2 M_\star^4 m_p^5} = \frac{(2.1 \times 10^{-3})}{16\pi}\epsilon\xi^2 \left(\frac{H}{R}\right)^2 \left(\frac{J^2}{P}\right). \tag{3.33}$$

By comparing Equations (3.32) and (3.33), we find that

$$\epsilon \simeq 2.2 \times 10^{-4} \tag{3.34}$$

for our fiducial model. Note that ϵ is a constant independent of R given our scalings, in agreement with the assumption of constant ϵ made by JGM06.

The value of ϵ estimated in Equation (3.34) is about an order of magnitude smaller than what was reported by OMM07 for a stratified disk model with zero net flux on a $1 \times 4 \times 4H$ grid at the same resolution as our fiducial model with 64 points per scale height. To identify the reason for this discrepancy, we further evaluate the magnitude and the correlation time of the torques exerted by the turbulent gas on the particles in our model. First, the rms of the y-component of the gravitational force per unit mass exerted by the gas over all time and particles is $a_{y,\mathrm{rms}} \simeq (3.7 \times 10^{-3})\xi H P^{-2} = (4.2 \times 10^{-3})(2\pi G\Sigma)$. We find negligible difference between torques calculated following the particles along their orbits and those calculated at the fixed center of the box. The magnitude we obtained is reasonably consistent with the value of $a_{y,\mathrm{rms}} = (3.2 \times 10^{-3})(2\pi G\Sigma)$ reported by OMM07 at the same numerical resolution. Secondly, we plot in Figure 3.15 the autocorrelation functions (ACFs) of a_y for several randomly selected particles as well as at the center of the box. The results are again similar to what was reported by OMM07, indicating a similar estimate for the correlation time, τ_c. The source of the discrepancy appears to be neither of these factors.

We notice, though, that OMM07 could have overestimated the correlation time by equating it to the value of the second zero crossing of the ACF. Strictly speaking, the correlation time should instead be computed by integrating an ensemble average of the ACF over all possible realizations, as motivated by the definitions of the diffusion coefficient and the correlation time in JGM06:

$$D(J) \equiv \frac{1}{2}\int_{-\infty}^{\infty} \overline{\delta\Gamma(t - \frac{\tau}{2}, J)\delta\Gamma(t + \frac{\tau}{2}, J)}\, \mathrm{d}\tau \tag{3.35}$$

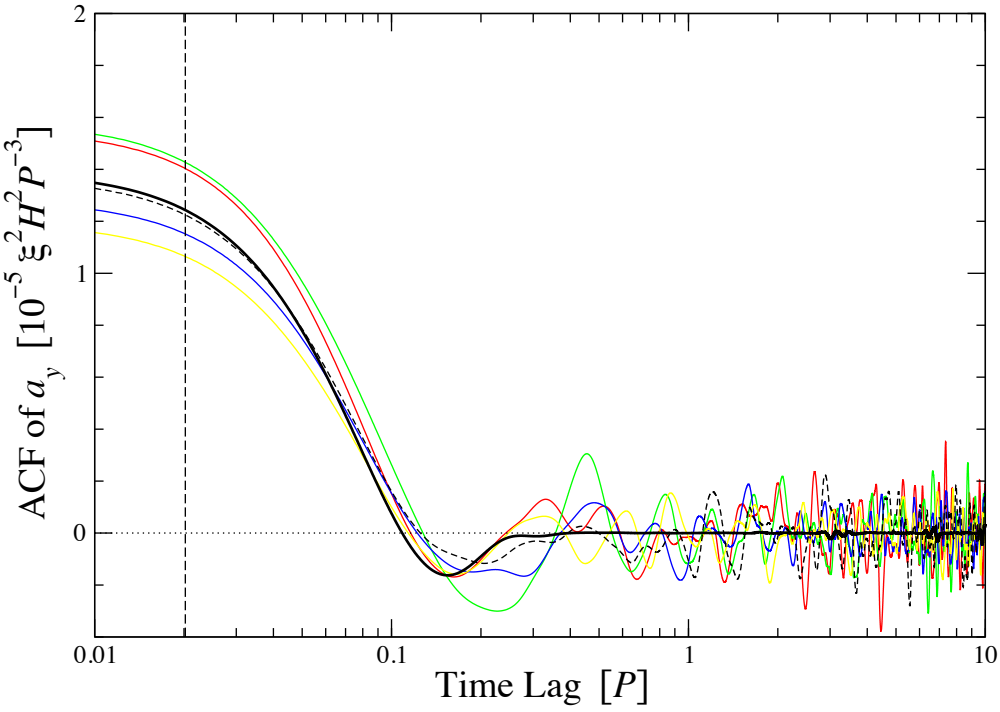

Figure 3.15 Autocorrelation functions of the azimuthal (torque) component of the gravitational force per unit mass, a_y, exerted by the turbulent gas in our fiducial model. The *short-dashed black* curve corresponds to a_y calculated at the center of the box, while the various *colored* curves correspond to a_y calculated following the orbits of several randomly selected particles. The average over all particles is given by the *solid black* line, which shows almost no power beyond the second zero-crossing. The vertical *long-dashed black* line indicates our estimated correlation time of the torques using Equation (3.37). Notice the negative part of the ensemble-averaged ACF beyond the first zero-crossing, which may be responsible for reducing the diffusion coefficient (see Section 3.3.1).

and

$$\tau_c \equiv D(J)/\overline{\delta\Gamma^2(t,J)}, \tag{3.36}$$

where $\delta\Gamma(t,J)$ is the fluctuating part of the torque and the overline denotes ensemble average. Since we distribute numerous particles uniformly over the entire computational domain, the ACF obtained for each particle can be considered as one realization, and the average of the ACFs over all particles may resemble the true ensemble average. This averaged ACF is shown by the solid black curve in Figure 3.15. Note that the oscillation occurring at time lag longer than the second crossing for each particle is much reduced, indicating the noise nature of the autocorrelation at long time lag. However, the negative value of the ACF between the first two zero-crossings remains significant. This interval represents the anti-diffusion nature of the stochastic torques that we believe could be responsible for reducing the diffusion coefficient. Therefore, we suggest that a better approximation for the correlation time in accordance with Equations (3.35) and (3.36) be

$$\tau_c \approx \frac{\int_0^\infty \overline{\mathrm{ACF}(\tau)}\,\mathrm{d}\tau}{2\overline{\mathrm{ACF}(0)}}, \tag{3.37}$$

where $\overline{\mathrm{ACF}(\tau)}$ is the ensemble-averaged ACF of the torque per unit mass a_y as a function of time lag τ. Using Equation (3.37), we find that in our fiducial model $\tau_c \simeq 0.020P$, about one order of magnitude less than the value of $\tau_c \simeq 0.31P$ reported by OMM07. With the same approximation $D(J) \simeq m_p^2 R^2 \overline{a_y^2}\tau_c$ used by OMM07, we find that $\epsilon \simeq 1.7 \times 10^{-4}$, in good agreement with the estimate of $\epsilon \simeq 2.2 \times 10^{-4}$ we derived from our direct measurement of particle radial drifts.

Therefore, we have achieved consistent results using two independent approaches to estimating the diffusion coefficient, one by direct measurement as in Equation (3.32) and the other by the definition of correlation time given by JGM06 (Equation (3.36)). In principle, our direct measurement should be robust while using $D(J) \simeq \tau_c \overline{\delta\Gamma^2}$ can only be considered as an approximation. To use the latter approach, one should refer to Equation (3.37) to measure the correlation time of the stochastic torques, instead of conventional methods like using the zero crossing of the ACF or the timescale of the peak of the temporal power spectrum, which probably give about one order of magnitude larger values. It will be enlightening for studies based on global models to conduct the same exercise described in this section, since

this will likely explain part of the orders of magnitude discrepancy in diffusion coefficients derived from local versus global models. (Although the box size effects we have identified must also contribute to this discrepancy, they appear unable to increase the derived value of ϵ by more than one order of magnitude.)

According to Figures 6 and 7 of JGM06, the value of ϵ we inferred from our simulations indicates that advective (type I) migration dominates over diffusive (stochastic) migration for the parameter space JGM06 have investigated. For an Earth-mass protoplanet at a radial distance up to 100 AU in the MMSN disk and in a viscous disk with $\alpha = 0.02$, advection dominates when $\epsilon \lesssim 10^{-2}$ and 10^{-1}, respectively. For a protoplanet of mass as low as 0.01 $M_\oplus$ at $R = 10$ AU in the same disk models, advection dominates when $\epsilon \lesssim 10^{-3}$ and 10^{-2}, respectively. The critical distance and mass for the transition between dominance of advection and diffusion given our small estimate of ϵ for our fiducial model is outside of the parameter space explored by JGM06, and even our largest box has a value of ϵ less than an order of magnitude larger. By inspection of Figure 7 in JGM06, though, the transition masses for an object at 10 AU in the MMSN disk and in the viscous disk probably lies at about 10^{-3} and 10^{-4} $M_\oplus$, respectively. Therefore, our results suggest that hydromagnetic turbulence does not significantly affect the secular migration of Earth-sized protoplanets in regimes of current astrophysical interest. Nevertheless, torques exerted by turbulent density perturbations seem to be a dominant agent determining the orbital dynamics of kilometer-sized planetesimals.

3.3.2 Collisional Destruction of Planetesimals

IGM08 suggested that hydromagnetic turbulence may inhibit the growth of kilometer-sized planetesimals. They argued that the velocity dispersion excited by the turbulence could be so large that collisions between planetesimals exceed their material strength or self-gravity, leading to destruction. Their conclusion, however, relies on orbital integrations incorporating the heuristic, stochastic formulae for the time history of gravitational torques provided by LSA04, which in turn were calibrated using MHD simulations of a global disk model. As pointed out in Section 3.2.5, a possible inconsistency exists between global and local models. Since the latter shows a significantly lower effect on orbital dynamics of planetesimals, it is

worthwhile revisiting the planetesimal growth problem in light of the results highlighted in this work.

For comparison purposes, we adopt the same scalable MMSN disk model as used by IGM08. The gas density and the speed of sound in the mid-plane are given by

$$\rho_0 = \left(1.8 \times 10^{-9}\ \mathrm{g\ cm^{-3}}\right) f_g \left(\frac{R}{\mathrm{AU}}\right)^{-11/4} \tag{3.38}$$

and

$$c_s = \left(1.1 \times 10^{5}\ \mathrm{cm\ s^{-1}}\right) \left(\frac{R}{\mathrm{AU}}\right)^{-1/4}, \tag{3.39}$$

respectively, where a solar-type host star ($M_\star = M_\odot$) is assumed and f_g is a scale factor. When $f_g = 1$, the disk mass is about 1.4 times that of an MMSN disk. The corresponding ξ-parameter and ratio of disk scale height to radial distance then become

$$\xi = 1.5 f_g \left(\frac{R}{\mathrm{AU}}\right)^{1/4} \tag{3.40}$$

and

$$\frac{H}{R} = 0.051 \left(\frac{R}{\mathrm{AU}}\right)^{1/4}, \tag{3.41}$$

respectively. Substituting Equations (3.40) and (3.41) into Equation (3.17), which is derived from our fiducial high-resolution model, we arrive at

$$\sigma(\Delta e) = 3.1 \times 10^{-5}\, f_g \left(\frac{R}{\mathrm{AU}}\right)^{-1/4} \left(\frac{\Delta t}{\mathrm{yr}}\right)^{1/2}. \tag{3.42}$$

Comparing Equation (3.42) with Equation (13) of IGM08 with the understanding that $\sigma(e) = \sigma(\Delta e)\sqrt{(4-\pi)/2}$ for particles with zero initial eccentricity (see Section 3.2.5), we find the value of the dimensionless parameter γ—a measure of the strength of hydromagnetic turbulence used by IGM08—in our orbital integrations to be $\gamma \simeq 2.0 \times 10^{-4}$. The rest of the analysis performed by IGM08 remains unchanged since the effects induced by hydromagnetic turbulence are all incorporated in the parameter γ.

As noted in Section 3.2.5, enlarging the horizontal size of our shearing box by a factor of four at our medium resolution increases the amplitude of the eccentricity deviation by about a factor of four. Nevertheless, the largest box we have studied gives $\gamma \simeq 6 \times 10^{-4}$, which remains somewhat smaller than the $\gamma \sim 10^{-3}$–10^{-2} estimated by IGM08.

The rather small values of γ we obtained indicate that hydromagnetic turbulence might not pose as a serious threat to the growth of kilometer-sized planetesimals as suggested by IGM08. These authors compared the critical radii of planetesimals for accretive and erosive regimes due to different turbulence strengths $\gamma = 10^{-2}, 10^{-3}$, and 10^{-4} in their Figures 3, 4, and 5, respectively. Therefore, the values of γ we measured point to a scenario in between what is predicted by Figures 4 and 5 of IGM08. In this scenario, the erosive regime only appears in the outer regions of a young protoplanetary disk and it disappears rapidly with decreasing disk mass. Kilometer-sized planetesimals may be able to evade collisional destruction in the inner regions of the disk.

We reiterate that the value of γ measured here pertains to a local region with turbulent stresses such that $\alpha \sim 10^{-2}$ and $\Delta\rho/\rho_0 \sim 10\%$. As discussed in Section 3.2.5, the validity of our results in a global context remains to be demonstrated by numerical experiments on a global disk model with a resolution capable of resolving the characteristic scales of coherent turbulence structures.

3.4 Conclusions

In this work, we have used local, shearing-box simulations to study the dynamics of massless planetesimals in a turbulent, isothermal, unstratified, gas disk driven by the MRI. With a uniform, vertical magnetic field but without explicit physical dissipation, the saturated turbulence is maintained at a roughly constant level, showing convergence with increasing resolution. By adopting a suitable magnitude for the net magnetic flux, we produce a fiducial disk model with turbulent accretion at the level of $\alpha \sim 10^{-2}$ and with rms density perturbations $\Delta\rho/\rho_0 \sim 10\%$. As discussed in Section 3.1.3, this model can be scaled to other physical systems of interest, as long as the assumption of negligible self-gravity of the gas remains valid. After the hydromagnetic turbulence in our fiducial model reaches saturation, we distribute numerous particles of zero mass and integrate their orbital motion under the gravitational influence of the turbulent gas.

The stochastic nature of the orbital evolution of these particles is evident, so we characterize their orbital dynamics with statistical distributions, finding three major results. First, although the mean orbital radius does not change, particles slowly drift away from their

original radii, so that the distribution of radii grows with time. Second, gravitational force from density perturbations produced in hydromagnetic turbulence can both excite and damp the eccentricities of particle orbits, with again no change in the mean value, but a growing width of distribution if the particles possess non-negligible initial eccentricities. Finally, the planetesimal disk is heated up by the turbulence, a process dominating over gravitational scattering between particles in most physical conditions relevant to protoplanetary gas disks and planetesimal sizes. A corollary of these results is that eccentricity does not serve as a good indicator of the velocity dispersion of the particles.

The amplitude of orbital changes driven by the turbulence in our local models is significantly smaller than what was reported in recent global models (LSA04; N05; IGM08). Two possible explanations for this discrepancy suggest themselves: either insufficient resolution in the global models or the lack of convergence with box size in our local shearing box model, as discussed in Section 3.2.5. If our local results are valid, they indicate that although hydromagnetic turbulence can drive radial diffusion, eccentricity variations, and relative velocities of planetesimals and protoplanets, these effects may not be dominant in determining their evolution. In particular, it appears that type I migration dominates over turbulent radial drift for objects well above 10^{-4} $M_{\oplus}$. In addition, hydromagnetic turbulence might not be exciting sufficient velocity dispersion to drive planetesimals into an erosive regime that would inhibit their further growth. Before these results can be considered robust, however, it will be necessary to elucidate, and hopefully reconcile, the differences that have appeared between global and local models.

Chapter 4

Planetesimal and Protoplanet Dynamics in a Turbulent Protoplanetary Disk: Ideal Stratified Disks

4.1 Numerical Modelling

Directly extending the work we reported in Chapter 3, we continue to use the Pencil Code[1] to model particles moving in magneto-rotational turbulence. We describe in detail the equations and the relevant numerical techniques we implemented in the code.

4.1.1 Magnetohydrodynamics

We use the local shearing box approximation (e.g., Goldreich & Lynden-Bell, 1965; Brandenburg et al., 1995; Hawley et al., 1995). A local shearing box is a small Cartesian box at a large distance R to the host star about which the center of the box revolves at its Keplerian angular speed Ω_K. The box is always oriented with the x-axis directing radially and the y-axis azimuthally. In contrast to Chapter 3, we include the linearized vertical gravity from the host star so that the disk is vertically stratified. We again impose a vertical, external magnetic field $\boldsymbol{B}_{\rm ext} = B_{\rm ext}\hat{\boldsymbol{z}}$ to maintain a non-zero magnetic flux. The magnetohydrodynamical

[1]The Pencil Code is publicly available at `http://code.google.com/p/pencil-code/`.

equations then become

$$\partial_t \rho - \frac{3}{2}\Omega_K x \partial_y \rho + \nabla \cdot (\rho \boldsymbol{u}) = f_D, \tag{4.1}$$

$$\partial_t \boldsymbol{u} - \frac{3}{2}\Omega_K x \partial_y \boldsymbol{u} + \boldsymbol{u} \cdot \nabla \boldsymbol{u} = -\frac{1}{\rho}\nabla p + \left(2\Omega_K u_y \hat{\boldsymbol{x}} - \frac{1}{2}\Omega_K u_x \hat{\boldsymbol{y}} - \Omega_K^2 z \hat{\boldsymbol{z}}\right) + \frac{1}{\rho}\boldsymbol{J} \times (\boldsymbol{B} + \boldsymbol{B}_{\rm ext}) + \boldsymbol{f}_V, \tag{4.2}$$

$$\partial_t \boldsymbol{A} - \frac{3}{2}\Omega_K x \partial_y \boldsymbol{A} = \frac{3}{2}\Omega_K A_y \hat{\boldsymbol{x}} + \boldsymbol{u} \times (\boldsymbol{B} + \boldsymbol{B}_{\rm ext}) + \boldsymbol{f}_R, \tag{4.3}$$

in which ρ is gas density, $\boldsymbol{u}$ is gas velocity relative to the background shear flow, p is gas pressure, $\boldsymbol{J} = \nabla \times \boldsymbol{B}/\mu_0$ is the electric current density, $\boldsymbol{B} = \nabla \times \boldsymbol{A}$, and μ_0 is permeability. The terms f_D, $\boldsymbol{f}_V$, and $\boldsymbol{f}_R$ are numerical dissipation terms, including both hyper-diffusions and shock diffusions, that are needed to stabilize the scheme, and the reader is referred to Chapter 3 for their description. We assume an isothermal equation of state, $p = c_s^2 \rho$, where c_s is the isothermal speed of sound.

We set up the gas density so that the gas is at vertical hydrostatic equilibrium initially:

$$\rho_0(z) = \rho_m \exp\left(-\frac{z^2}{H^2}\right), \tag{4.4}$$

in which ρ_m is the mid-plane gas density and $H = \sqrt{2} c_s/\Omega_K$ is the vertical disk scale height. The initial magnetic vector potential $\boldsymbol{A}$ is set to zero, while the external magnetic field is fixed at such a level that the corresponding plasma $\beta_{\rm ext}(z) \equiv 2\mu_0 c_s^2 \rho_0 / B_{\rm ext}^2$ in the mid-plane is $\beta_{\rm ext}(0) = 6.2 \times 10^3$. Gaussian noise of magnitude $10^{-3}\, H/P$ in each component of the gas velocity $\boldsymbol{u}$ is generated to seed the MRI, where $P = 2\pi/\Omega_K$ is the orbital period at the center of the shearing box.

We adopt different boundary conditions for the gas and the magnetic field. Horizontally, we use sheared periodic boundary conditions for all dynamical variables, i.e., the system is periodic after shifted by the background shear flow (Hawley et al. 1995; also see Section 4.1.2). On the other hand, the gas density and velocity is periodic in z-direction while the magnetic field is held vertically across the z-boundaries. Vertical periodicity in gas attributes is used to conserve the total mass and to mimic both inward and outward flows of the turbulent fluctuations across the boundary. The vertical-field boundary condition is achieved by setting $\partial_z A_x = \partial_z A_y = A_z = 0$. This condition forces the radial and the toroidal components of the

magnetic field to be zero ($B_x = B_y = 0$) at the z-boundary planes while allowing the vertical component (B_z) to be free.

For large box simulations, concerns have been raised that artificial numerical diffusion as a function of x may occur due to the radial dependence of shear velocity and thus the corresponding truncation errors on a fixed grid (Johnson et al., 2008). Explicit treatment of the shear advection may be needed to eliminate these truncation errors. In the Pencil Code, this kind of technique, dubbed the shear advection by Fourier interpolation (SAFI), has been implemented (Johansen et al., 2009). In this work, we also implement the SAFI for all of our simulations to remove the undesirable numerical effect.

4.1.2 Poisson Equation with Isolated Boundary Condition in z-direction

To find the gravitational influence of the turbulent gas on the movement of solid particles, we need to solve the Poisson equation for the fluctuation potential Φ_1 in the local shearing box (Goldreich & Lynden-Bell, 1965)

$$\left[\left(\partial_x + \frac{3}{2}\Omega_K t\partial_y\right)^2 + \partial_y^2 + \partial_z^2\right]\Phi_1 = 4\pi G\rho_1, \tag{4.5}$$

where G is the gravitational constant and $\rho_1 = \rho - \rho_0$ is the density fluctuation with respect to the basic state of the gas stratification. The boundary conditions appropriate to our stratified gas disk are sheared periodic horizontally while isolated or open vertically, i.e., we assume that there exist no fluctuations in density outside the vertical boundary. Since the equilibrium density (Equation (4.4)) declines exponentially above and below the mid-plane, the fluctuations may well be ignored at high altitude.

We use a variation of Hockney & Eastwood (1988) fast algorithm to solve the Poisson equation (4.5), combining the Fourier interpolation technique to achieve sheared periodicity (Brucker et al., 2007; Johansen et al., 2007). The computational domain is doubled in z-direction by appending $\rho_1 = 0$. The expanded $\rho_1(x, y, z)$ is Fourier transformed in the y-direction into $\hat{\rho}_1(x, k_y, z)$, where k_y is the y-wavenumber. The result is phase shifted to recover periodicity in x-direction: $\check{\rho}_1(x, k_y, z) = \hat{\rho}_1(x, k_y, z)\exp\left[-i(3/2)\Omega_K k_y x\delta t\right]$, where δt is the time step. Then $\check{\rho}_1(x, k_y, z)$ is Fourier transformed in x-direction into $\widetilde{\rho}_1(k_x, k_y, z)$,

where k_x is the x-wavenumber.

For the modes $k_x^2 + k_y^2 > 0$, $\widetilde{\rho}_1(k_x, k_y, z)$ is Fourier transformed in z-direction to find $\breve{\rho}_1(k_x, k_y, k_z)$, where k_z is the z-wavenumber. The fluctuation potential in Fourier space $\breve{\Phi}_1(k_x, k_y, k_z)$ is calculated using the usual convolution theorem:

$$\breve{\Phi}_1(k_x, k_y, k_z) = -\frac{4\pi G}{\left(k_x + 3\Omega_K k_y \delta t/2\right)^2 + k_y^2 + k_z^2} \breve{\rho}_1(k_x, k_y, k_z), \quad \text{for } k_x^2 + k_y^2 > 0. \tag{4.6}$$

It is then inverse Fourier transformed in k_z to find $\widetilde{\Phi}_1(k_x, k_y, z)$.

The mode $k_x = k_y = 0$ needs to be treated seperately. It represents an infinite thin layer of mass of constant density at a given altitude z. The corresponding gravitational acceleration is constant above and below z. Therefore, the resultant fluctuation potential can be written as

$$\widetilde{\Phi}_1(k_x = 0, k_y = 0, z) = 2\pi G \int \widetilde{\rho}_1(k_x = 0, k_y = 0, z')|z - z'|dz', \tag{4.7}$$

where we have arbitrarily defined the reference potential to be zero at each altitude. Instead of calculating the convolution by Fourier transforms, we directly evaluate the discretized version of equation (4.7):

$$\widetilde{\Phi}_1(k_x = 0, k_y = 0, z_j) = 2\pi G \sum_k \widetilde{\rho}_1(k_x = 0, k_y = 0, z_k)|j - k|\Delta z^2. \tag{4.8}$$

It produces exact solution for this mode while the computational cost is marginal. Finally, we reverse the process to inverse Fourier transform $\widetilde{\Phi}_1(k_x, k_y, z)$ in k_x and k_y to derive the fluctuation potential in real space $\Phi_1(x, y, z)$, incorporating the corresponding phase shifts with opposite sign.

In practice, it is not necessary to allocate storage space for the whole extended domain in z-direction. The appended zero density is only involved in the calculation between the forward and inverse Fourier transforms in x and y. In addition, the convolutions in z (Equations (4.6) and (4.7)) for different modes (k_x, k_y) are independent of each other. Therefore, these convolutions can be distributed among processors and performed sequentially by allocating only one one-dimensional working array along z-direction.

4.1.3 Particle Dynamics

We continue to use zero-mass approximation to model our solid particles as in Chapter 3. In this approximation, particles behaves as test particles and only respond to the gravity of the host star and the gas. We ignore viscous force between particles and gas and back reaction from the particles to the gas. This remains a good approximation for kilometer-sized planetesimals (e.g., Oishi et al., 2007). We also ignore mutual gravitational interactions between particles, and this helps us isolate the net effect induced by hydromagnetic turbulence.

The equations of motion for each particle, therefore, become

$$\frac{d\mathbf{x}_p}{dt} = \mathbf{u}_p - \frac{3}{2}\Omega_K x_p \hat{\mathbf{y}}, \tag{4.9}$$

$$\frac{d\mathbf{u}_p}{dt} = \left(2\Omega_K u_{p,y}\hat{\mathbf{x}} - \frac{1}{2}\Omega_K u_{p,x}\hat{\mathbf{y}} - \Omega_K^2 z_p \hat{\mathbf{z}}\right) + \mathbf{g}_0 - \nabla\Phi_1. \tag{4.10}$$

The vector $\mathbf{x}_p = (x_p, y_p, z_p)$ is the position of the particle in the shearing box, while $\mathbf{u}_p = (u_{p,x}, u_{p,y}, u_{p,z})$ is the velocity of the particle relative to the background shear flow. In equation (4.10), the terms inside the parenthesis stem from linearized gravity of the host star and Coriolis and centrifugal forces in the co-rotating frame of the shearing box. The remaining terms on the right-hand side represent the acceleration attributed to the gas: $\mathbf{g}_0$ is the gravitational acceleration due to the basic state of the gas stratification and has analytical expression

$$\mathbf{g}_0(z) = -2\pi^{3/2} G\rho_m H \operatorname{erf}\left(\frac{z}{H}\right)\hat{\mathbf{z}}, \tag{4.11}$$

while Φ_1 is the gravitational potential due to density fluctuation with respect to the basic state and is the solution of the Poisson equation (4.5) (Section 4.1.2). Note that by separating the density perturbation from the equilibrium density stratification and treating the gravity of the equilibrium state exactly, we significantly improve the sampling of the gravitational fluctuation due to hydromagnetic turbulence.

The position $\mathbf{x}_p$ and velocity $\mathbf{u}_p$ of each particle is forwarded in time by integrating the equations of motion (4.9) simultaneously with the third-order Runge-Kutta steps advancing the MHD equations. In addition to the Courant conditions set by the MHD equations, the time-step is limited by the absolute maximum of velocity $\boldsymbol{u}_p$ so that no particles can cross more than half the grid spacing. We calculate the gradient of the fluctuation potential $\nabla\Phi_1$ on the grid and then quadratically interpolate it onto each particle.

We uniformly distribute 128^2 particles in a horizontal plane. These particles do not move until after 20 orbital periods, at the time the turbulence has reached a statistically steady state. We arbitrarily denote this time as $t = 0$. The particles can have an initial eccentricity e_0 by setting an initial velocity $\boldsymbol{u}_p$ so that they are at the apogee of their orbits (see Chapter 3). They can also have an initial inclination i_0 by placing the initial particle plane at a distance to the mid-plane. Particles are wrapped around when crossing any of the six boundary planes of the shearing box.

4.2 Properties of Magneto-rotational Turbulence

In this section, we present several properties of the magneto-rotational turbulence in our numerical models and discuss their convergence with the box size and the resolution.

Figure 4.1 shows the horizontally averaged density fluctuation, inverse plasma β, and α parameter in the mid-plane ($z = 0$) as a function of time, for resolutions up to 64 points per H and horizontal box dimensions up to $L_x = L_y = 16\ H$. The magnitude of the density fluctuation is indicated by the rms value relative to the equilibrium density $\langle \rho_1^2 \rangle^{1/2}/\rho_0$, the plasma $\beta \equiv 2\mu_0\rho_0 c_s^2/\langle |\boldsymbol{B} + \boldsymbol{B}_{\rm ext}|^2 \rangle$ is the ratio of the equilibrium thermal pressure to the magnetic pressure, and α is calculated by (e.g., Brandenburg, 1998)

$$\alpha = \frac{\sqrt{2}}{3} \frac{\langle \rho u_x u_y - B_x B_y/\mu_0 \rangle}{\rho_0 c_s^2}, \tag{4.12}$$

which includes both Reynolds and magnetic stresses. The brackets $\langle\ \rangle$ denote the horizontal average of the property at any given altitude z.

The magneto-rotational turbulence in the mid-plane of our models reaches a statistically steady state at about $t = 20P$. At this saturated state, we see in general that the larger the horizontal size of the box, the smaller the amplitude of oscillation in the turbulence properties. Little difference exists between an $8{\times}8{\times}4H$ box and a $16{\times}16{\times}4H$ box at the same resolution, indicating convergence with horizontal box dimension. On the other hand, the amplitude of oscillation at saturation level increases with resolution for fixed box dimensions. We also note that there exists a curious trend of increase in density perturbation with time for the case of an $8{\times}8{\times}4H$ box at the resolution of 64 points/H. Nevertheless, the time average of each turbulence properties remains roughly the same with respect to resolution.

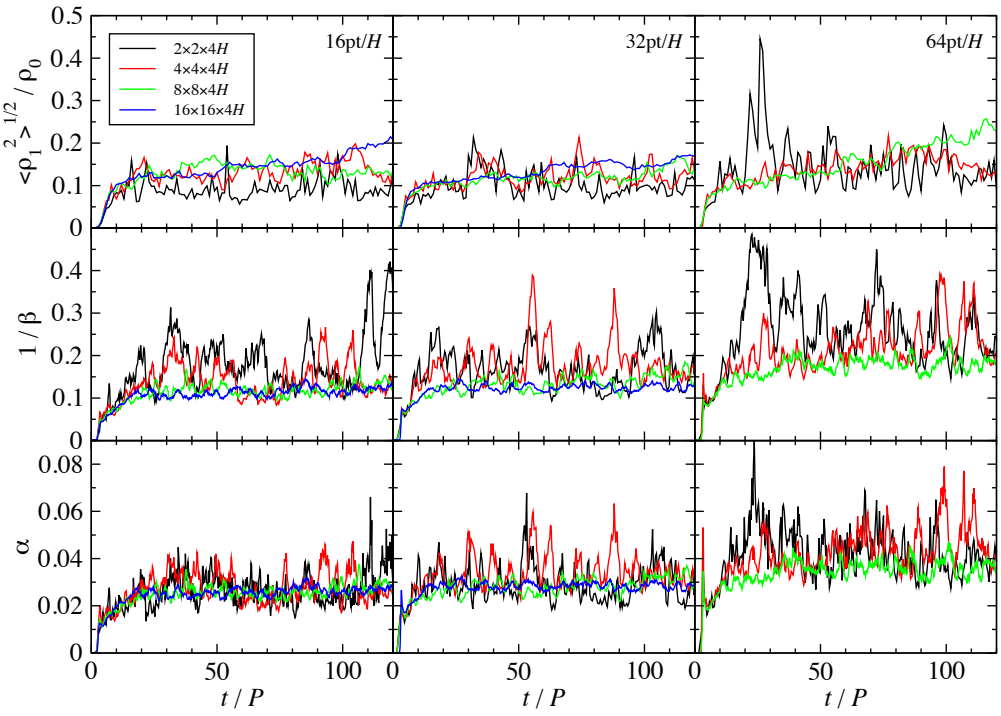

Figure 4.1 Horizontally averaged properties of the modeled magneto-rotational turbulence in the mid-plane as a function of time. The rows of panels from top to bottom are rms density fluctuation, inverse plasma β, and α-parameter, respectively. The columns are arranged with increasing resolution from left to right. Lines of different colors denote measurements from boxes with different dimensions.

The means and standard deviations of the turbulence properties at saturated state for each set of resolution and box dimensions are reported in Table 4.1, which includes the magnetic stress and the Reynolds stress as well.

Figure 4.2 shows the time-averaged vertical profiles of density perturbation, inverse plasma β, and α parameter at saturation level. Each of the three properties increases with $|z|$, indicating stronger turbulence at higher altitude. The increasing activity with altitude is related with the increasing importance of the external magnetic field, which can be quantified by $\beta_{\rm ext}(z)$ (Section 4.1.1). This is in accordance with the same trend found in models of unstratified disks (Hawley et al. 1995; Johansen et al. 2006; Chapter 3). Notice that $\beta_{\rm ext}(\pm 2H) = 1.1 \times 10^2 \gg 1$ at our highest altitude, and thus the corona is not modeled in our simulations. With such a week vertical magnetic field, channel flows developed in the initial stage of MRI can be contained and does not destroy the solution near the mid-plane (in contrast to Miller & Stone, 2000). As shown in Figure 4.2, the time-averaged inverse plasma β near the vertical boundary amounts to only about 0.4, and thus on average, thermal pressure still dominates magnetic pressure there.

4.3 Orbital Properties of Massless Particles

With the statistically steady, numerically convergent magneto-rotational turbulence shown in Section 4.2, we further report the response of zero-mass particles to the gravity of the density fluctuations of this turbulent gas. The reference time $t = 0$ in the following discussion is referred to the time at which the turbulent gas reaches its saturated state and the particles start to move.[2]

4.3.1 Mean Orbital Radius

As discussed in Chapter 3, the evolution of the mean orbital radius of one particle can be found by averaging the radial position x of the particle over each epicycle motion. For the case of ideal unstratified disks, the distribution of particles in terms of the orbital radius

[2]We choose this reference time to be $t = 20P$ reported in Section 4.2. See Figure 4.1.

Table 4.1. Mid-plane Properties of the Magneto-rotational Turbulence

Dimensions $[H]$	Resolution [pt/H]	$\sqrt{\langle\rho_1^2\rangle}/\rho_m$	β^{-1}	$\langle B_x B_y\rangle/\mu_0\rho_m c_s^2$	$\langle\rho u_x u_y\rangle/\rho_m c_s^2$	α
2×2×4	16	0.09±0.02	0.053±0.026	0.019±0.008	0.005±0.003	0.012±0.004
4×4×4	16	0.14±0.02	0.059±0.018	0.024±0.007	0.007±0.002	0.015±0.004
8×8×4	16	0.16±0.03	0.052±0.008	0.022±0.003	0.007±0.001	0.014±0.002
16×16×4	16	0.17±0.03	0.051±0.004	0.022±0.002	0.007±0.001	0.014±0.001
2×2×4	32	0.10±0.03	0.076±0.034	0.028±0.010	0.006±0.003	0.016±0.005
4×4×4	32	0.12±0.03	0.063±0.018	0.026±0.006	0.007±0.002	0.016±0.004
8×8×4	32	0.15±0.04	0.054±0.006	0.024±0.003	0.006±0.001	0.014±0.001
16×16×4	32	0.13±0.01	0.051±0.004	0.023±0.001	0.006±0.001	0.014±0.001
2×2×4	64	0.16±0.06	0.171±0.094	0.055±0.030	0.009±0.006	0.030±0.015
4×4×4	64	0.14±0.03	0.081±0.016	0.034±0.007	0.008±0.002	0.020±0.004
8×8×4	64	0.16±0.04	0.070±0.009	0.030±0.004	0.006±0.001	0.017±0.002

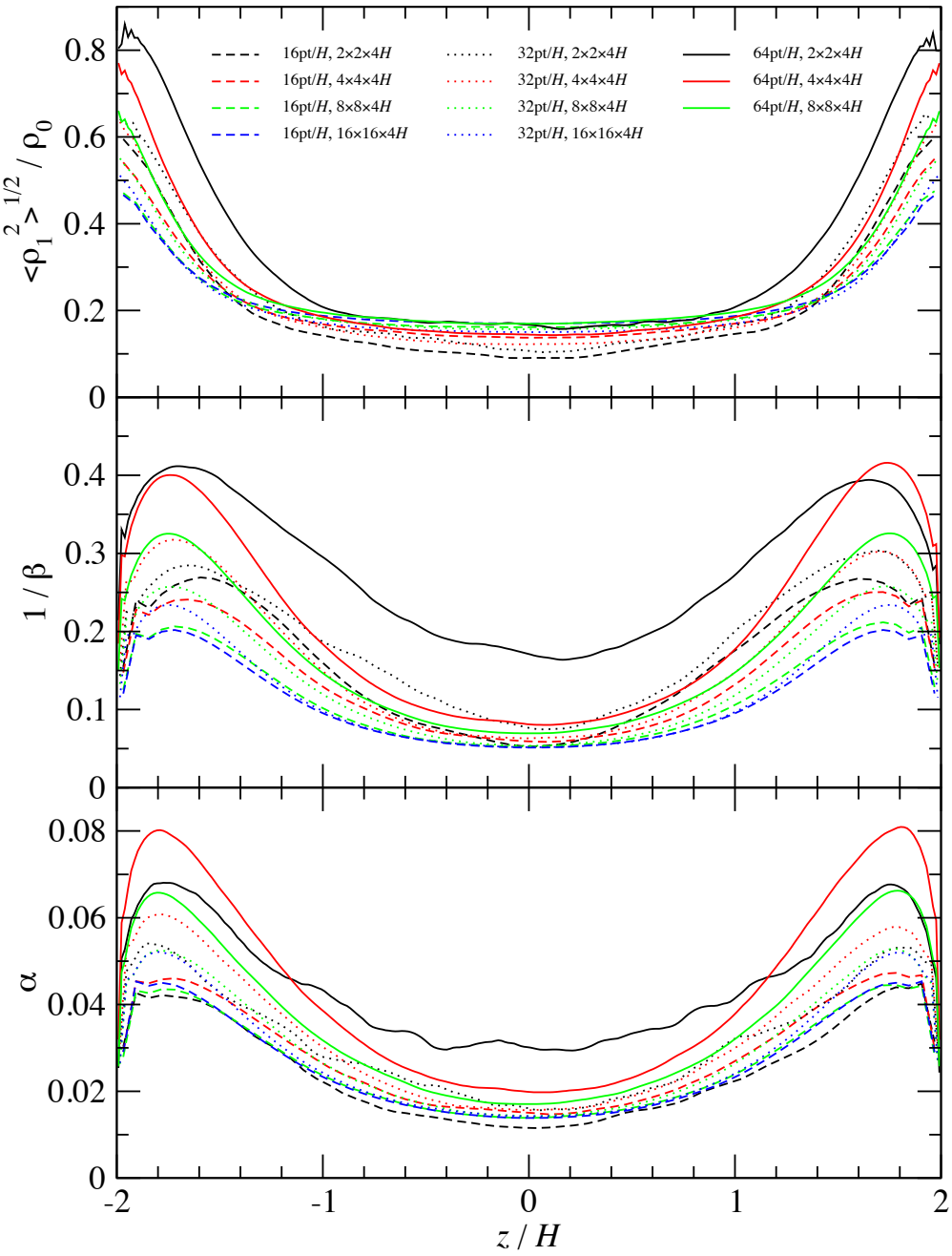

Figure 4.2 Time-averaged vertical profiles of the modeled magneto-rotational turbulence at saturation stage for different resolutions and box dimensions. The panels from top to bottom are rms density fluctuations, inverse plasma β, and α parameter, respectively.

change can be described by a time-dependent normal distribution centered at zero:

$$f(\Delta x, t) = \frac{1}{\sqrt{2\pi}\sigma_x(t)} \exp\left[-\frac{\Delta x^2}{2\sigma_x^2(t)}\right], \tag{4.13}$$

where Δx is the orbital radius change from the initial radius x_0 at $t = 0$ and $\sigma_x(t)$ is the time-dependent standard deviation. We reported in Chapter 3 that $\sigma_x(t)$ depends on the properties of the gas disk and can be concisely expressed by

$$\sigma_x(t) = C_x \xi H \left(\frac{t}{P}\right)^{1/2}, \tag{4.14}$$

where C_x is a dimensionless proportionality constant[3] and $\xi \equiv 4\pi G\rho_0 P^2$ is a dimensionless quantity indicating the strength of the gas gravity. Equations (4.13) and (4.14) demonstrate the diffusive nature of particle radial migration driven by magneto-rotational turbulence.

For the case of ideal stratified disks studied here, we again find the evolution of particle orbital radius can be described by Equations (4.13) and (4.14). The dimensionless quantity ξ is now defined by

$$\xi \equiv 4\pi G\rho_m P^2 \tag{4.15}$$

in terms of the mid-plane gas density ρ_m. In Table 4.2, we report the measured values of the constant C_x from our simulations at different resolutions and horizontal box sizes. Comparing the value from the $2\times2\times4H$ stratified model at a resolution of 64 points/H with that from the unstratified model at the same resolution and horizontal box size (see Equation (15) of Chapter 3), we find excellent agreement in the two C_x values.

As can be seen from Table 4.2 and Figure 4.3, the value of C_x remains roughly the same with different resolutions for given box dimensions (except the anomaly shown by the $2\times2\times4H$ box at a resolution of 64 points/H). Conversely, it is significantly dependent on the horizontal box size $L_h \equiv L_x = L_y$. The larger the size, the stronger the effect of the turbulence on particle orbital radius. This relationship can be represented by the following power-law fit:

$$C_x \simeq (6.2 \times 10^{-5})(L_h/H)^{1.38}. \tag{4.16}$$

We find no evidence of convergence with horizontal box size up to $L_h = 16H$, the largest size we have investigated.

[3] C_x as well as other dimensionless constants introduced in the following discussions may depend on the α parameter. This dependency is not investigated in this work.

Table 4.2. Dynamical Properties of the Massless Particles with $e_0 = 0$ and $i_0 = 0$

Dimensions $[H]$	Resolution [pt/H]	C_x	C_e	C_i	S_x	S_z	ϵ	γ
2×2×4	16	2.3×10^{-4}	2.3×10^{-4}	1.2×10^{-4}	3.4×10^{-4}	1.8×10^{-4}	7.7×10^{-5}	1.1×10^{-4}
4×4×4	16	4.4×10^{-4}	3.4×10^{-4}	1.8×10^{-4}	4.9×10^{-4}	3.0×10^{-4}	2.8×10^{-4}	1.7×10^{-4}
8×8×4	16	1.3×10^{-3}	7.6×10^{-4}	1.8×10^{-4}	1.1×10^{-3}	3.2×10^{-4}	2.7×10^{-3}	3.8×10^{-4}
16×16×4	16	3.0×10^{-3}	1.6×10^{-3}	1.6×10^{-4}	2.4×10^{-3}	3.4×10^{-4}	1.4×10^{-2}	8.2×10^{-4}
2×2×4	32	2.5×10^{-4}	2.5×10^{-4}	1.4×10^{-4}	3.6×10^{-4}	2.0×10^{-4}	9.4×10^{-5}	1.2×10^{-4}
4×4×4	32	3.7×10^{-4}	3.1×10^{-4}	1.7×10^{-4}	4.5×10^{-4}	2.4×10^{-4}	2.0×10^{-4}	1.5×10^{-4}
8×8×4	32	1.1×10^{-3}	6.3×10^{-4}	1.6×10^{-4}	9.1×10^{-4}	2.8×10^{-4}	1.7×10^{-3}	3.1×10^{-4}
16×16×4	32	2.4×10^{-3}	1.3×10^{-3}	1.5×10^{-4}	1.9×10^{-3}	3.1×10^{-4}	8.4×10^{-3}	6.6×10^{-4}
2×2×4	64	3.8×10^{-4}	4.4×10^{-4}	2.8×10^{-4}	6.8×10^{-4}	4.7×10^{-4}	2.2×10^{-4}	2.2×10^{-4}
4×4×4	64	4.0×10^{-4}	3.4×10^{-4}	1.7×10^{-4}	4.8×10^{-4}	3.0×10^{-4}	2.5×10^{-4}	1.7×10^{-4}
8×8×4	64	1.1×10^{-3}	6.6×10^{-4}	1.5×10^{-4}	9.6×10^{-4}	3.0×10^{-4}	1.9×10^{-4}	3.2×10^{-4}

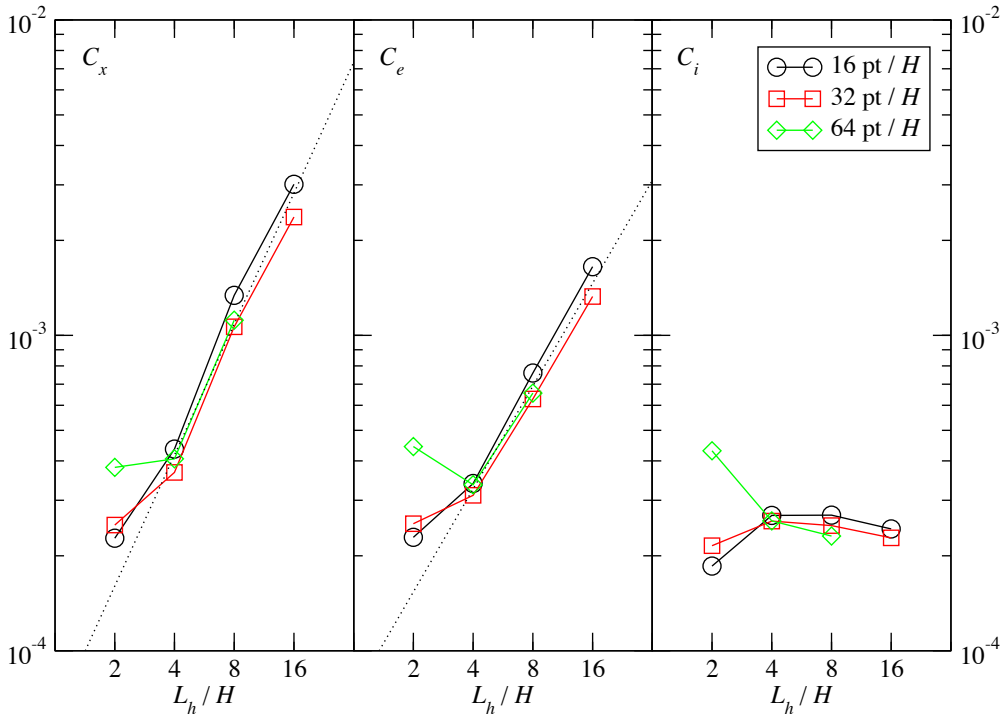

Figure 4.3 Dimensionless proportionality constants C_x, C_e, and C_i as a function of horizontal box size $L_h = L_x = L_y$. They indicate the strength of diffusion in mean orbital radius, eccentricity, and inclination of massless particles moving in magneto-rotational turbulence and are defined in Equations (4.14), (4.19), and (4.25), respectively. The dotted lines are power-law fits to data points with $L_h \geq 4H$.

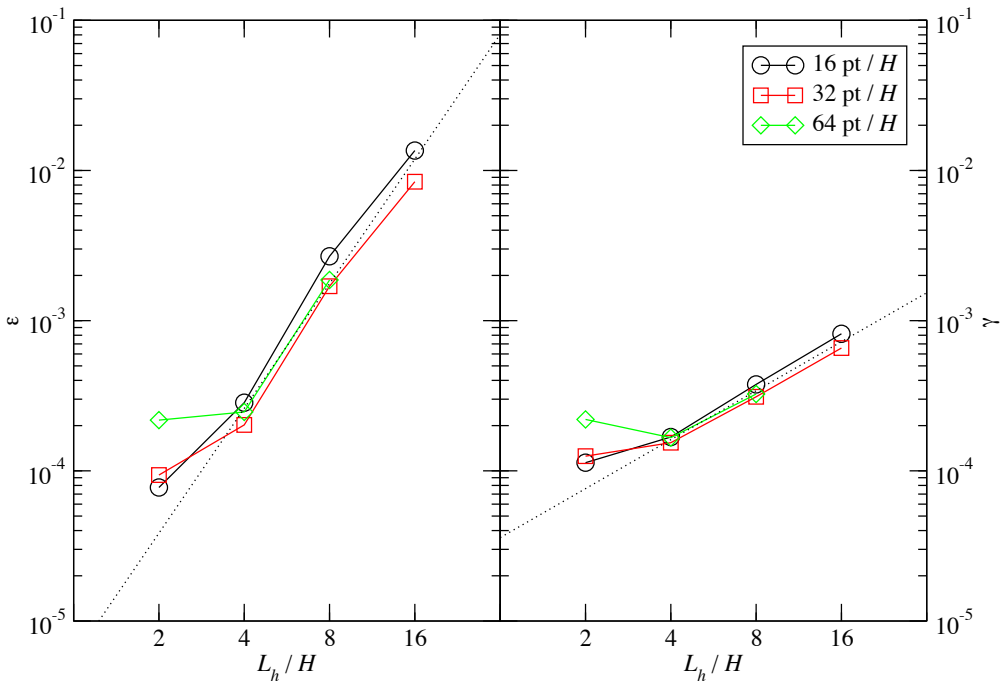

Figure 4.4 Dimensionless constants ϵ and γ as a function of horizontal box size L_h. The constant ϵ indicate the strength of diffusive migration driven by turbulence and was defined by Johnson et al. (2006), while γ is related with the strength of eccentricity excitation (when $e_0 = 0$) due to turbulence and was defined by Ida et al. (2008). The dotted lines are power-law fits to data points with $L_h \geq 4H$.

Equation (4.14) can be transformed into the diffusion coefficient $D(J)$ for describing the radial random walks of orbiting particles induced by turbulent torques, in terms of the Keplerian orbital angular momentum J. The reader is referred to Chapter 3 for a detailed description of this procedure. We emphasize here that this transformation involves no assumption of the correlation time of the stochastic torques and is thus a direct measurement of $D(J)$. Using a heuristic choice of dimension for the diffusion coefficient, Johnson et al. (2006) defined a dimensionless parameter ϵ to represent the magnitude of $D(J)$. We report our measured values of ϵ in Table 4.2. The dependence of ϵ on the horizontal box size L_h in our models for $L_h \gtrsim 4H$ is shown in Figure 4.4 and can be written as

$$\epsilon \simeq (5.7 \times 10^{-6})(L_h/H)^{2.76}. \tag{4.17}$$

4.3.2 Eccentricity

The amplitude of each epicyclic oscillation of a particle gives the instantaneous eccentricity of the particle orbit. We reported in Chapter 3 that in ideal unstratified disks, the distribution of particles in terms of the eccentricity deviation should be a time-dependent normal distribution centered at zero, as long as the particles have non-negligible initial eccentricity (c.f. Equation (4.13)):

$$f(\Delta e, t) = \frac{1}{\sqrt{2\pi}\sigma_e(t)} \exp\left[-\frac{\Delta e^2}{2\sigma_e^2(t)}\right], \tag{4.18}$$

where Δe is the eccentricity deviation from the initial eccentricity e_0 at $t = 0$ and the time-dependent standard deviation $\sigma_e(t)$ can be written as

$$\sigma_e(t) = C_e \xi \left(\frac{H}{R}\right) \left(\frac{t}{P}\right)^{1/2}, \tag{4.19}$$

with C_e being a dimensionless proportionality constant. We emphasize that the time-dependent Rayleigh distribution found for particles with zero (or negligible) initial eccentricity

$$f(e, t) = \frac{e}{\sigma_e^2(t)} \exp\left[-\frac{e^2}{2\sigma_e^2(t)}\right] \tag{4.20}$$

is a manifestation of Equation (4.18) since the eccentricity e is a positive definite quantity. Equations (4.18) and (4.20) share the same time-dependent parameter $\sigma_e(t)$, and there exists no evidence that $\sigma_e(t)$ depends on the initial eccentricity e_0.

We find that the same evolution of particle distribution in eccentricity deviation also holds for the case of ideal stratified disks. The measured values of the constant C_e for different resolutions and horizontal box sizes are listed in Table 4.2. The same comparison performed in Section 4.3.1 for the orbital radius evolution indicates that the eccentricity evolution in a stratified disk again agrees very well with that in an unstratified disk (see Equation (17) of Chapter 3). These comparisons demonstrate that a local unstratified disk model gives consistent results with the mid-plane of a local stratified disk model that has the same physical conditions except vertical stratification.

As in the case of orbital radius discussed in Section 4.3.1, the eccentricity evolution of the particles does not noticeably depend on the resolution for given box dimensions, while strongly affected by the horizontal box size (Table 4.2 and Figure 4.3). A power-law

regression gives

$$C_e \simeq (7.2 \times 10^{-5})(L_h/H)^{1.08}, \tag{4.21}$$

which is close to a linear relation on the horizontal box size. We dedicate the discussion of the box-size effect on both orbital radius and eccentricity of the massless particles in Section 4.4.

The eccentricity evolution driven by magneto-rotational turbulence enhances orbital crossing among planetesimals and thus increases the chance of collisions between them. Ida et al. (2008) defined a dimensionless parameter γ to represent the strength of this effect. Equation (4.19) can be used to estimate the value of γ, and the reader is referred to Chapter 3 for a detailed description of this procedure. We report in Table 4.2 our measured values of γ. As shown in Figure 4.4, the dependence of γ on the horizontal box size L_h in our models for $L_h \gtrsim 4H$ can be described by

$$\gamma \simeq (3.6 \times 10^{-5})(L_h/H)^{1.08}. \tag{4.22}$$

4.3.3 Inclination

The only orbital property of a particle that cannot be measured from an unstratified disk model is the inclination i. In a stratified disk, vertical linear gravity from the host star (the third term in the parenthesis on the right-hand side of Equation (4.10)) provides a restoring force such that particles oscillate in z-direction centered at the mid-plane, as demonstrated in Figure 4.5. Note that because the particles also experience the gravity of the gas, the period of the oscillation is $P\left(1+\xi/4\pi^2\right)^{-1/2}$ in the linear limit (derived from Equations (4.10) and (4.11)), which is slightly shorter than the orbital period P. We can calculate the induced inclination (in radians) for a single particle by $i \approx \left(z_{\max} - z_{\min}\right)/2R$, in which $z_{\max}$ and $z_{\min}$ are the maximum and the minimum vertical positions in one oscillation, respectively, provided that $z/R \ll 1$.

Figure 4.6(a) shows the histograms of particles with zero initial inclination in bins of their instantaneous inclination at three different times. Similar to the eccentricity distribution for particles with $e_0 = 0$ described by Equation (4.20), the inclination distribution resembles a time-dependent Rayleigh distribution

$$f(i,t) = \frac{i}{\sigma_i^2(t)} \exp\left[-\frac{i^2}{2\sigma_i^2(t)}\right], \tag{4.23}$$

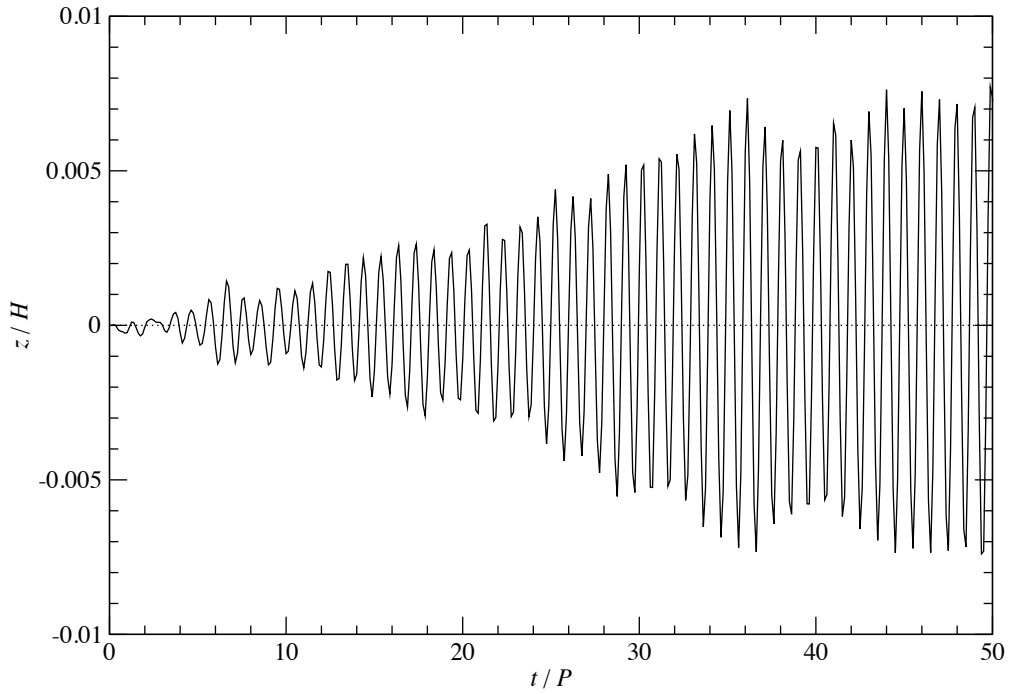

Figure 4.5 Vertical displacement of one example massless particle moving in a stratified, turbulent gas disk. The disk has the dimension of $8\times8\times4H$, the resolution of 16 points per disk scale height H, and the strength of disk gravity $\xi = 1$. The particle has zero initial inclination.

where $\sigma_i(t)$ is a time-dependent parameter. Learning from the experience when we studied the eccentricity, we conjecture that Equation (4.23) could also be a special case of a zero-centered normal distribution

$$f(\Delta i, t) = \frac{1}{\sqrt{2\pi}\sigma_i(t)} \exp\left[-\frac{\Delta i^2}{2\sigma_i^2(t)}\right], \tag{4.24}$$

where Δi is the inclination deviation from the initial inclination i_0 at $t = 0$. Indeed, it is the case as demonstrated by Figure 4.6(b) for particles with $i_0 = 0.1(H/R)$ moving in an $8{\times}8{\times}4H$, $\xi = 1$ gas disk at a resolution of 32 points/H.

Figure 4.7 shows $\sigma_i(t)$ for disks with varying gravity parameter ξ and particles with varying initial inclination i_0. Note that $\sigma_i(t)$ is normalized by ξ and H/R and the curves roughly coincide. This indicates that $\sigma_i(t)$ is linearly dependent on both ξ and H/R. The results can be summarized by the following expression:

$$\sigma_i(t) = C_i \xi \left(\frac{H}{R}\right)\left(\frac{t}{P}\right)^{1/2}, \tag{4.25}$$

where C_i is a dimensionless proportionality constant. We caution that although there exists no noticeable change by varying the initial inclination i_0, it does not prove $\sigma_i(t)$ is independent of i_0. Since an inclination of $i = 0.1(H/R)$ represents small-amplitude vertical oscillations, the motion of the particles does not cover significant vertical height and thus is not sensitive to the vertical stratification of the gas.

Table 4.2 lists our measured values of the constant C_i for different resolutions and box dimensions. We note that in contrast to orbital radius and eccentricity, the evolution of orbital inclination is not significantly affected by resolution or horizontal box size.

4.3.4 Velocity Dispersion

Finally, all three components of velocity dispersion $\boldsymbol{\sigma}_u$ among the particles as a function of time can be measured in our stratified disk models. Similarly to what we reported in Chapter 3, each component assumes the same form:

$$\sigma_{u,i}(t) = S_i \xi c_s \left(\frac{t}{P}\right)^{1/2}, \tag{4.26}$$

where the index i is either x, y, or z and S_i is the corresponding dimensionless proportionality constant. We emphasize that $S_y \sim S_x/2$ always holds due to fixed ratio of amplitudes in

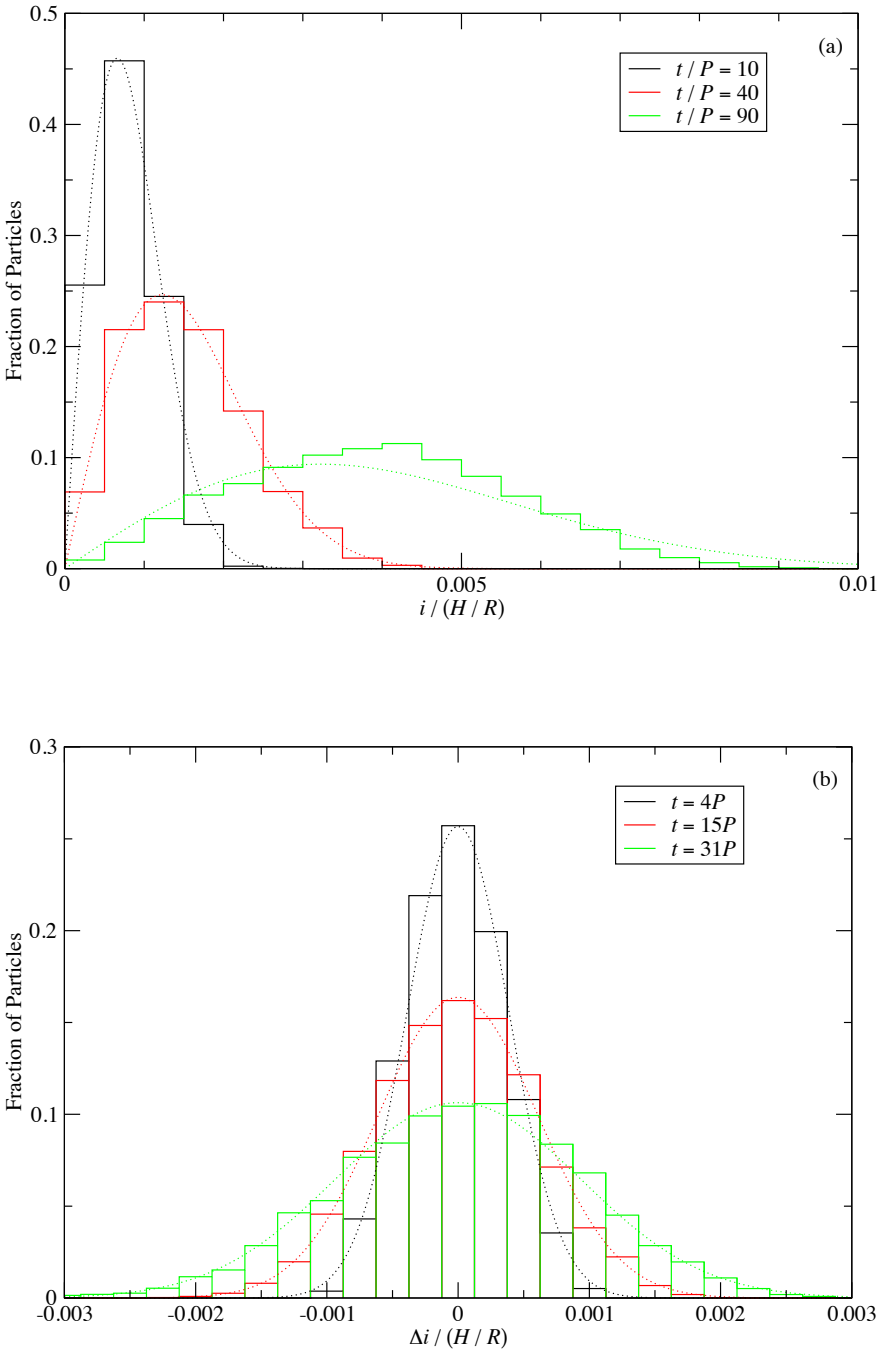

Figure 4.6 Histograms of particles at three different times in bins of (a) orbital inclination i when the particles have zero initial inclination and (b) orbital inclination deviation $\Delta i \equiv i - i_0$ when the particles have an initial inclination of $i_0 = 0.1(H/R)$. The disk has the dimensions of $8\times8\times4H$, the resolution of 32 points/H, and the strength of disk gravity $\xi = 1$. The dotted-lines are the best-fits using (a) Rayleigh distribution and (b) normal distribution, respectively.

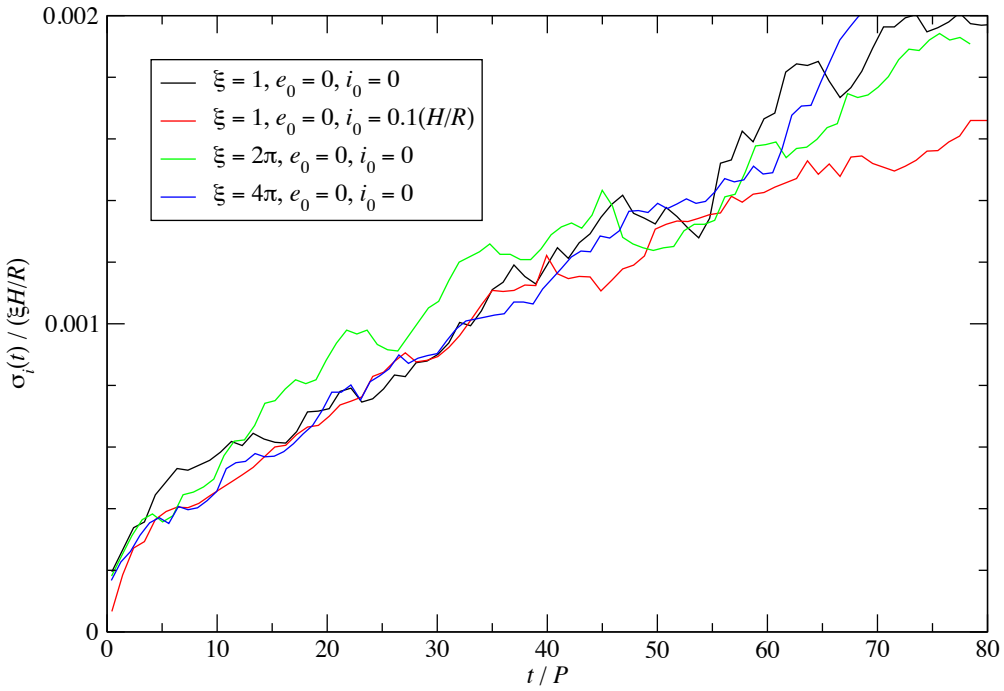

Figure 4.7 Parameter $\sigma_i(t)$ as a function of time t, indicating the evolution of width in inclination distribution for disks with varying strength of gravity and particles with varying initial inclinations. The disk has the dimensions of $8\times8\times4H$ and the resolution of 32 points/H.

x and y directions in the epicycle motions of the particles, which has been verified in our simulations. The values of S_x and S_z at different resolutions and box dimensions are listed in Table 4.2. Note that the value of S_x for the $2{\times}2{\times}4H$ box at a resolution of 64 points/H is consistent with that from the unstratified disk with the same horizontal size and resolution we reported previously (see Equation (18) of Chapter 3), a further confirmation of the consistency between stratified and unstratified models discussed in Sections 4.3.1 and 4.3.2.

As shown by Figure 4.8, we do not see evident dependence of velocity dispersion on resolution of our models. On the other hand, the horizontal component S_x (and thus S_y) significantly depends on the horizontal box size L_h while the vertical component S_z does not. This is in accordance with the dependence of the three orbital properties found in previous subsections. From our measured values for $L_h \geq 4H$, we quantify S_x and S_z by the following expressions:

$$S_x \simeq (1.0 \times 10^{-4})(L_h/H)^{1.09}, \tag{4.27}$$

$$S_z \simeq 3.0 \times 10^{-4}. \tag{4.28}$$

4.4 Issues of Convergence with Horizontal Box Size

We have demonstrated in Section 4.2 that various properties of the saturated magneto-rotational turbulence in our simulations converge with both resolution and box dimensions. However, while converging with resolution, the response of massless particles to the gravity of density fluctuations in the turbulent gas does not likewise converges with the horizontal box size, as shown in Section 4.3. This result raises serious concerns about the validity of using the local shearing box to simulate the dynamics of any particles under gravitational influence of magneto-rotational turbulence. We discuss the cause of this result and related issues in the following subsections.

4.4.1 Fourier Analysis of the Gas Density

Since the density structure of the turbulent gas directly affects its gravitational influence on the particles, it is informative to consider how the structure changes with resolution and horizontal box size. Figure 4.9 plots the time-averaged Fourier amplitudes of the gas

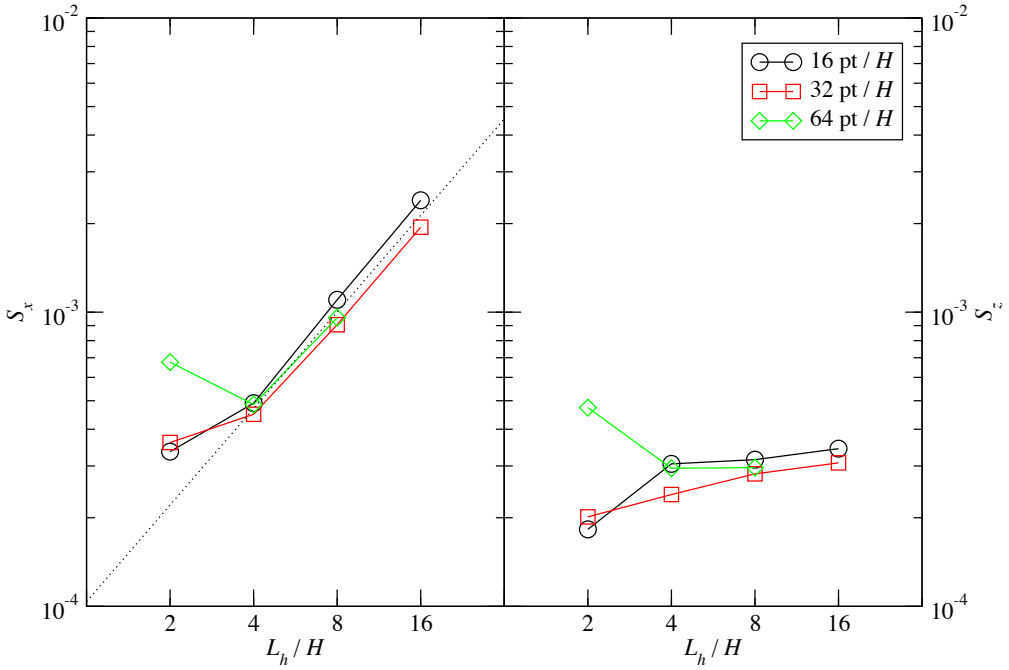

Figure 4.8 Dimensionless proportionality constants S_x and S_z as a function of horizontal box size L_h. They indicate the strength of turbulence excitation in vertical and radial velocity dispersions among massless particles and are defined in Equation (4.26). The dotted line is the power-law fit to S_x with $L_h \geq 4H$.

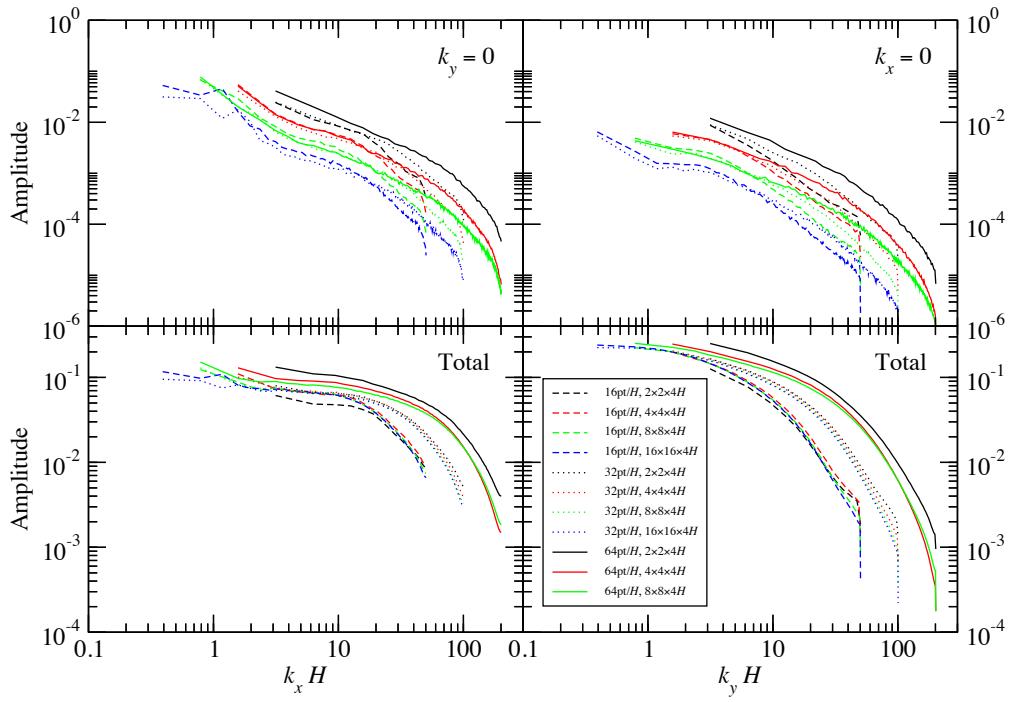

Figure 4.9 Time-averaged Fourier amplitudes of the density fluctuation of saturated magneto-rotational turbulence in the mid-plane for different resolutions and box dimensions. The amplitudes are averaged over a period of over $100P$. The top-left panel shows $|\widetilde{\rho}(k_x, k_y = 0, z = 0)|$, while the bottom-left panel the summation of $|\widetilde{\rho}(k_x, k_y, z = 0)|$ over k_y. Similarly, the top-right panel shows $|\widetilde{\rho}(k_x = 0, k_y, z = 0)|$, while the bottom-right panel the summation of $|\widetilde{\rho}(k_x, k_y, z = 0)|$ over k_x.

density in the mid-plane along either radial or azimuthal direction. The top-left panel shows the amplitude as a function of k_x for $k_y = 0$. In general, the largest amplitude resides at the longest wavelength while monotonically decreasing with increasing frequency (Johansen et al., 2009). For any given box dimensions, increasing resolution has little effect on each amplitude, only to extend the profile toward higher frequency. Flattening of the profile for wavelengths $\gtrsim 8H$ is hinted by $16\times16\times4H$ boxes. We find no evidence of downward turn toward even longer wavelength. On the other hand, increasing the horizontal box size L_h lowers the overall profile of the Fourier amplitudes. Interestingly, the amplitude of the fundamental mode $k_x = k_0 \equiv 2\pi/L_h$ remains roughly constant.

The bottom-left panel of Figure 4.9 plots the summation of Fourier amplitudes over all k_y at any given k_x. In contrast to the amplitudes for $k_y = 0$, horizontal box size L_h has little effect on the amplitudes for most of the wavelengths. Nevertheless, increasing resolution

indeed increases the inertial range and resolves more power toward shorter wavelength.

The right-hand column of Figure 4.9 plots the azimuthal counterpart of the left-hand column. We find similar features in the azimuthal amplitudes as those found in the radial ones. The only difference is that the flat part of the spectrum in the azimuthal direction is short compared with that in the radial direction, as can be seen in the bottom-right panel. Uncaptured power in the long-wavelength range of the spectrum in the $2\times2\times4H$ boxes is probably the cause for artificially higher amplitude at $(k_x, k_y) = (0, k_0)$ (the top-right panel), which may in turn be responsible for the anomaly found in the particle dynamics shown in Section 4.3.

The Fourier amplitudes shown in Figure 4.9 help us understand the dependence of the particle response to the gas gravity on the horizontal box size. The eccentricity deviation and the radial diffusive migration discussed in Sections 4.3.2 and 4.3.1 are in fact driven by the x and the y components of the gravitational force of the gas, respectively. The magnitudes of these force components for any given (horizontal) Fourier mode $\boldsymbol{k} = (k_x, k_y)$ are related with the corresponding Fourier amplitude $\breve{\rho}(\boldsymbol{k})$ by (see Equation (4.6))

$$F_x(\boldsymbol{k}) \sim 4\pi G \left(\frac{k_x}{k^2}\right) |\breve{\rho}(\boldsymbol{k})| \lesssim 4\pi G \frac{|\breve{\rho}(k_0, 0)|}{k_0} \propto L_h, \tag{4.29}$$

$$F_y(\boldsymbol{k}) \sim 4\pi G \left(\frac{k_y}{k^2}\right) |\breve{\rho}(\boldsymbol{k})| \lesssim 4\pi G \frac{|\breve{\rho}(0, k_0)|}{k_0} \propto L_h, \tag{4.30}$$

where we have used the facts that the dominant modes in the radial and the azimuthal directions are the fundamental modes and both $|\breve{\rho}(k_0, 0)|$ and $|\breve{\rho}(0, k_0)|$ are about constant. Therefore, both components should be linearly proportional to the horizontal box size in our simulations.

The linear dependence of the gravitational force of the turbulent gas on the horizontal box size, Equations (4.29) and (4.30), satisfactorily explains our measured dependence of eccentricity evolution and horizontal velocity dispersion of massless particles (Equations (4.21) and (4.27)) while accounting for that of the orbital radius evolution for the most part (Equation (4.16)). The slightly steeper slope of C_x versus L_h might be due to the crudeness of our single-mode analysis and the contributions from several non-fundamental modes. We note that this slope may decrease with increasing L_h, as suggested by the left panel of Figure 4.3. To confirm this trend will require even larger azimuthal box dimension than we have

investigated in this work.

Johansen et al. (2009) have discussed the dominant role of the radial fundamental mode $\boldsymbol{k} = (k_0, 0)$ in great detail and suggested this kind of persistent structures are similar to the zonal flows found in many other astrophysical systems. The particle dynamics presented in this work is closely related with these structures. We emphasize here that although the axisymmetric components ($k_y = 0$) of the density fluctuation in the gas does not affect the radial diffusive migration of particles, they are in fact still responsible for driving the evolution of the orbital eccentricity of these particles. Furthermore, the azimuthal fundamental mode $\boldsymbol{k} = (0, k_0)$ in the gas structure is so significant that the radial diffusive migration of the particles are similarly affected by the box dimensions.

4.4.2 Bridge to a Global Disk Model?

It is not clear how a local shearing box could be connected to a global disk model so that both models would give consistent results on the particle dynamics under the gravitational influence of the density fluctuations in magneto-rotational turbulence. By measuring the correlation lengths in the density field, Guan et al. (2009) also found extended density features in contrast to well localized magnetic structures and suggested that they are propagating acoustic MHD waves excited by the turbulence (also see Heinemann & Papaloizou, 2009a,b). It is crucial to measure the dissipation scale for these waves and identify the critical length scale that can capture all the features in the density fluctuations excited by magneto-rotational turbulence. This measurement is beyond the scope of this work and remains to be investigated.

On the other hand, a global disk model may require high resolution in order to self-consistently produce large-scale structures. For example, Johansen et al. (2009) showed that the inverse cascade of magnetic energy from small scales to large scales may be responsible for ultimately launching zonal flows. To confirm this mechanism in a global context, a model that is able to resolve the correlation lengths in the magnetic structures might be necessary.

We conjecture at this point that the criterion $L_h/R \sim 1$ might be able to set this critical scale for a local shearing box. At this scale, the local-shearing-box approximation formally breaks down since it assumes $L/R \ll 1$. The curvature terms become important and might

trigger turbulent eddies to damp propagating waves. If this conjecture could be verified, Equations (4.16), (4.21) and (4.27) would prove to be useful in evaluating the gravitational influence of the turbulent gas on particle dynamics. As an example, for an aspect ratio of $H/R \sim 0.1$ in a protoplanetary disk, we should simulate a local shearing box with $L_h \sim 10H$ and our models would predict that

$$\begin{cases} C_x & \simeq & 1.5 \times 10^{-3} \\ C_e & \simeq & 8.8 \times 10^{-4} \\ S_x & \simeq & 1.3 \times 10^{-4} \end{cases} \qquad (H/R \sim 0.1 \text{ and } \alpha \sim 10^{-2}). \tag{4.31}$$

In Section 3.4 of Chapter 3, we specifically compared with the global model of Nelson (2005) and found the magnitude of radial diffusive migration in our simulations was about a factor of three smaller than that of Nelson (2005). This remains roughly true according to Equation (4.31). Using the same procedure as done in Chapter 3, we find the standard deviation of $e/(\xi H/R)$ for the six massless particles reported by Nelson (2005) is about 0.005 at $t \simeq 90P$, giving an estimate of $C_e \simeq \sigma_e(\xi H/R)^{-1}(t/P)^{-1/2} \simeq 8 \times 10^{-4}$.[4] This is in close agreement with our prediction of Equation (4.31). Six particles represent a small number of statistics, however, and increasing the number of particles in a global model might reduce the outcomes of the statistics we have performed here (Richard P. Nelson 2009, private communication). Therefore, the comparisons are not meant to be accurate and conclusive.

4.4.3 Implications to Planet Formation and Migration

As discussed in the previous subsection, if the criterion $L_h/R \sim 1$ could be justified, Equations (4.17) and (4.22) would give

$$\begin{cases} \epsilon & \simeq & 3.3 \times 10^{-3} \\ \gamma & \simeq & 4.4 \times 10^{-4} \end{cases} \qquad (H/R \sim 0.1 \text{ and } \alpha \sim 10^{-2}). \tag{4.32}$$

The value of the ϵ parameter in Equation (4.32) is about one order of magnitude higher than what was reported in Chapter 3 for the case of a 2×2×2H unstratified box, while the value of the γ parameter is only about a factor of two larger.

We suggested in Chapter 3 that in a typical protoplanetary disk, the radial diffusive migration of proto-planets induced by magneto-rotational turbulence may be unimportant

[4]Note that the standard deviation of a Rayleigh distribution (Equation (4.20)) is equal to $\sigma_e\sqrt{(4-\pi)/2}$. Also note that there exists a factor of $\sqrt{2}$ difference between our definition of disk scale height H and Nelson's (2005).

compared to the secular migration like type I. According to Johnson et al. (2006), for the diffusive migration to be able to dominate over type I migration, the ϵ parameter should be greater than or about 0.1–1. Our new measurement $\epsilon \simeq 3 \times 10^{-3}$ remains orders of magnitude smaller than this transition value. Therefore, our previous remark on the unimportance of planetary diffusive migration may still hold even though ϵ is increased by one order of magnitude.

We also argued in Chapter 3 that kilometer-sized planetesimal moving in magneto-rotational turbulence may survive from mutual collisional destruction, except in the inner region of a young proto-planetary disk. This was based on the results of Ida et al. (2008) for the cases of $\gamma = 10^{-3}$ and 10^{-4}. Since our new measurement $\gamma \simeq 4 \times 10^{-4}$ does not fall outside this range, the same scenarios may still apply.

4.5 Summary

Directly extending our previous publication (Chapter 3), we continue to study massless particles moving under gravitational influence of density fluctuations of saturated magneto-rotational turbulence in a local, isothermal, Keplerian gas disk. We include linearized vertical gravity from the host star and thus the gas disk is vertically stratified. For comparison purposes, the conditions in the mid-plane of the vertically stratified disks are exactly the same as those in the unstratified disks of Chapter 3.

In order to accurately measure the gravitational effect of the turbulent gas, we separate the gas density ρ into two components: the basic state $\rho_0(z)$ for the vertical hydrostatic equilibrium (Equation (4.4)) and the density deviation $\rho_1 \equiv \rho - \rho_0$ from this basic state. We use the exact gravitational acceleration due to the basic state (Equation (4.11)) and only solve the Poisson equation for the gravitational potential due to the density deviation (Equation (4.5)). We emphasize that since the Poisson equation is linear in density, this approach does not assume small density fluctuations. Furthermore, we implement isolated boundary conditions in vertical direction and thus any density fluctuation outside the vertical computational domain is neglected.

By imposing a weak, uniform external magnetic field, we maintain a constant level of saturated magneto-rotational turbulence in the mid-plane. Several turbulence properties

demonstrate convergence with both resolution up to 64 points per disk scale height H and horizontal box size up to $16H$. The Shakura & Sunyaev (1973) α parameter in the mid-plane of our models is controlled at the level of $\sim 10^{-2}$.

However, even though the properties of the gas are numerically convergent, the dynamics of massless particles moving under the gravity of this turbulent gas does not converge with the horizontal box size L_h. The larger the horizontal box size, the stronger the gravitational effect of the gas on the particles. Specifically, the evolution of the orbital radius, the eccentricity, and the horizontal velocity dispersion of the particles is roughly linearly dependent on L_h up to $16H$. This trend was also found in our unstratified models (Chapter 3), and we find consistency between the unstratified models and the mid-plane of the stratified models. In contrast to the horizontal components of the particle movement, we find the evolution of the inclination and the vertical velocity dispersion is not significantly affected by L_h.

The dependence of particle dynamics on horizontal box size can be traced back to the density structure of the gas. Consistent with the large-box models studied by Johansen et al. (2009), the fundamental mode dominate the density spectrum along radial direction in our models. Furthermore, we also find that the fundamental mode in azimuthal direction is also important in affecting the particle dynamics. The former drives the eccentricity while the latter drives the orbital radius. The powers of these fundamental modes are roughly constant against the horizontal box size. Using a simple single-mode analysis, we demonstrate the linear dependence of the particle response is a natural outcome of these findings in the density spectrum.

Lack of convergence in particle dynamics poses major difficulty in interpreting local-shearing-box models involving gravitational physics of magneto-rotational turbulence. At this point, we can only conjecture that $L_h \sim R$, where R is the distance of the box center to the host star, might be a natural scale of choice for a local model to approach reality. If this conjecture could be verified, we find that our previous remarks in Chapter 3 on the unimportance of radial diffusive migration of proto-planets as well as the survivability of kilometer-sized planetesimals under collisional destruction might still hold valid. Ultimately, high-resolution global disk models and detailed comparisons might be necessary to reconcile the inconsistency we have been finding.

Chapter 5

Concluding Remarks

It has been three decades since Goldreich & Tremaine (1980) pointed out that planets embedded in a gas disk might undergo problematically rapid migration, implying the existence of planetary systems might be a rarity. Not until the first discovery of extrasolar planets in 1995 did this issue resurface and challenge our understandings of the survivability of these planets. As of today, identifying mechanisms that can mitigate this difficulty remains an active research topic. This dissertation presents itself as just one of the numerous attempts toward this goal.

Although one-dimensional, viscous disk models serve as an efficient tool to study the evolution of protoplanetary accretion disks, we caution that several instabilities are suppressed because of the assumption of nearly fixed rotation law behind these models. Given that protoplanetary disks may develop narrow features that may effectively delay or reverse the rapid inward type I migration, we urge that one needs to explicitly check the stability of such features at each time-step in the viscous disk models. Whenever any instability is detected, implementing an adjustment scheme to recover marginal stability is necessary to self-consistently evolve these disk models.

To accurately quantify the effect of the gravitational influence of density fluctuations in magneto-rotational turbulence on the orbital motion of planetesimals and protoplanets, we use the local-shearing-box approximation to simultaneously evolve a magnetically unstable gas disk and numerous massless particles. We find the change in orbital radius and eccentricity of these particles is roughly linearly dependent on the horizontal box size of the local shearing box. Both unstratified disks and the mid-plane of vertically stratified disks give

consistent results. This lack of convergence calls into question the validity of using a local shearing box to study the gravitational physics of magneto-rotational turbulence.

Based on heuristic arguments, nevertheless, some implications to planet formation scenarios might be drawn from the measurements of our numerical simulations. On one hand, the radial random walks of protoplanets induced by a turbulent gas disk may be unimportant compared with secular orbital migration. On the other hand, the orbital crossing of kilometer-sized planetesimals driven by the turbulence may not be strong enough to endanger them with mutual collisional destruction.

To conclude, the results reported in this dissertation have been unexpected and intriguing. More issues are raised than problems are resolved. To elucidate these new-found issues, the applicability of the local-shearing-box approximation and the numerical methods in question probably needs to be examined in greater detail. I hope that this dissertation will seed future research improving our understanding of protoplanetary accretion disks and planet formation scenarios.

Appendix A

Velocity of a Particle at the Apogee of Its Orbit

In this section, we (re-)derive the velocity of a particle at the apogee of its elliptical orbit in the local shearing box approximation of a Keplerian disk. We repeat the Equation of motion (3.9) for a single particle without the gravity of the gas here:

$$\frac{\mathrm{d}u_x}{\mathrm{d}t} = 2\Omega_K u_y, \tag{A.1}$$

$$\frac{\mathrm{d}u_y}{\mathrm{d}t} = -\frac{1}{2}\Omega_K u_x, \tag{A.2}$$

where we have dropped the subscript p for clarity. Eliminating u_y in Equations (A.1) and (A.2) leads to

$$\frac{\mathrm{d}^2 u_x}{\mathrm{d}t^2} + \Omega_K^2 u_x = 0. \tag{A.3}$$

By assuming the particle is at the apogee at $t = 0$, the solution for u_x is

$$u_x = -A \sin \Omega_K t, \tag{A.4}$$

where A is the amplitude of the radial velocity. Since $\mathrm{d}x/\mathrm{d}t = u_x$ (Equation (3.8)), the radial oscillation is then

$$\Delta x \equiv x - x_0 = \frac{A}{\Omega_K} \cos \Omega_K t, \tag{A.5}$$

where x_0 is the radial position of the center of the orbit. From Equation (A.2), the corresponding azimuthal velocity relative to the background shear flow is

$$u_y = -\frac{1}{2} A \cos \Omega_K t = -\frac{1}{2}\Omega_K \Delta x. \tag{A.6}$$

Since the eccentricity e of the orbit is related to the amplitude of the radial oscillation by $e \approx \Delta x(t=0)/R$, where R is the distance to the central object,

$$u_y(t=0) = -\frac{1}{2} R\Omega_K e = -\frac{1}{2} H\Omega_K \left(\frac{e}{H/R}\right), \tag{A.7}$$

where H is the disk scale height. This is just the initial condition (3.13) we set out to prove. Note that we have normalized e by the ratio H/R.

Bibliography

Adams, F. C., & Bloch, A. M. 2009, ApJ, 701, 1381

Alibert Y., Mordasini C., Benz W., Winisdoerffer C., 2005, A&A, 434, 343

Andrews, S. M., & Williams, J. P. 2005, ApJ, 631, 1134

Bai, X.-N., & Goodman, J. 2009, ApJ, 701, 737

Bai, X.-N., & Stone, J. M 2010a, ApJ, submitted (arXiv:1005.4981)

Bai, X.-N., & Stone, J. M 2010b, ApJ, submitted (arXiv:1005.4982)

Balbus, S. A., & Hawley, J. F. 1991, ApJ, 376, 214

Balbus, S. A., & Hawley, J. F. 1998, Reviews of Modern Physics, 70, 1

Bate, M. R., Lubow, S. H., Ogilvie, G. I., & Miller, K. A. 2003, MNRAS, 341, 213

Beresnyak, A., & Lazarian, A. 2009, ApJ, 702, 1190

Bertout, C., Basri, G., & Bouvier, J. 1988, ApJ, 330, 350

Blum, J., & Wurm, G. 2008, ARA&A, 46, 21

Brandenburg, A. 1998, in Theory of Black Hole Accretion Disks, ed. M. A. Abramowicz et al. (Cambridge: Cambridge Univ. Press), 61

Brandenburg, A., & Dobler, W. 2002, Computer Physics Communications, 147, 471

Brandenburg, A., Nordlund, A., Stein, R. F., & Torkelsson, U. 1995, ApJ, 446, 741

Brucker, K. A., Isaza, J. C., Vaithianathan, T., & Collins, L. R. 2007, Journal of Computational Physics, 225, 20

Burrows, C. J., et al. 1996, ApJ, 473, 437

Calvet, N., & Gullbring, E. 1998, ApJ, 509, 802

Camenzind, M. 1990, Reviews in Modern Astronomy, 3, 234

Cameron, A. G. W. 1962, Icarus, 1, 13

Carpenter, J. M., Mamajek, E. E., Hillenbrand, L. A., & Meyer, M. R. 2006, ApJ, 651, L49

Chandrasekhar S., 1961, Hydrodynamic and Hydromagnetic Stability. Clarendon Press, Oxford

D'Angelo, G., Kley, W., & Henning, T. 2003, ApJ, 586, 540

Davis, S. W., Stone, J. M., & Pessah, M. E. 2010, ApJ, 713, 52

Dutrey, A., Guilloteau, S., & Ho, P. 2007, Protostars and Planets V, 495

Fleming, T., & Stone, J. M. 2003, ApJ, 585, 908

Fragile, P. C., Anninos, P., Gustafson, K., & Murray, S. D. 2005, ApJ, 619, 327

Frank J., King A. R., Raine D. J., 2002, Accretion Power in Astrophysics. Third Edition Cambridge Univ. Press, New York, NY

Fromang, S., & Papaloizou, J. 2007, A&A, 476, 1113

Fromang, S., Papaloizou, J., Lesur, G., & Heinemann, T. 2007, A&A, 476, 1123

Fromang, S., Terquem, C., & Balbus, S. A. 2002, MNRAS, 329, 18

Gammie, C. F. 1996, ApJ, 457, 355

Gammie, C. F. 2001, ApJ, 553, 174

Glassgold, A. E., Najita, J., & Igea, J. 1997, ApJ, 480, 344

Goldreich, P., & Lynden-Bell, D. 1965, MNRAS, 130, 125

Goldreich, P., & Tremaine, S. 1980, ApJ, 241, 425

Guan, X., Gammie, C. F., Simon, J. B., & Johnson, B. M. 2009, ApJ, 694, 1010

Haisch, K. E., Jr., Lada, E. A., & Lada, C. J. 2001, ApJ, 553, L153

Hartigan, P., Hartmann, L., Kenyon, S. J., Strom, S. E., & Skrutskie, M. F. 1990, ApJ, 354, L25

Hartmann, L. 2008, Physica Scripta Volume T, 130, 014012

Hartmann, L., Calvet, N., Gullbring, E., & D'Alessio, P. 1998, ApJ, 495, 385

Hartmann, L., D'Alessio, P., Calvet, N., & Muzerolle, J. 2006, ApJ, 648, 484

Haugen, N. E., & Brandenburg, A. 2004, Phys. Rev. E, 70, 026405

Haugen, N. E. L., Brandenburg, A., & Mee, A. J. 2004, MNRAS, 353, 947

Hawley, J. F., Gammie, C. F., & Balbus, S. A. 1995, ApJ, 440, 742

Hayashi, C. 1981, Progress of Theoretical Physics Supplement, 70, 35

Heinemann, T., & Papaloizou, J. C. B. 2009a, MNRAS, 397, 52

Heinemann, T., & Papaloizou, J. C. B. 2009b, MNRAS, 397, 64

Henning, T. 2008, Physica Scripta Volume T, 130, 014019

Hillenbrand, L. A. 2008, Physica Scripta Volume T, 130, 014024

Hockney, R. W., & Eastwood, J. W. 1988, Computer Simulation Using Particles (London: IOP)

Ida, S., Guillot, T., & Morbidelli, A. 2008, ApJ, 686, 1292 (IGM08)

Ida, S., & Lin, D. N. C. 2004a, ApJ, 604, 388

Ida, S., & Lin, D. N. C. 2004b, ApJ, 616, 567

Ida, S., & Lin, D. N. C. 2005, ApJ, 626, 1045

Ida, S., & Lin, D. N. C. 2008a, ApJ, 673, 487

Ida, S., & Lin, D. N. C. 2008b, ApJ, 685, 584

Igea, J., & Glassgold, A. E. 1999, ApJ, 518, 848

Ilgner, M., & Nelson, R. P. 2006, A&A, 445, 205

Johansen, A., & Klahr, H. 2005, ApJ, 634, 1353

Johansen, A., Klahr, H., & Mee, A. J. 2006, MNRAS, 370, L71

Johansen, A., Oishi, J. S., Low, M.-M. M., Klahr, H., Henning, T.,& Youdin, A. 2007, Nature, 448, 1022

Johansen, A., Youdin, A., & Klahr, H. 2009, ApJ, 697, 1269

Johansen, A., Youdin, A., & Mac Low, M.-M. 2009, ApJ, 704, L75

Johnson, B. M., Guan, X., & Gammie, C. F. 2008, ApJS, 177, 373

Johnson, E. T., Goodman, J., & Menou, K. 2006, ApJ, 647, 1413 (JGM06)

Kley, W., & Crida, A. 2008, A&A, 487, L9

Königl, A. 1991, ApJ, 370, L39

Kornet, K., & Wolf, S. 2006, A&A, 454, 989

Kuiper, G. P. 1949, ApJ, 109, 308

Lada, C. J., et al. 2006, AJ, 131, 1574

Latham, D. W., Stefanik, R. P., Mazeh, T., Mayor, M., & Burki, G. 1989, Nature, 339, 38

Laughlin, G., Steinacker, A., & Adams, F. C. 2004, ApJ, 608, 489 (LSA04)

Lesur, G., & Longaretti, P.-Y. 2007, MNRAS, 378, 1471

Li H., Finn J. M., Lovelace R. V. E., Colgate S. A., 2000, ApJ, 533, 1023

Li H., Colgate S. A., Wendroff B., Liska R., 2001, ApJ, 551, 874

Lin, D. N. C., & Papaloizou, J. 1986, ApJ, 309, 846

Lissauer, J. J. 1993, ARA&A, 31, 129

Lyra, W., Johansen, A., Klahr, H., & Piskunov, N. 2008, A&A, 479, 883

Lyra W., Johansen A., Zsom A., Klahr H., Piskunov N., 2009, A&A, 497, 869

McCaughrean, M. J., & O'dell, C. R. 1996, AJ, 111, 1977

Marcy, G. W., & Butler, R. P. 1995, Bulletin of the American Astronomical Society, 27, 1379

Masset F. S., Morbidelli A., Crida A., Ferreira J., 2006, ApJ, 642, 478

Matsumura S., Pudritz R. E., 2005, ApJ, 618, L137

Matsumura S., Pudritz R. E., 2006, MNRAS, 365, 572

Matsumura S., Pudritz R. E., Thommes E. W., 2007, ApJ, 660, 1609

Matsumura S., Pudritz R. E., Thommes E. W., 2009, ApJ, 691, 1764

Mayor, M., et al. 2009, A&A, 507, 487

Mayor, M., & Queloz, D. 1995, Nature, 378, 355

Menou, K., & Goodman, J. 2004, ApJ, 606, 520

Miller, K. A., & Stone, J. M. 2000, ApJ, 534, 398

Morbidelli, A., Bottke, W. F., Nesvorný, D., & Levison, H. F. 2009, Icarus, 204, 558

Mordasini, C., Alibert, Y., & Benz, W. 2009a, A&A, 501, 1139

Mordasini, C., Alibert, Y., Benz, W., & Naef, D. 2009b, A&A, 501, 1161

Nelson, R. P. 2005, A&A, 443, 1067 (N05)

Nelson, R. P., & Papaloizou, J. C. B. 2004, MNRAS, 350, 849

Nitta, S., Tanuma, S., Shibata, K., & Maezawa, K. 2001, ApJ, 550, 1119

Ogihara, M., Ida, S., & Morbidelli, A. 2007, Icarus, 188, 522 (OIM07)

Oishi, J. S., & Mac Low, M.-M. 2009, ApJ, 704, 1239

Oishi, J. S., Mac Low, M.-M., & Menou, K. 2007, ApJ, 670, 805 (OMM07)

O'Toole, S. J., Tinney, C. G., Jones, H. R. A., Butler, R. P., Marcy, G. W., Carter, B., & Bailey, J. 2009, MNRAS, 392, 641

Paardekooper, S.-J., Baruteau, C., Crida, A., & Kley, W. 2010, MNRAS, 401, 1950

Paardekooper, S.-J., & Mellema, G. 2006, A&A, 459, L17

Paardekooper S.-J., Papaloizou J. C. B., 2008, A&A, 485, 877

Paardekooper, S.-J., & Papaloizou, J. C. B. 2009, MNRAS, 394, 2283

Padgett, D. L., Brandner, W., Stapelfeldt, K. R., Strom, S. E., Terebey, S., & Koerner, D. 1999, AJ, 117, 1490

Papaloizou, J. C. B., & Larwood, J. D. 2000, MNRAS, 315, 823

Papaloizou J., Lin D. N. C., 1984, ApJ, 285, 818

Papaloizou, J. C. B., & Terquem, C. 2006, Reports on Progress in Physics, 69, 119

Pessah, M. E., Chan, C.-k., & Psaltis, D. 2007, ApJ, 668, L51

Pollack J. B., Hubickyj O., Bodenheimer P., Lissauer J. J., Podolak M., Greenzweig Y., 1996, Icar, 124, 62

Rafikov R. R., 2006, ApJ, 648, 666

Rafikov, R. R. 2007, ApJ, 662, 642

Rafikov, R. R. 2009, ApJ, 704, 281

Rein, H., & Papaloizou, J. C. B. 2009, A&A, 497, 595

Rice, W. K. M., Armitage, P. J., Bate, M. R., & Bonnell, I. A. 2003, MNRAS, 339, 1025

Robinson, S. E., Laughlin, G., Bodenheimer, P., & Fischer, D. 2006, ApJ, 643, 484

Sano, T., Inutsuka, S.-i., Turner, N. J., & Stone, J. M. 2004, ApJ, 605, 321

Sano, T., Miyama, S. M., Umebayashi, T., & Nakano, T. 2000, ApJ, 543, 486

Schlaufman K. C., Lin D. N. C., Ida S., 2009, ApJ, 691, 1322

Semenov, D., Wiebe, D., & Henning, T. 2004, A&A, 417, 93

Shakura, N. I., & Sunyaev, R. A. 1973, A&A, 24, 337

Shi, J.-M., Krolik, J. H., & Hirose, S. 2009, ApJ, submitted (arXiv:0909.2003)

Sicilia-Aguilar, A., et al. 2006, ApJ, 638, 897

Simon, J. B., Hawley, J. F., & Beckwith, K. 2009, ApJ, 690, 974

Tanaka, H., Takeuchi, T., & Ward, W. R. 2002, ApJ, 565, 1257

Tassoul J. L., 1978, Theory of Rotating Stars. Princeton Univ. Press, Princeton, NJ

Thommes, E. W., Matsumura, S., & Rasio, F. A. 2008, Science, 321, 814

Turner, N. J., Sano, T., & Dziourkevitch, N. 2007, ApJ, 659, 729

Valenti, J. A., Basri, G., & Johns, C. M. 1993, AJ, 106, 2024

Ward, W. R. 1997, Icarus, 126, 261

Watson, A. M., Stapelfeldt, K. R., Wood, K., & Ménard, F. 2007, Protostars and Planets V, 523

Weidenschilling, S. J. 1977, MNRAS, 180, 57

Williamson, J. H. 1980, Journal of Computational Physics, 35, 48

Yang, C.-C., & Menou, K. 2010, MNRAS, 402, 2436

Yang, C.-C., Mac Low, M.-M., & Menou, K. 2009, ApJ, 707, 1233

Youdin, A. N., & Goodman, J. 2005, ApJ, 620, 459